# NUMERICAL ABERRATIONS COMPENSATION AND POLARIZATION IMAGING IN DIGITAL HOLOGRAPHIC MICROSCOPY

THÈSE N$^{O}$ 3455 (2006)

PRÉSENTÉE À LA FACULTÉ SCIENCES ET TECHNIQUES DE L'INGÉNIEUR

Laboratoire d'optique appliquée

SECTION DE MICROTECHNIQUE

ÉCOLE POLYTECHNIQUE FÉDÉRALE DE LAUSANNE

POUR L'OBTENTION DU GRADE DE DOCTEUR ÈS SCIENCES

PAR

Tristan COLOMB

ingénieur physicien diplômé EPF
de nationalité suisse et originaire de Bagnes (VS)

acceptée sur proposition du jury:

Prof. Ph. Renaud, président du jury
Prof. R.P. Salathé, directeur de thèse
Prof. C. Depeursinge, rapporteur
Prof. M. Gu, rapporteur
Prof. H. Tiziani, rapporteur
Prof. M. Unser, rapporteur

ÉCOLE POLYTECHNIQUE
FÉDÉRALE DE LAUSANNE

Lausanne, EPFL
2006

*En mémoire de Grand-maman, Pierrot et Simon*

# Abstract

In this thesis, we describe a method for the numerical reconstruction of the complete wavefront properties from a single digital hologram: the amplitude, the phase and the polarization state. For this purpose, we present the principle of digital holographic microscopy (DHM) and the numerical reconstruction process which consists of propagating numerically a wavefront from the hologram plane to the reconstruction plane. We then define the different parameters of a Numerical Parametric Lens (NPL) introduced in the reconstruction plane that should be precisely adjusted to achieve a correct reconstruction. We demonstrate that automatic procedures not only allow to adjust these parameters, but in addition, to completely compensate for the phase aberrations. The method consists in computing directly from the hologram a NPL defined by standard or Zernike polynomials without prior knowledge of physical setup values (microscope objective focal length, distance between the object and the objective...). This method enables to reconstruct correct and accurate phase distributions, even in the presence of strong and high order aberrations. Furthermore, we show that this method allows to compensate for the curvature of specimen. The NPL parameters obtained by Zernike polynomial fit give quantitative measurements of micro-optics aberrations and the reconstructed images reveal their surface defects and roughness. Examples with micro-lenses and a metallic sphere are presented.

Then, this NPL is introduced in the hologram plane and allows, as a system of optical lenses, numerical magnification, complete aberration compensation in DHM (correction of image distortions and phase aberrations) and shifting. This NPL can be automatically computed by polynomial fit, but it can also be defined by a calibration method called Reference Conjugated Hologram (RCH). We demonstrate the power of the method by the reconstruction of non-aberrated wavefronts from holograms recorded specifically with high orders aberrations introduced by a tilted thick plate, or by a cylindrical lens or by a lens ball used instead of the microscope objective.

Finally, we present a modified digital holographic microscope permit-

ting the reconstruction of the polarization state of a wavefront. The principle consists in using two reference waves polarized orthogonally that interfere with an object wave. Then, the two wavefronts are reconstructed separately from the same hologram and are processed to image the polarization state in terms of Jones vector components. Simulated and experimental data are compared to a theoretical model in order to evaluate the precision limit of the method for different polarization states of the object wave.

We apply this technique to image the birefringence and the dichroism induced in a stressed polymethylmethacrylate sample (PMMA), in a bent optical fiber and in a thin concrete specimen. To evaluate the precision of the phase difference measurement in DHM design, the birefringence induced by internal stress in an optical fiber is measured and compared to the birefringence profile captured by a standard method, which had been developed to obtain high-resolution birefringence profiles of optical fibers. A 6 degrees phase difference resolution is obtained, comparable with standard imaging polariscope, but with the advantage of a single acquisition allowing real-time reconstruction.

**Keywords**: Computer Holography, Microscopy, Aberration Compensation, Polarization

# Version abrégée

Dans cette thèse, nous décrivons une méthode capable de reconstruire numériquement et complètement les propriétés d'un front d'onde à partir d'un unique hologramme digital: l'amplitude, la phase et l'état de polarisation. Dans ce but, nous présentons le principe de la Microscopie par Holographie Digitale (DHM) et le processus de reconstrution qui consiste à propager numériquement un front d'onde à partir du plan de l'hologramme jusqu'au plan de reconstruction. Nous définissons ensuite les différents paramètres d'une Lentille Numérique Paramétrique (NPL), introduite dans le plan de reconstruction, qui doivent être précisément ajustés pour obtenir une reconstruction correcte. Nous démontrons que des procédures automatiques permettent non seulement d'ajuster ces paramètres mais de plus de compenser complètement les aberrations de phase. La méthode consiste à calculer directement, à partir de l'hologramme, une NPL définie par des polynômes standards ou de Zernike sans connaissance a priori des valeurs physiques du montage expérimental (focale de l'objectif de microscope, distance entre l'objet et l'objectif...). Cette méthode permet de reconstruire les distributions de phase correctement et précisément, même en présence d'aberrations fortes ou d'ordres élevés. De plus, nous montrons que cette méthode permet de compenser la courbure de spécimens. Les paramètres de la NPL obtenus avec l'approche par les polynômes de Zernike fournissent des mesures quantitatives des aberrations de micro-optiques et les images reconstruites révèlent leur défauts de surface et leur rugosité. Des exemples avec des micro-lentilles et une sphère métallique sont présentés.

Ensuite, cette NPL est introduite dans le plan de l'hologramme et permet, comme un système de lentilles optiques, des décalages et des grandissements numériques paramétrables ainsi qu'une compensation totale des aberrations en DHM (correction des distorsions d'images et des aberrations de phase). Cette NPL peut être calculée automatiquement par une approche polynomiale, mais elle peut aussi être définie par une méthode de calibrage appellée Hologramme de Référence Conjugué (RCH). Nous démontrons la puissance de la méthode en reconstruisant des fronts d'onde non aberrés à partir d'hologrammes volontairement enregistrés avec des

aberrations d'ordre élevé introduites par une lame épaisse inclinée, par une lentille cylindrique ou par une lentille sphérique utilisées à la place d'un objectif de microscope.

Enfin, nous présentons un microscope holographique digital modifié qui permet de reconstruire l'état de polarisation d'un front d'onde. Le principe consiste à utiliser deux ondes de référence polarisées orthogonalement qui interfèrent avec une onde objet. Ensuite, l'état de polarisation, exprimé en termes de composantes du vecteur de Jones, est calculé à partir des deux fronts d'onde reconstruits séparément à partir du même hologramme. Des mesures simulées et expérimentales sont comparées à un modèle théorique dans le but d'évaluer la limite de précision de la méthode pour différents états de polarisation de l'onde objet.

Nous appliquons cette technique à l'imagerie de biréfringence et de dichroïsme induits dans un échantillon de polymethylmethacrylate (PMMA) soumis à une contrainte, dans une fibre optique courbée, ainsi que dans un échantillon fin de béton. Afin d'évaluer la précision sur la mesure de différence de phase pour un montage expérimental en microscopie, la biréfringence induite par les contraintes internes d'une fibre optique est mesurée et comparée au profil de biréfringence obtenu par une méthode standard, qui a été développée pour obtenir des hautes résolutions de profils de biréfringence pour les fibres optiques. Une résolution de 6 degrés pour la différence de phase est obtenue, ce qui est comparable aux polariscopes standards avec l'avantage d'une unique acquisition et donc d'une reconstruction possible en temps réel.

**Mots clefs**: Holographie digitale, Microscopie, Compensation d'aberration, Polarisation

# Acknowledgements

A Long Time Ago in the MVD Group Far, Far Aware...

I met a wise man named Prof. Christian Depeursinge who instructed me on the Force of optical engineering. His competence, his enthusiasm, and his many pertinent ideas gave to me, and to the other Rebels of digital holography, the Force and the wisdom to fight the dark side of a thesis work. He was always there when a recorded hologram said: "Help me, Christian Depeursinge, you are our only hope." His sympathy and his kindness is always like a light saber that illuminates the friendship of his group. Therefore, I would like to thank him a lot to have initiated and directed this thesis work.

Then, I would like to thank my thesis advisor, and director of the Institute of Applied Optics, Prof. René-Paul Salathé, who pushed me to finish my training before facing the thesis examination. I am grateful to him for having given me the opportunity to achieve this thesis in excellent conditions. Thanks to Prof. M. Gu, Prof. H. Tiziani, Prof. M. Unser and Prof. P. Renaud for having accepted to participate in the jury of this thesis.

I would now like to thank very much all the Rebellion members. First the Red Leader of digital holography, Dr. Etienne Cuche, who opened the way with his thesis and who proposed to me a semester project in 1999, which has stimulated my interest in digital holography; the Chewie of my office, Dr. Frédéric Montfort, for all the discussions about science or not, and especially for his bellowing about the culinary quality of the Vinci; the R2D2 of the experimental setups, always there to help, Jonas Kühn and the 3PO specialist of the belgian joke, Michel Saint-Ghislain. I will never forget the other office, (fortunately not the dark side), Florian Charrière for helping me to use the OPA Death Star, and Anca Marian for their availabilities and their invaluable advice. I only regret that Anca did not explain to us how she uses the Force to evaporate herself... I would like to thank the other people I met in the MVD group or during collaboration with Lyncéetec SA: Dr. Pia Massatsch, Dr. Daniel Salzmann, Sylvain Her-

minjard, Yves Delacrétaz, Dr. Nicolas Aspert, François Marquet, Mikhail Botkine, Dr. Yves Emery, Sébastien Bourquin. Moreover I would to thank all my colleagues of the Institute of Imaging and Applied Optics for their availability and their kindness. In particular, I would thank Manuelle Borruat and Yvette Bernhard for the remainders and the bureaucracy and Alejandro Salamanco for the preparation and the updates of the fighter computers, and the members of the volley team (Rodrigue, Yann, Dragan, Roland), with whom I could exercise my senses.

I want to thank my friends of the beautiful planet Bagnes. They gave me the Force and the courage to do my best by changing my mind during the week end. I think in particular of the members of the Chenegouga which are like my Ewoks team, always smiling and ready to have fun. Finally, I want to thank my family that gave me the opportunity to study such a long time, a very long time. They were always there in the dark time as in the good time.

I would to thank particularly Suzette and Pierre, whose corrected my bad english and César for the bottle of red wine, that comforted me after the death of Raul le pigeon.

And at the end, I would to thank my princess Hélène who supported me and encouraged me in all these thesis days.

Thanks to all these people, they can say to me: "The thesis is strong with you, "young student", and you are a doctor now."

# Contents

# List of Figures

# List of Notations

## Roman Letters

| | |
|---|---|
| $c_o$ | Light velocity in free space |
| $C_b$ | Relative strain-optic coefficient |
| $C$ | Curvature compensation parameter |
| $d$ | Reconstruction distance |
| $\boldsymbol{D}$ | Electric flux density |
| $E_x, E_y$ | Complex number |
| $I_H(x, y)$ | Hologram |
| $I_{\boldsymbol{R}}$ | Intensity of reference wave |
| $I_{\boldsymbol{O}}$ | Intensity of object wave |
| $i$ | $\sqrt{-1}$ |
| $j, k, l, m, n$ | Integer numbers |
| $\boldsymbol{J_E}$ | Jones vector of the wave $\boldsymbol{E}$ |
| $\boldsymbol{k}, \boldsymbol{k_R}, \boldsymbol{k_O}$ | Wave vectors |
| $k$ | Wavenumber |
| $k_x, k_y$ | Tilt compensation parameters |
| $n$, $n_j$ | (Principal) Refractive index |
| $\boldsymbol{O}$ | Object wave |
| $P_\alpha, P_{jk}$ | Aberration compensation parameters |
| $\boldsymbol{R}$ | Reference wave |
| $\boldsymbol{R}_D$ | Digital reference wave |
| $\boldsymbol{R}_1$ | Reference wave polarized horizontally |
| $\boldsymbol{R}_2$ | Reference wave polarized vertically |
| $t$ | Temporal variable |
| $\boldsymbol{U}, \boldsymbol{E}$ | Wave |
| $\boldsymbol{x} = (x, y, z)$ | Position vector |

## Greek Letters

| | |
|---|---|
| $\Delta\varphi$ | Phase difference |
| $\Delta n$ | Index difference |
| $\Delta x, \Delta y$ | Pixel size of CCD camera |
| $\Delta\xi, \Delta\eta$ | Pixel size in the reconstruction plane |
| $\varepsilon$ | Arctangent of the ratio of the Jones vector amplitude components |
| $\epsilon$, $\epsilon_{ij}$ | (Coefficients) Electric permittivity tensor |
| $\epsilon_0$ | Permittivity of free space |
| $\eta$ | Electric impermeability tensor |
| $\gamma$ | Polarization ellipse azimuth |
| $\Gamma^{P,D}$ | NPL in plane P to Shift ($D = Sh$); Magnify ($D = M$); Compensate for the aberrations ($D = C$) or the specimen shape ($D = SCL$) |
| $\Gamma_S$, $\Gamma_Z$ | NPL expressed in Standard or Zernike polynomials |
| $\lambda$ | Wavelength |
| $\nu_{\max}$ | Spatial frequency cut-off |
| $\omega$ | Polarization ellipse ellipticity |
| $\varphi$ | Phase |
| $\Phi$ | Curvature compensating digital phase mask |
| $\varpi$ | Wave pulsation |
| $\pi$ | 3.141592... |
| $\Psi$ | Reconstructed wave front |
| $\sigma$ | Principal stress |
| $\theta$,$\theta_{\max}$ | (Maximal) Angle between reference and object wave |

## Other notations

| | |
|---|---|
| CF | Convolution Formulation |
| FFT | Fast Fourier Transform |
| $\text{FFT}^{-1}$ | Inverse Fast Fourier Transform |
| DHM | Digital Holographic Microscopy |
| FT | Fourier Transform |
| $\text{FT}^{-1}$ | Inverse Fourier Transform |
| $H$ | Hologram plane |
| $I$ | Image plane |

| | |
|---|---|
| MO | Microscope Objective |
| NA | Numerical Aperture |
| NPL | Numerical Parametric Lens |
| ROI | Region Of Interest |
| RCH | Reference Conjugated Hologram |
| SCL | Shape Compensation Lens |
| SFTF | Single Fourier Transform Formulation |
| SOP | State Of Polarization |
| std | Standard Deviation |
| $\mathcal{F}_\tau$ | Two-dimensional Fresnel Transform |
| $Z^*$ | Complex conjugate |
| $\otimes$ | Symbol of convolution |

# Chapter 1

# Introduction

## 1.1 Goal of Thesis

The great advantage of holographic techniques is that a single hologram acquisition allows theoretically to record and to reconstruct simultaneously the amplitude and the phase components of a wavefront. This feature is very well demonstrated in classical holography with art holograms that show 3D images of human faces for example. In the case of digital holography (DH) and digital holographic microscopy (DHM), this feature is very often proposed but not always accomplished. Indeed, the numerical process of wavefront reconstruction needs a precise adjustment of several parameters so that these computed data fit as close as possible their experimental equivalences. This approach seems to require a perfect a-priori knowledge of these parameters. Therefore a majority of authors prefer to reconstruct the phase component by using several holograms with apparently a more simple procedure.

Another proposed advantage in classical holography is the possibility to record on the same support different interference patterns (multi-exposed holograms). A first possibility is to record these interferences by changing the reference wave orientation. As a consequence, when the hologram is illuminated, different reconstructed objects appear, depending on the orientation of the illumination wave. Well known examples are the artistic holograms where we can observe a human face smiling or not, when looking at it from the left or from the right. Another possibility is to record simultaneously the interferences between an object wave and several reference waves as suggested by Lohmann in 1965 [Loh65], and especially using two different polarized reference waves. If the first possibility has no real interest in digital holography, the second one can be applied easily and allows a polarization imaging by use of a single hologram.

This thesis is dedicated to the application of numerical methods for the reconstruction of the amplitude, the phase, and the polarization state of a wavefront by using a single hologram. For these purposes, automatic procedures are developed to adjust the reconstruction parameters without knowing them beforehand. Furthermore, a complete aberration compensation of the DHM technique is presented.

## 1.2 Structure of the Dissertation

In the next sections of the present chapter, some basics of classical holography are summarized, followed by a brief state of the art of digital holography. Then, we present some basics of polarization, the Jones formalism, the interpretation of polarization parameters in terms of dichroism and birefringence, and finally the state of the art of polarization imaging. Chapter 1 constitutes the introduction, Chapters 2, 3, 4, 5 and 6 the core of the thesis and Chapter 7 the conclusion.

This thesis is divided in two different parts. The first one (Chapters 2, 3 and 4) is dedicated to the wavefront reconstruction procedure from a single hologram. In Chapter 2, we present and develop in detail the basics of the procedure presented initially by Cuche *et al.* [Cuc99a, Cuc99b, Cuc00c, Cuc00d]. We discuss and compare the implementation of this procedure to the two numerical reconstruction formulation in DHM: the Single Fourier Transform Formulation (SFTF) and the Convolution Formulation (CF). For this purpose, we introduce the concept of Numerical Parametric Lens (NPL), an array of complex numbers calculated from several parameters that have to be adjusted precisely in the reconstructed plane to achieve a correct wavefront reconstruction. In Chapter 3 (modified version of Ref. [Col06]), NPL is generalized and defined with two different 2D polynomial models (Standard and Zernike polynomials) to compensate for phase aberrations. We show in Section 3.3 that automatic procedures allow to adjust the reconstruction parameters defining this NPL. Finally in Chapter 4, a complete aberration compensation (compensation of amplitude, phase and image distortion) is achieved by applying NPL in the hologram plane instead of the reconstruction plane. We show first that this NPL can be defined and adjusted by polynomial fit as in the reconstruction plane. We present also a calibration method, inspired by the works of Ward *et al.* [War71] and Upatnieks *et al.* [Upa66], that computes the NPL from a conjugated reference hologram. Furthermore, we demonstrate that this NPL, placed in the hologram plane, behaves like a physical optical lens and can be used to magnify or to shift the reconstructed images.

The second part (Chapters 5 and 6) concerns the application of DHM to polarization imaging. In Chapter 5, the design and principle of the reconstruction of the State Of Polarization (SOP) are presented. The limit of precision of the method is estimated by a simulated and experimental study (modified version of Ref. [Col04]). Finally, Chapter 6 presents different applications and results of the DHM-Polariscope (modified versions of Refs [Col02b, Col05b, Col05a].

### 1.2.1 Classical Holography

#### Generalities

A description of the different forms and applications of classical holography is already developed in detail in several books [Goo68, Har96, Col71, Han79, Str69, Smi69, Fra87]. Furthermore, an exhaustive list of historical papers and an interesting overview of the developments of holography, from its discovery by Denis Gabor in 1947 to the present, can be found in Ref. [Lei97]. Here we just give a short presentation of off-axis holography and introduce some conventions of vocabulary, symbols and geometry which will be used throughout this thesis.

It is however important to mention that, although digital holography took a great importance in the holographic topics, the classical holography cannot be and should not be reduced to only 3D spectacular art images. The research work began during the 1950s and the 1960s by several famous personalities like D. Gabor, E.N. Leith, A. Lohmann, R.J. Collier, J. Upatnieks, G. Stroke, N. Hartman, Yu. N. Denisyuk, S. Benton, R.F. Vanligte, J.W. Goodman, R. Dändliker, H. Tiziani, and N. Abramson, continues today for many different applications like holographic data storage [She97, Ort03], photorefractive crystals applications [Roo03], or light-in-flight for ultrafast phenomena recording [Yam05] among others.

Furthermore, classical holography is a source of inspiration for the development of digital holography. For example, the configuration of DHM presented in [Cuc99b] and used in this thesis was presented for the first time in 1966 by VanLighte and Oserberg [Van66]. In the particular case of this thesis, we can mention that the use of holography for polarization imaging (Chapters 5 and 6) follows an idea initially proposed by A. Lohmann in 1965 [Loh65], and the calibration method presented in Section 4.5.3 is directly inspired from works of Ward and Upatnieks [Upa66, War71].

### Recording and reconstruction of a hologram

A hologram results from the interference between two coherent waves, a first wave called the object wave $\boldsymbol{O}$ emanating from the object and a second one called the reference wave $\boldsymbol{R}$. In the hologram plane *0xy*, these two waves produce an interference pattern with a two-dimensional (2D) intensity distribution:

$$I_H(x,y) = (\boldsymbol{R}+\boldsymbol{O})(\boldsymbol{R}+\boldsymbol{O})^* = |\boldsymbol{R}|^2 + |\boldsymbol{O}|^2 + \boldsymbol{R}^*\boldsymbol{O} + \boldsymbol{R}\boldsymbol{O}^*, \qquad (1.1)$$

where $|\boldsymbol{R}|^2 = I_{\boldsymbol{R}}$ is the intensity of the reference wave and $|\boldsymbol{O}|^2 = I_{\boldsymbol{O}}(x,y)$ the intensity of the object wave. $\boldsymbol{R}^*\boldsymbol{O}$ and $\boldsymbol{R}\boldsymbol{O}^*$ are the interference terms with $\boldsymbol{R}^*$ and $\boldsymbol{O}^*$ denoting the complex conjugates of the two waves. In classical holography, this interference pattern is principally recorded on photographic plates, photorefractive material, or photopolymers.

Assuming a plane reference wave with a uniform intensity $I_{\boldsymbol{R}}$ and a hologram transmittance proportional to the exposure, the so-called reconstructed wavefront $\Psi$ is obtained by the illumination of the hologram with a plane wave $\boldsymbol{U}$:

$$\Psi(x,y) = \boldsymbol{U}I_H(x,y) = \boldsymbol{U}I_{\boldsymbol{R}} + \boldsymbol{U}I_{\boldsymbol{O}} + \boldsymbol{U}\boldsymbol{R}^*\boldsymbol{O} + \boldsymbol{U}\boldsymbol{R}\boldsymbol{O}^*. \qquad (1.2)$$

The two first terms of Eq. 1.2 form the zero order of diffraction which will be sometimes called zero order (ZO) in what follows. The third and the fourth terms are produced by the interference terms and they generate two conjugate or twin images of the object. $\boldsymbol{U}\boldsymbol{R}^*\boldsymbol{O}$ produces a virtual image located at the initial position of the object and $\boldsymbol{U}\boldsymbol{R}\boldsymbol{O}^*$ produces a real image located on the other side of the hologram. If the reconstruction is performed by illuminating the hologram with a replica of the reference wave ($\boldsymbol{U} = \boldsymbol{R}$) the virtual image is a replica of the object wave multiplied by the reference intensity ($I_{\boldsymbol{R}}\boldsymbol{O}$). Reciprocally if $\boldsymbol{U} = \boldsymbol{R}^*$, the real image is a replica of the conjugate object wave multiplied by the reference intensity ($I_{\boldsymbol{R}}\boldsymbol{O}^*$).

In classical holography, the condition $\boldsymbol{U} = \boldsymbol{R}$ or $\boldsymbol{U} = \boldsymbol{R}^*$ is generally required, especially for so-called thick or volume holograms for which the recording of the interference in the thickness of the photographic emulsion defines a Bragg condition for the illuminating wave (see. e.g. Ref. [Goo68], chap. 8). This Bragg condition also acts on the wavelength of the illuminating wave and if light with a broad spectrum (white light) is used for the reconstruction process, only the "correct" wavelength will participate to the image formation. For thin holograms, the condition $\boldsymbol{U} = \boldsymbol{R}$ or $\boldsymbol{U} = \boldsymbol{R}^*$ cannot be strictly satisfied with a repercussion on the quality of the reconstructed images; in particular, their resolution [Cha69]. As explained

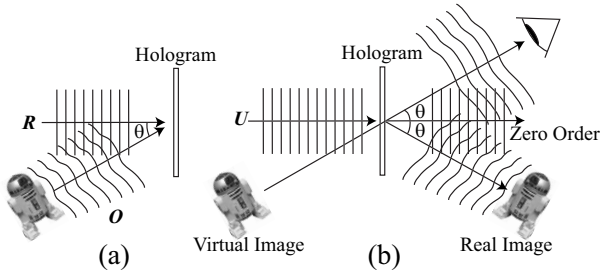


*Figure 1.1: (a) Recording and (b) reconstruction of an off-axis hologram.*

in Ref. [Cuc99a] and developed in Chapter 2 of this thesis, the phase reconstruction in DHM is performed by replacing the illuminating wave $\boldsymbol{U}$ by a digital reference $\boldsymbol{R}_D$, which must be an exact replica of the optical reference wave.

### Off-axis holography

In Gabor's original work, the hologram was recorded in an inline geometry with an object wave and a reference wave having parallel directions of propagation. In this case, the four components of Eq. 1.2 propagate along the same direction and cannot be observed separately. The idea with off-axis holography (Fig. 1.1) is to introduce an angle $\theta$ between the directions of propagation of the object and reference waves. Therefore, the different terms of the interference propagate along separated directions during the reconstruction. Indeed, if we assume a plane reference wave of the form:

$$\boldsymbol{R}(x,y) = \sqrt{I_{\boldsymbol{R}}}\exp\left(ikx\sin\theta\right), \tag{1.3}$$

where $k = 2\pi/\lambda$ is the wavenumber. The intensity on the hologram plane becomes:

$$I_H = I_{\boldsymbol{R}} + I_{\boldsymbol{O}} + \sqrt{I_{\boldsymbol{R}}}\exp\left(-ikx\sin\theta\right)\boldsymbol{O} + \sqrt{I_{\boldsymbol{R}}}\exp\left(ikx\sin\theta\right)\boldsymbol{O}^*. \tag{1.4}$$

The phase factor $\exp\left(-ikx\sin\theta\right)$ in the third term indicates that the wave, which produces the virtual image, is deflected with an angle $-\theta$ with respect to the direction of the illuminating wave $\boldsymbol{U}$. The opposite phase factor appears in the fourth term, meaning that the wave producing the real image is deflected with an angle $\theta$. The zero order of diffraction propagates in the same direction as $\boldsymbol{U}$. In other words, the off-axis geometry allows to separate spatially the different orders of diffraction.

### 1.2.2 Digital Holography: State of the Art

An overview on digital holography can be found in Ref. [Sch02]; therefore, we give here only a brief account of the history of digital holography.

The principle of digital holography is identical to the classical one. The idea is always to record the interference between an object wave and a reference wave in an in-line or off-axis geometry. The major difference consists in replacing the photographic plate by a digital device like a charged-couple device camera (CCD), and in achieving the reconstruction process numerically. This idea was proposed for the first time in 1967 by J.W. Goodman and R.W. Laurence [Goo67] and numerical hologram reconstruction was initiated by M.A. Kronrod and L.P. Yaroslavsky [Kro72b, Kro72a] in the early 1970s. They still recorded in-line and Fourier holograms on a photographic plate, but they enlarged and sampled part of them to reconstruct them numerically.

A complete digital holographic setup in a sense of digital recording and reconstruction was achieved by U. Schnars and W. Jüptner when they introduce a CCD camera to record Fresnel holograms [Sch94b]. This method suppresses the long intermediate step of photographic plate development between the recording and the numerical reconstruction process and allows high acquisition and reconstruction rates.

Important steps in the evolution of the technique and algorithms have been proposed since: acquisition through endoscopic device [Coq95, Sch99, Sch01, Kol03, Ped03], the use of large wavelength [All03] and short-coherence laser sources [Ped01a, Ped02, Mas05, ML05a]. An important step was the reconstruction of the phase in addition to the amplitude. Different techniques exist to reconstruct the phase. In-line techniques require phase-shifting procedures done with several holograms acquired successively [Yam97, Zha98, Lai00b, Guo02, Yam03, Awa04, Mil05] or simultaneously [Kol92, Kem99, Mil01, Dun03, Wya03]. In off-axis configuration, Schnars *et al.* [Sch94a] demonstrated the possibility to measure specimen deformations by evaluating the phase difference between two states of the specimen. However, this double exposure technique does not give the absolute phase of the object wave.

A solution for absolute phase measurements was proposed by Cuche *et al.* in 1999 [Cuc99a] and then by Liebling [Lie03, Lie04b]. They showed that the reconstruction of the phase can be done from a single hologram as in classical holography by the adjustment of several parameters. However, as proposed initially, the procedure for this parameters adjustment is not automated and requires a prior knowledge of the parameters values, making the method not user-friendly. To avoid this adjustment, Ferraro

*et al.* [Fer03b] used a reference hologram taken in a flat part of the specimen, and a subtraction procedure for aberrations compensation. This simple technique performs efficiently if the experimental presence of parasitic conditions (vibrations, drifts,...) are well controlled, but fails in providing precise measurements in most of the situations, and is therefore not adapted for most practical applications.

Then, Cuche *et al.* showed in Ref. [Cuc99b] that their technique can be applied in DHM developed recently [Had92, Zha98, Tak99, Tis01, Xu01, Yam01b, Dub02a, Car04, Cop04]. Because DHM allows for truly noninvasive examination of biological specimen, the interest of digital holography techniques for biomedical applications increases [Col02a, Tis03, Ale04, Car04, Pop04, vH04, Ike05, Tis05, Mas05, ML05a, Mar05, Jeo05, Jav05b, Ahn05, Sun05, Rap05]. Other developments are proposed as tomographic digital holography [Ind99, Kim00, Dak03, Mas05, The05, ML05a, Yu05], optical diffraction tomography [Cha06c], color digital holography [Kat02, Yam02, Alm04, Jav05a], synthetic-wavelength digital holography [Ono98, Wag00, Gas03] and several aberrations compensation techniques [Cuc99b, Sta00, Ind01, Ped01b, dN02, Fer03a, Fer03b, ML05a, Yon05, dN05b, Col06].

Other applications are deformation analysis and shape measurement [Ped97, Nil98, Kem99, Nil00, Yam01a, Ma04], particle tracking [Mur00, Coe02, Hin02, Soo02, Fer03a, Leb03, Pan03, Xu03, Mül04], information encrypting [Jav00, Taj00, Lai00a, Yu03, Nis04, Nom04, He05, Sit05], refractometry [Keb99, Dub99, Bac05, Seb05, Apo04], electrochemistry [Wan04, Yan04], vibration measurement [Zha04a, Bor05, Iem05], micro-optic testing [Mül05b, Sin05, Cha06a] or ferroelectric metrology [dA04, dN04, Gri04, Pat05]. We mention also the paper of Beghuin *et al.* in Ref. [Beg99] that applies digital holography to polarization imaging. This paper shows the feasibility of DHM to image the polarization state that is presented in this thesis (Chapters 5 and 6) and published in the Ref. [Col02b, Col04, Col05b].

## 1.3 Basics of Polarization

This section presents and defines the polarization parameters used through out this thesis and particularly in Chapters 5 and 6. For more details about polarization light, the reader can consult different books as for example Refs. [Kli90, Sal91, Bor80].

Two different formalisms exist to represent the polarization state of a wave: the Jones and Stokes formalisms. The fact that it usually is easier to measure intensities than phases, the second one is very often used because it expresses the polarization state in terms of different intensities.

In this thesis, because the digital holographic technique allows to measure the phase of a wavefront, the use of Jones formalism is preferred. Therefore only the Jones formalism is presented in the following section ; but simple relations between Jones and Stokes parameters can be found in the Ref. [Kli90]. In the second part of this section we present different techniques for polarization imaging.

### 1.3.1 Jones Formalism

We define a wave $\boldsymbol{E}$ that is the superposition of two waves $E_x$ and $E_y$ that have the same pulsation $\varpi$ and the same wave vector $\boldsymbol{k}$ along $z$, but with orthogonal vibration planes:

$$\boldsymbol{E} = \begin{pmatrix} E_x \\ E_y \\ 0 \end{pmatrix} \exp[i(\boldsymbol{kx} - \varpi t], \tag{1.5}$$

where $\boldsymbol{x} = (x, y, z)$ is the position vector, $E_x$ and $E_y$ are complex numbers:

$$\begin{array}{l} E_x = |E_x| \exp(i\varphi_x) \\ E_y = |E_y| \exp(i\varphi_y) \end{array} . \tag{1.6}$$

We can normalize Eq. 1.5 by dividing the two components of $\boldsymbol{E}$ by $E_x \exp[i(\boldsymbol{kx} - \varpi t]$ and we define the polarization property of the wave $\boldsymbol{E}$ by its Jones vector:

$$\boldsymbol{J_E} = \begin{pmatrix} 1 \\ \tan(\varepsilon) \exp(i\Delta\varphi) \\ 0 \end{pmatrix}, \tag{1.7}$$

where

$$\begin{array}{c} \tan(\varepsilon) = \frac{|E_y|}{|E_x|} \\ \Delta\varphi = \varphi_y - \varphi_x \end{array} , \tag{1.8}$$

These two parameters called respectively the wave amplitudes ratio and the phase difference define entirely the polarization ellipse (Fig 1.2). This ellipse corresponds to the projection of the trajectory of the extremity of the vector $\boldsymbol{E}$ on the plane $xy$. This ellipse has also three principal parameters generally used, that are deduced from the parameters defined

in Eq. 1.8. These parameters are respectively the ellipse azimuth $\gamma$, the ellipticity $\omega$ and the direction of rotation of the vector $\boldsymbol{E}$:

$$\begin{array}{l}\gamma = 1/2 \arctan[\tan(2\varepsilon)\cos(\Delta\varphi)],\\ \omega = 1/2 \arcsin[\sin(2\varepsilon)\sin(\Delta\varphi)],\\ -\pi \leq \Delta\varphi \leq 0\text{: left-hand polarization (L-state)},\\ 0 \leq \Delta\varphi \leq \pi\text{: right-hand polarization (R-state)}.\end{array} \tag{1.9}$$

In the particular case when $\Delta\varphi = m \cdot 2\pi$ ($m \in \mathbb{Z}$), the elliptical state degenerates in two linear polarization states. Another particular case appears when $\varepsilon = \pi/4$ and $\Delta\varphi = \pi/2$: the polarization is called circular. These two different particular cases allow to construct an orthonormal basis of the polarization states. For example, we can define two orthogonal Jones vectors with two linear orthogonal polarizations:

$$\boldsymbol{R}_1 = \begin{pmatrix} 1 \\ 0 \\ 0 \end{pmatrix}, \boldsymbol{R}_2 = \begin{pmatrix} 0 \\ 1 \\ 0 \end{pmatrix}. \tag{1.10}$$

Therefore any State of Polarization (SOP) are a linear combination of these two Jones vectors:

$$\boldsymbol{E} = E_1 \boldsymbol{R}_1 + E_2 \boldsymbol{R}_2. \tag{1.11}$$

The coefficients $E_1$ and $E_2$ can be easily calculated by projecting the vector $\boldsymbol{E}$ on the basis vectors ($E_j = \boldsymbol{R}_j \boldsymbol{E}$, $j = 1, 2$). In the particular case of the basis defined in Eq. 1.10, the coefficients are simply $E_1 = E_x$ and $E_2 = E_y$ defined in Eq. 1.6.

In the context of interferometry, we can see immediately that this projection is recorded in the virtual image term of the hologram intensity (Eq. 1.1) if $\boldsymbol{R}_j = \boldsymbol{R}^*$. Chapters 5 and 6 show that the SOP parameters $\varepsilon$ and $\Delta\varphi$ can be imaged therefore very simply with digital holography.

### 1.3.2 Polarization Parameters Interpretation

Assuming that the parameters $\varepsilon$ and $\Delta\varphi$ can be measured and that a known SOP wave illuminates a specimen, the question is what does a modification of the SOP of the reflected or transmitted wave reveal about the structure, the composition or the optical properties of this specimen? There are mainly two physical phenomena that can modify the polarization state: an anisotropy of absorption (dichroism) or an anisotropy of the refractive index (birefringence).

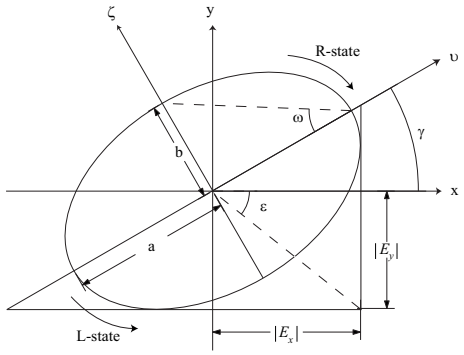


*Figure 1.2: The polarization ellipse. The ellipticity is defined by the ratio of the length of the semi-minor axis to the length of the semi-major axis, $b/a = tan(\omega)$. The ellipse is further characterized by its azimuth $\gamma$ measured counterclockwise from the x axis. $|E_x|$ and $|E_y|$ are the amplitudes of respectively the x and y components of the electric vector $\boldsymbol{E}$ and $tan(\varepsilon)$ is defined by their ratio.*

## Dichroism

A number of crystalline materials absorb more light in one incident plane than another, so that light progressing through the material becomes more and more polarized as it proceeds [Fig. 1.3(a)]. This anisotropy in absorption is called dichroism. There are several naturally occurring dichroic materials, and the commercial material polaroid also polarizes by selective absorption. A famous application of such Polaroid$^{TM}$ is the sunglasses. These sunglasses transmit only vertically polarized light, therefore the intensity of the unpolarized sun light is reduced after passing through the glasses. Furthermore, the light partially horizontally polarized after a reflection on the ground (in particular on water surfaces) is filtered by the glasses [Fig. 1.3(b)]. We present here an example of anisotropy for orthogonal linear polarizations, but an anisotropy can occur with the circular R-state and L-state polarizations. In this case, this anisotropy is called circular dichroism.

The evaluation of the dichroism property of a specimen can be done simply by illuminating it with a linear polarized light oriented at $45^o$ and by measuring $\varepsilon$.

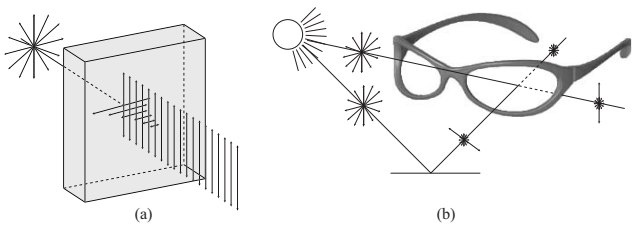


*Figure 1.3: (a) Dichroic material, absorption of the horizontal linear polarization; (b) application of polaroid for sunglasses.*

### Birefringence

The birefringence is a property of anisotropic materials which possess different refractive indices according to the polarization of light passing through the material. As shown in Ref. [Sal91], the refractive indices are related to the electric permittivity tensor $\epsilon$ that expresses physical characteristics of the material. In a linear anisotropic dielectric medium (a crystal for example), the components of the electric displacement $\boldsymbol{D}$ are related to the electric field $\boldsymbol{E}$ with the equation:

$$D_j = \sum_i \epsilon_{jk} E_k. \tag{1.12}$$

It can be shown that a coordinate system, for which the off-diagonal elements $\epsilon_{jk}$ of the dielectric tensor vanish can always be found, so that:

$$D_j = \epsilon_j E_j. \tag{1.13}$$

with $j = 1, 2, 3$. This coordinate system will be assumed to lie along the principal axes of the crystal. The permittivites $\epsilon_1$, $\epsilon_2$ and $\epsilon_3$ correspond to the refractive indices

$$n_j = \left(\epsilon_j/\epsilon_0\right)^{1/2}, \tag{1.14}$$

known as the principal refractive indices ($\epsilon_0$ is the permittivity of free space). An index ellipsoid (Fig. 1.4) can be defined to represent geometrically the electric permeability tensor $\eta = \epsilon_0 \epsilon^{-1}$. Considering the general case of a plane wave propagating along an arbitrary direction defined by the unitary vector $\boldsymbol{u}$, it can be shown first that the two normal modes are linearly polarized waves. Secondly the refractive indices $n_a$ and $n_b$ and the directions of the vectors $D_a$ and $D_b$ correspond respectively to the half-lengths and the directions of the major and minor axes of the index ellipse (intersection between the index ellipsoid and the plane passing through the origin and normal to $\boldsymbol{u}$). The vectors $E_a$ and $E_b$ are determined by use of Eq. 1.13.

We study now the particular case of light travelling along a principal axis of a crystal. We assume that the illuminating light is linearly polarized at $45^o$ and propagates along the z direction. This wave can be analyzed as a superposition of two linearly polarized components in the normal modes direction $x$ and $y$. The respective velocities in the crystal are $c_o/n_1$ and $c_o/n_2$. They undergo therefore different phase shifts $\varphi_x = 2\pi n_1 d/\lambda$ and $\varphi_y = 2\pi n_2 d/\lambda$ after propagating a distance $d$. Their phase difference is

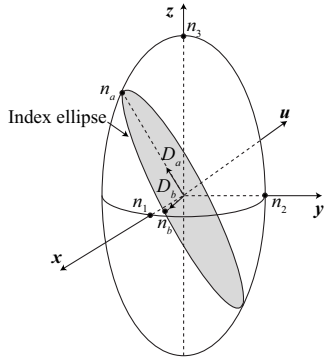


*Figure 1.4: The index ellipsoid. The coordinates (x,y,z) are the principal refractive indices of the crystal. Normal modes are determined from it.*

therefore:

$$\Delta\varphi = \frac{2\pi}{\lambda}\Delta n, \tag{1.15}$$

where $\Delta n = (n_2 - n_1)$ is the index difference.

We present above birefringence due to intrinsic anisotropy of the material, but the anisotropy can be a consequence of an applied stress. For example, a substance may change its dielectric constant and consequently, in transparent materials, change its refractive index. This induced optical anisotropy is known as photoelasticity. In a first approximation, the relative change in refractive index is proportional to the difference between the principal stresses (Stress-Optic Law also known as Brewster's Law):

$$(n_2 - n_1) = C_b(\sigma_1 - \sigma_2). \tag{1.16}$$

where $\sigma_1$ and $\sigma_2$ are the principal stresses at some point within the solid and $Cb$ is the relative strain-optic coefficient, which is a property of the photoelastic material used. The phase difference can be also written from Eq. 1.15 and 1.16:

$$\Delta\varphi = \frac{2\pi}{\lambda}C_b(\sigma_1 - \sigma_2). \tag{1.17}$$

The measurement of the phase difference gives information about the crystallographic properties of materials or about stress or strain applied to the material.

### 1.3.3 Polarization Imaging

Polarization imaging is very useful for revealing inner dichroic or birefringent structures or stresses in materials. Different methods are developed to determine the polarization state. For example we can mention

some recent works in optical coherence tomography (OCT) [Boe97, Boe98, Duc99, Hua03, Jia03, Yan03, Kem05] real-time polarization phase shifting system [Kem99], P-NSOM (polarization contrast with near field scanning optical microscopy) [Ume98] among others. These techniques require several measurements to determine the polarization state. Typically several acquisitions for different orientations of birefringent optical components such as polarizers, half wave ($\lambda/2$) and quarter-wave ($\lambda/4$) plates are needed to obtain the Jones parameters [Kli90]. The temporal resolution can be improved by use of a liquid-crystal universal compensator in place of analyzing optics as presented by Oldenbourg with his Pol-Scope [Old95], but the technique still needs several images to reconstruct the SOP. Finally other methods very similar to holographic ones allow to image SOP with a single acquisition [Oka03, Oht94], but their main drawback is a relatively low spatial resolution compared to polarizing-analyzing techniques that can use a microscope objective to improve the spatial resolution.

We propose in Chapters 5 and 6 a new approach, based on digital holographic imaging, which requires a single acquisition. In a recent paper [Beg99], it was shown that using a configuration initially proposed by Lohmann [Loh65], digital holography can be used as a polarization imaging technique. The basic idea is to create a hologram of the specimen by producing the interference between the object wave and two reference waves having perpendicular polarization states. The reconstruction of such a hologram produces two wave fronts, one for each reference wave, or in other words one for each perpendicular polarization state. The implementation of this idea in digital holography consists in using a numerical method to reconstruct the hologram, which is digitally recorded by a CCD camera. The method presented in Ref. [Beg99] only take advantage of the reconstructed amplitude distributions and therefore provides only the parameter $\varepsilon$. Here we apply the reconstruction procedure described in Chapters 2, 3 and 4, to reconstruct the phase information as well as the amplitude. We demonstrate in Chapter 5 that comparing the amplitude and phase distributions associated to the two orthogonal polarization states enables to determine entirely the distribution of SOP at the surface of the specimen. An attractive feature of the method presented here is that the polarization information is obtained simultaneously with the amplitude and phase information. This provides a complete description of the optical field at the surface of the specimen, on the basis of a single image acquisition performed at a frequency depending on the CCD specifications (usually 25 Hz).

# Chapter 2

# Numerical Wavefront Reconstruction

## 2.1 Introduction

Digital holographic microscopy (DHM) is a powerful instrument to study microscopic specimens by retrieving the amplitude and phase of the wave reflected by the specimen or transmitted through it. Phase reconstruction is of particular interest since it enables surface topography measurements with nanometer vertical resolution [Cuc99a]. Several methods are proposed for phase measurements in digital holography. In line techniques [Yam03] use phase shifting procedures that require several hologram acquisitions, at least three, and additional means, such as a piezoelectric transducer, for controlling the phase of the reference wave. In off-axis configurations, Schnars *et al.* [Sch94a] have demonstrated the possibility to measure specimen deformations by evaluating the phase difference between two states of the specimen. However, this double exposure technique does not give the absolute phase introduced by the specimen.

A solution for absolute phase measurements is proposed by Cuche *et al.* in 1999. They introduce the concept of digital reference wave [Cuc99a], that compensates the role of the reference wave in an off-axis geometry, and the concept of digital phase mask [Cuc99b, Cuc00b], which is introduced to compensate for the wavefront deformation associated to the use of a microscope objective (MO). These two quantities are defined numerically as arrays of complex numbers, computed using a set of parameters, called phase reconstruction parameters, whose values must be precisely defined so that these computed data fit as close as possible their experimental equivalences. This approach enables absolute phase reconstruction, with a single hologram acquisition. However, as proposed initially, the procedure for the

phase reconstruction parameters adjustment was not automated and required a prior knowledge of the parameters values, making the method not user friendly.

Ferraro *et al.* [Fer03b] propose in 2003 to use a reference hologram taken in a flat part of the specimen, and a subtraction procedure for aberrations compensation. This simple technique performs efficiently if the experimental presence of parasitic conditions (vibrations, drifts,...) are well controlled, but fails in providing precise measurements in most of the situations, and is therefore not adapted for most practical applications. In the same year, Allaria *et al.* proposed in Ref. [All03] to determine the reference wave components by a transform-based method for fringe pattern analysis [dN98]. But this method does not achieve a complete adjustment of the phase reconstruction parameters.

In this chapter we propose a new approach that merges the digital reference wave and the digital phase mask in a single entity, whose computation is now performed by an automated, simple and fast procedure.

### 2.1.1 Experimental Configurations

Two main configurations exist for the implementation of DHM: a first one (Fig. 2.1) for reflection imaging and a second one (Fig. 2.2) for transmission imaging in lensless (a) or microscope (b) configuration. In both cases the basic architecture is that of a modified Mach-Zehnder interferometer. The light source depends on applications, in Refs. [Cuc99a,Cuc99b] a HeNe laser is used, but lower coherence sources can also be used [Mas03, Mas05]. The combination of a neutral density filter, a half-wave plate and a polarizing beam splitter are used for the adjustment of the intensities in the reference and object arms.

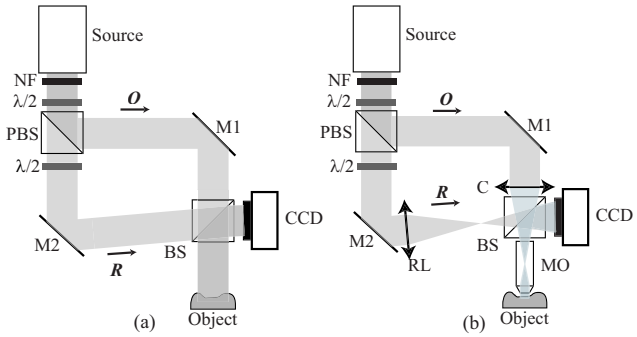


*Figure 2.1: Reflection Setups. (a) Lensless configuration, (b) Microscope configuration. PBS, polarizing beam splitter; BS, beam splitter, λ/2, half-wave plate; M1, M2 mirrors; C, lens used as condenser that focalized in the back focal lens of the microscope objective (MO); RL, reference lens; NF, neutral filter.*

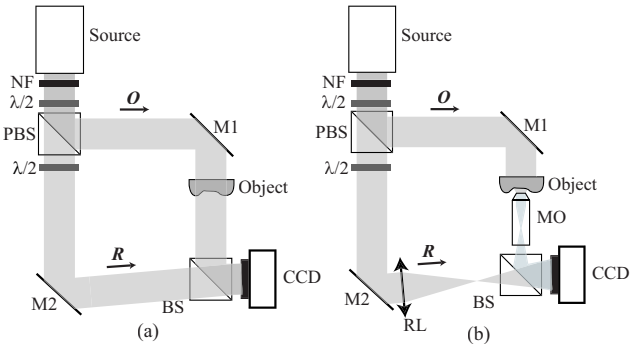


*Figure 2.2: Transmission Setups. (a) Lensless configuration, (b) Microscopic configuration. BS, PBS, polarizing beam splitter;BS, beam splitter, λ/2, half-wave plate; M1, M2 mirrors; MO, microscope objective and RL, reference lens.*

In both microscope configurations, a MO collects the object wave $\boldsymbol{O}$ transmitted or reflected by the specimen, and produces a magnified image of the specimen behind the CCD camera at a distance $d$ (Fig. 2.3). As explained in details in Ref. [Cuc00d], this situation can be considered to be equivalent to a holographic configuration without MO with an object wave $\boldsymbol{O}$ emerging directly from the magnified image of the specimen and not from the specimen itself. Very high resolution can be obtained by MO with a high numerical aperture (NA). Indeed, the role of this high NA MO is to provide a simple mean to adapt the sampling capacity of the camera to the information content of the hologram [Mar03]. As illustrated in Fig. 2.3, a lens or a MO achieve a reduction of the $K_x$, $K_y$ components of the $\boldsymbol{K}$ vector components in the specimen plane perpendicular to the optical axis. The reduction factor is given by the magnification of the MO. The new components $K'_x$, $K'_y$ of the $\boldsymbol{K'}$ wavevector of the beam after having crossed the MO can be made as small as required by the Shannon theorem applied to the sampling capacity dictated by the pixel size of the camera. Using a high magnification objective, the match can be optimized. At the same time, by maximizing the NA, the transverse resolution can be pushed to the limit of diffraction and sub-micron resolution can be easily achieved (ordinarily better than 600nm).

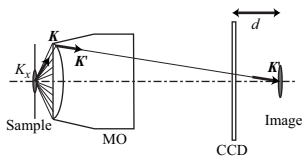


*Figure 2.3: Use of a lens or microscope objective to match the sampling capacity of a CCD placed in the plane of the hologram with the spatial spectrum of the object.*

At the exit of the interferometer the interference between the object wave $\boldsymbol{O}$ and the reference wave $\boldsymbol{R}$ creates the hologram intensity of Eq. 1.1.

A lens could be introduced in the reference arm (RL) to produce a spherical reference wave with a curvature in the CCD plane very similar to the curvature induced by the MO. This permits to have a hologram composed with equal spaced straight fringes. This hologram is digitalized and recorded by a black and white CCD camera and then transmitted to a computer. The digital hologram $I_H(k,l)$ is an array of N x N (usually 512 x 512 or 1024 x 1024) 8-bit-encoded numbers resulting from the two dimensional sampling of $I_H(x,y)$ by the CCD camera:

$$I_H(k,l) = \int_{k\Delta x-\Delta x/2}^{k\Delta y+\Delta y/2} \int_{l\Delta y-\Delta y/2}^{l\Delta y+\Delta y/2} I_H(x,y)dxdy. \tag{2.1}$$

where $k$,$l$ are integers and $\Delta x$, $\Delta y$ define the sampling intervals in the hologram plane (pixel size). A hologram of an USAF test target recorded with a reflection setup is presented in Fig. 2.4.

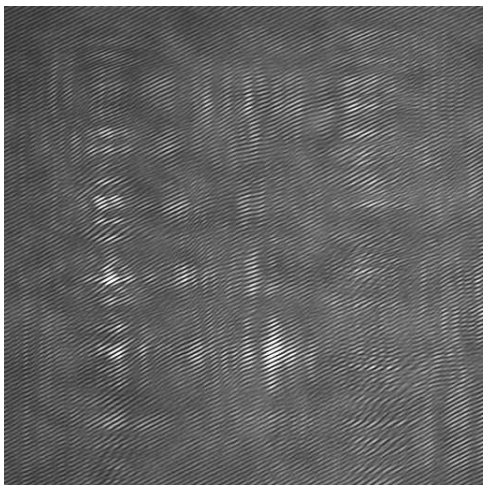

*Figure 2.4: Hologram of an USAF test target recorded on a reflection setup.*

### 2.1.2 Sampling

Digitalization of the reconstruction process presents numerous advantages, but also some drawbacks due to the sampling of the signal. This sampling implies a limitation on the resolution of the reconstructed image. The cut-off spatial frequency of the CCD, $\nu_{\max}$, depends on the sampling step $\Delta x$ given by the pixel size of the CCD camera. The Nyquist relation gives the cut-off frequency:

$$\nu_{\max} = \frac{1}{2\Delta x}. \tag{2.2}$$

This means that the angle $\theta$ between two planes waves in off-axis geometry may not exceed the maximal value $\theta_{\max}$:

$$\theta \leq \theta_{\max} = \frac{\lambda}{2\Delta x}. \tag{2.3}$$

## 2.2 Hologram Preprocessing

### 2.2.1 Numerical Apodization

Truncation of the recorded hologram arises from the finite size of the CCD camera detector. In coherent optics, diffraction by sharp edges induces spatial fluctuation of the transmitted optical field. In our case, the truncated hologram gives rise to fluctuations of the reconstructed amplitude and phase distributions when propagated. Several methods are developed to attenuate these undesired undulations [Mil86, Jar93, Dub02b]. The method used in this work is the apodization method proposed by E. Cuche *et al.* in Ref. [Cuc00c]. It is based on the multiplication of the hologram by an apodized aperture. The apodization profile consists in a cubic spline calculated to reduce the residual fluctuations to an insignificant level.

### 2.2.2 Spatial Frequencies Filtering

As already presented in Section 1.2.1, let us consider an off-axis hologram recorded with an object wave $\boldsymbol{O}$ in normal incidence with respect to the hologram plane and with a reference wave of the form:

$$\boldsymbol{R}(x, y) = \sqrt{I_{\boldsymbol{R}}} \exp(ikx \sin\theta), \tag{2.4}$$

where $k = 2\pi/\lambda$ is the wavenumber and $\theta$ is the angle between the reference wave and the normal to the hologram. The intensity on the hologram plane becomes:

$$I_H = I_{\boldsymbol{R}} + I_{\boldsymbol{O}} + \sqrt{I_{\boldsymbol{R}}} \exp(-ikx \sin\theta)\, \boldsymbol{O} + \sqrt{I_{\boldsymbol{R}}} \exp(ikx \sin\theta)\, \boldsymbol{O}^*, \tag{2.5}$$

If we consider the Fourier transform of this hologram, the influence of the two phase factors $\exp(\pm ikx \sin\theta)$ can be interpreted as a shift of the spatial frequencies associated to the real and to the virtual images. The spatial frequencies of the zero order $[I_{\boldsymbol{R}} + I_{\boldsymbol{O}}(x, y)]$ are located in the center of the Fourier plane and the spatial frequencies of the interference terms lie hereby different carrier frequencies located symmetrically with respect to the center of the Fourier plane: $-ikx \sin\theta$ for the virtual image

and $+ikx\sin\theta$ for the real image. The spectral separation of the different components of the hologram suggests that the extraneous terms of the reconstructed wavefront can be spatially filtered. In digital holography, this procedure can be performed digitally by multiplying the computed Fourier transform of the hologram with a numerically defined mask, as described by E. Cuche *et al.* in Ref. [Cuc00d]. The mask eliminates all spatial frequencies except those of the interference terms of interest. It is composed of transparent and opaque windows of various shapes and sizes. In most cases, the design of the mask is done manually on the amplitude of the Fourier transform of the hologram. The filtering allows the suppression of the orders out of interest and eventual parasitic interferences. An illustration of this procedure is presented in Fig. 2.5. The reconstruction process used for (d-f) is explained in Section 2.6.1.

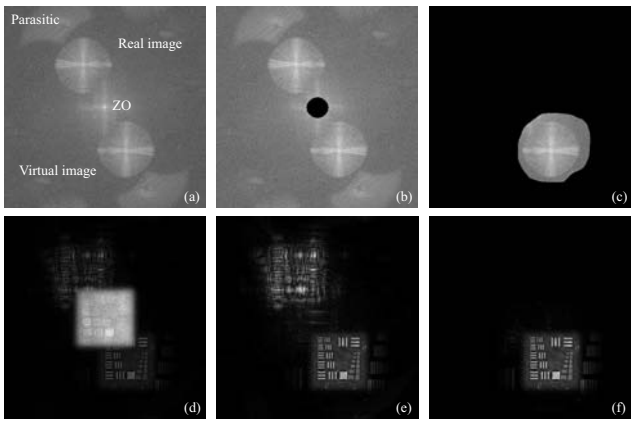


*Figure 2.5: Filtering process:(a) is the amplitude of the Fourier transform of the hologram presented in Fig. 2.4. The frequencies of the different orders of diffraction and of parasitic interference are visible; (b) Zero order filtering and (c) real image and parasitic frequencies filtering. (d), (e) and (f) are the respective amplitude reconstructed image obtained with the filtering (a),(b) and (c).*

## 2.3 Former Algorithm of Reconstruction

In Ref. [Cuc99b], the algorithm for hologram reconstruction, was formulated as follows:

$$\begin{aligned}\Psi(\xi,\eta) =& \Phi(\xi,\eta)\cdot\frac{\exp(i2\pi d/\lambda)}{i\lambda d}\exp\left[\frac{i\pi}{\lambda d}(\xi^2+\eta^2)\right]\cdot \\ & \iint \boldsymbol{R}_D(x,y)I_H(x,y)\exp\left[\frac{i\pi}{\lambda d}\left((x-\xi)^2+(y-\eta)^2\right)\right]dxdy.\end{aligned} \tag{2.6}$$

This expression describes the Fresnel propagation of the reconstructed wavefront $\Psi$ over a distance $d$, from the hologram plane $0xy$ to the observation plane (or reconstruction plane) $0\xi\eta$. The digital reference wave $\boldsymbol{R}_D$ introduced in Ref. [Cuc99a], and the digital phase mask $\Phi$ introduced in Ref. [Cuc99b] play a major role in the phase reconstruction. $\boldsymbol{R}_D$ is defined as a computed replica of the experimental reference wave $\boldsymbol{R}$. Assuming an hologram recorded in the off-axis geometry with a plane reference wave, $\boldsymbol{R}_D$ is written:

$$\boldsymbol{R}_D(x,y) = \exp\left[i\frac{2\pi}{\lambda}(k_x x + k_y y) + i\varphi(t)\right], \tag{2.7}$$

where the parameters $k_x$, $k_y$ define the propagation direction, and $\varphi(t)$ the phase delay between the object and reference waves, which varies during time due to external perturbations, such as mechanical vibrations. As explained in Ref. [Cuc99a], for proper phase reconstruction, the $k_x$ and $k_y$ values must be adjusted, so that the propagation direction of the computed wave-front $\boldsymbol{R}_D$ fits the propagation direction of the experimental wave $\boldsymbol{R}$. As explained in Ref. [Cuc99b], the role of $\Phi$ is to compensate for the wavefront curvature that appears when a MO is used to improve the transverse resolution. If we assume a monochromatic illumination, the relation between the optical field $U_i(x_i, y_i)$ in the image plane and $U_0(x_0, y_0)$ in the object plane can be described as follows:

$$\boldsymbol{U}_i(x_i,y_i) = \int\int \boldsymbol{h}(x_i,y_i;x_0,y_0)\,\boldsymbol{U}(x_0,y_0)\mathrm{d}x_0\mathrm{d}y_0, \tag{2.8}$$

where $\boldsymbol{h}(x_i, y_i; x_0, y_0)$ is the amplitude point-spread function. If the image plane and the object plane form an object-image relation,

$$\frac{1}{d_i} + \frac{1}{d_0} = \frac{1}{f}, \tag{2.9}$$

$\boldsymbol{h}(x_i, y_i; x_0, y_0)$ can be written as follows (in two dimensions, $x$ and $z$, for simplicity) [Goo68]:

$$\begin{aligned}\boldsymbol{h}(x_i;x_0) =& B\exp\left[\frac{i\pi}{\lambda d_i}x_i^2\right]\exp\left[\frac{i\pi}{\lambda d_0}x_0^2\right]\cdot \\ & \int P(x_\phi)\exp\left[\frac{-i2\pi}{\lambda}\left(\frac{x_0}{d_0}+\frac{x_i}{d_i}\right)x_\phi\right]\mathrm{d}x_\phi,\end{aligned} \tag{2.10}$$

where $Ox_\phi$ is the coordinate of the MO plane, $P(x_\phi)$ is the pupil function of the MO, and $B$ is a complex constant. Under the assumption of

a perfect imaging system of magnification $M = d_i/d_0$, for which a point of coordinates $(x_0, y_0)$ in the object plane becomes a point of coordinates $(x_i = -Mx_0, y_i = -My_0)$ in the image plane, the integral in Eq. 2.10 can be approximate by a Dirac $\delta$ function. If we replace $x_0$ with $-x_i d_0/d_i$ in the quadratic phase term preceding the integral, we can write

$$\begin{aligned}\boldsymbol{h}(x_i, y_i; x_0, y_0) =& B \exp\left[\frac{i\pi}{\lambda d_i}\left(1 + \frac{d_0}{d_i}\right)(x_i^2 + y_i^2)\right] \cdot \\ & \delta(x_i + Mx_0, y_i + My_0). \end{aligned} \tag{2.11}$$

In other words, Eq. 2.11 means that the image field is a magnified replica of the object field multiplied by a paraboloidal phase term. For our purpose here it also means that the phase curvature can be corrected by multiplication of the reconstructed wave front with the complex conjugate of the phase term that precedes the $\delta$ function in Eq. 2.11. In Ref. [Cuc99b], a simple quadratic model is used for computation:

$$\Phi(\xi, \eta) = \exp\left[\frac{-i\pi}{\lambda C}(\xi^2 + \eta^2)\right], \tag{2.12}$$

where $C$ is the parameter that has to be adjusted to compensate for this curvature. The reconstruction procedure of Eq. 2.6 involves four parameters: $k_x$, $k_y$ and $C$, for phase reconstruction, and the reconstruction distance $d$ for image focusing. This formulation suffers from several drawbacks:

- i) As the digital reference wave is located inside the Fresnel integral, changing the $k_x$ and $k_y$ shifts the reconstructed images in the observation plane.
- ii) The model used to compute the digital phase mask is limited to the second order, and fails therefore in compensating for higher order aberrations (e.g. astigmatism and spherical).
- iii) Adjusting manually the $k_x$, $k_y$ and $C$ parameters is a complex task that requires expertise and a prior knowledge of their values.

We will describe how the reconstruction procedure can be improved in order to suppress these drawbacks. We present in the present chapter a solution for avoiding the shift of the image by demonstrating that the digital reference wave can be put outside the Fresnel integral. Then, an automatic procedure to adjust the reconstruction parameters is presented by generalizing the definition of the digital phase mask as a Numerical Parametric Lens (NPL). The compensation for higher order aberrations is discussed in Chapters 3 and 4.

## 2.4 Reference Outside Fresnel Integral

We will demonstrate here that the digital reference wave $\boldsymbol{R}_D$ in Eq. 2.6 can be replaced by a pseudo-reference wave $\boldsymbol{R}'$ outside the integral. First, let us define the two dimensional Fresnel Transform $\mathcal{F}_\tau$ of parameter $\tau$ as:

$$\mathcal{F}_\tau[f(x,y)] = \frac{1}{\tau^2}\iint f(x,y)\exp\left\{\frac{i\pi}{\tau^2}\left[(x-\xi)^2+(y-\eta)^2\right]\right\}dxdy \quad (2.13)$$

that has the modulation property [Lie04a]:

$$\begin{aligned}\mathcal{F}_\tau\left[\exp(i2\pi\boldsymbol{\nu}\boldsymbol{x})f(\boldsymbol{x})\right] =& \exp(i2\pi\boldsymbol{\nu}\boldsymbol{\xi})\cdot\exp(-i\pi\boldsymbol{\nu}^2\tau^2)\\ &\cdot\mathcal{F}_\tau[f(\boldsymbol{x})](\xi-\nu_x\tau^2,\eta-\nu_y\tau^2),\end{aligned} \quad (2.14)$$

where $\boldsymbol{x}=(x,y)$, $\boldsymbol{\xi}=(\xi,\eta)$ and $\boldsymbol{\nu}=(\nu_x,\nu_y)$. With this definition, Eq. 2.6 can be written as:

$$\Psi(\xi,\eta) = -i\Phi(\xi,\eta)\cdot\exp(i2\pi d/\lambda)\cdot\mathcal{F}_\tau\left[\boldsymbol{R}_D I_H\right](\xi,\eta), \quad \tau=(\lambda d)^{1/2}. \quad (2.15)$$

Using the property of Eq. 2.14 with $\nu_x = k_x/\lambda$ and $\nu_y = k_y/\lambda$ and Eq. 2.7, Eq. 2.15 becomes

$$\begin{aligned}\Psi(\xi,\eta) =& -i\Phi(\xi,\eta)\cdot\exp(i2\pi d/\lambda)\cdot\exp\left[i\frac{2\pi}{\lambda}(k_x\xi+k_y\eta)+i\varphi(t)\right]\\ &\cdot\exp\left\{-i\pi\lambda d\left[\left(\frac{k_x}{\lambda}\right)^2+\left(\frac{k_y}{\lambda}\right)^2\right]\right\}\cdot\\ &\cdot\mathcal{F}_\tau\left[I_H\right](\xi+k_x d,\eta+k_y d).\end{aligned} \quad (2.16)$$

Writing

$$\varphi'(k_x,k_y,t) = \varphi(t) - \pi d(k_x^2+k_y^2)/\lambda, \quad (2.17)$$

the property of shift-invariance of the Fresnel transform allows to write the wavefront as:

$$\Psi(\xi,\eta) = -i\Phi(\xi,\eta)\cdot\exp(i2\pi d/\lambda)\cdot\boldsymbol{R}'(\xi,\eta)\mathcal{F}_\tau\left[I_H\right](\xi,\eta), \quad (2.18)$$

where $\boldsymbol{R}'$ is the pseudo-reference wave

$$\boldsymbol{R}'(\xi,\eta) = \exp\left[i\frac{2\pi}{\lambda}(k_x\xi+k_y\eta)+i\varphi'(k_x,k_y,t)\right]. \quad (2.19)$$

This means that passing the digital reference wave outside the Fresnel integral is a straightforward operation that conserves the plane wave nature of the wavefront. In other words, for phase reconstruction with DHM, it means that the effects of the off-axis geometry has the appearance of a tilt aberration in the observation plane. This tilt can be compensated by multiplying the reconstructed wavefront with a correcting term calculated with the mathematical model of a plane wave. Compared to the former method [Eq. 2.6], the great advantage is that the adjustment of this pseudo-reference wave does not shift the image in the reconstruction plane and the propagation integral does not need to be recomputed if the parameters $k_x$ and $k_y$ change.

## 2.5 Numerical Parametric Lens

Equation 2.18 describes the reconstruction algorithm as the Fresnel transform of the hologram intensity $I_H$ multiplied by the product of the digital phase mask $\Phi$ with the pseudo digital reference wave $\boldsymbol{R}'$. As $\Phi(\xi,\eta)$ and $\boldsymbol{R}'(\xi,\eta)$ appear now outside the Fresnel integral, they can be merged in a single entity, and the reconstruction algorithm becomes:

$$\Psi(\xi,\eta) = -i \cdot \exp(i2\pi d/\lambda) \cdot \Gamma^I(\xi,\eta)\mathcal{F}_\tau\left[I_H\right](\xi,\eta), \tag{2.20}$$

where according to Eqs. 2.12 and 2.19 we have:

$$\Gamma^I(\xi,\eta) = \exp\left\{\frac{i\pi}{\lambda}\left[2k_x\xi + 2k_y\eta - \frac{\xi^2+\eta^2}{C}\right] + i\varphi'(k_x,k_y,t)\right\}. \tag{2.21}$$

This new formulation of the digital phase mask involves four reconstruction parameters; $k_x$ and $k_y$ for compensating for the tilt aberration due to the off-axis geometry, the phase offset $\varphi'$ for compensating for the phase delay between the object and reference waves, and $C$ for compensating for a quadratic wave-front curvature. This expression for the digital phase mask can be seen as a Numerical Parametric Lens (NPL) placed in the Image plane and can be written in a second order polynomial:

$$\Gamma^I(\xi,\eta) = \exp\left[-i\frac{2\pi}{\lambda}(P_{00} + P_{10}\xi + P_{01}\eta + P_{20}\xi^2 + P_{02}\eta^2)\right]. \tag{2.22}$$

where $P_{hv}$ define a new set of phase reconstruction parameters. The physical constants ($\lambda$, $C$ and $\pi$) are suppressed from the definition of the $P_{hv}$ parameters. But the corresponding physical quantities can be evaluated if

necessary. For example:

$$P_{00} = -\frac{\lambda}{2\pi}\varphi', \tag{2.23}$$

$$P_{10} = -k_x,\ P_{01} = -k_y, \tag{2.24}$$

$$P_{20} = P_{02} = \frac{1}{2C}. \tag{2.25}$$

## 2.6 Discrete Formulation

The numerical calculation of Eq. 2.20 can be performed efficiently following two different discrete formulations of the Fresnel integral. The first one consists in developing the propagation of Eq. 2.20 with a Single Fourier Transform Formulation (SFTF). The second one writes the propagation with a Convolution Formulation (CF).

### 2.6.1 Single Fourier Transform Formulation

As explained in Ref. [Cuc99a], a discrete formulation of Eq. 2.20 involving a Fast Fourier transform (FFT) can be derived directly:

$$\begin{aligned}\Psi(m,n) =& \Gamma^I(m,n)\cdot A\cdot \exp\left[\frac{i\pi}{\lambda d}\left(m^2\Delta\xi^2 + n^2\Delta\eta^2\right)\right] \\ & \cdot \mathrm{FFT}\left\{ I_H(k,l)\exp\left[\frac{i\pi}{\lambda d}\left(k^2\Delta x^2 + l^2\Delta y^2\right)\right]\right\}_{m,n} \\ =& \Gamma^I(m,n)\cdot\Omega(m,n),\end{aligned} \tag{2.26}$$

where $m$ and $n$ are integers ($-N/2 \leqslant m,n \leqslant N/2$), $\Omega(m,n)$ is the reconstructed wavefront in the Fresnel approximation at distance $d$, $A = \exp(i2\pi d/\lambda)/(i\lambda d)$, $\Delta\xi$ and $\Delta\eta$, the sampling intervals in the reconstruction plane are defined as follows:

$$\Delta\xi = \frac{\lambda d}{N\Delta x} \text{ and } \Delta\eta = \frac{\lambda d}{N\Delta y}. \tag{2.27}$$

The discrete formulation of NPL is simply:

$$\begin{aligned}\Gamma^I(m,n) = \exp\big[ -i\frac{2\pi}{\lambda}(P_{00} + P_{10}m\Delta\xi + P_{01}n\Delta\eta + P_{20}m^2\Delta\xi^2 \\ + P_{02}n^2\Delta\eta^2)\big].\end{aligned} \tag{2.28}$$

For computational purposes, the samplings $\Delta\xi$ and $\Delta\eta$ which are related to physical scales are suppressed in Eq. 2.28. The NPL is also written

$$\Gamma^I(m,n) = \exp\left[-i\frac{2\pi}{\lambda}(P_{00} + P_{10}m + P_{01}n + P_{20}m^2 + P_{02}n^2)\right]. \quad (2.29)$$

In this case, the physical definition of the phase reconstruction parameters becomes

$$P_{00} = -\frac{\lambda}{2\pi}\varphi', \quad (2.30)$$

$$P_{10} = -k_x\Delta\xi,\ P_{01} = -k_y\Delta\eta, \quad (2.31)$$

$$P_{20} = P_{02} = \frac{\Delta\xi^2}{2C}. \quad (2.32)$$

### 2.6.2 Convolution Formulation

Equation 2.20 can be written as a convolution:

$$\Psi(\xi,\eta) = A\cdot\Gamma^I(\xi,\eta)\cdot\left\{I_H(x,y)\otimes\exp\left[\frac{i\pi}{\lambda d}(x^2+y^2)\right]\right\}, \quad (2.33)$$

where $\otimes$ is the symbol of convolution. The property of the equivalence between the convolution in the space domain and the multiplying in the frequency domain allows to write:

$$\begin{aligned}\Psi(\xi,\eta) &= A\cdot\Gamma^I(\xi,\eta)\mathrm{FT}^{-1}\left\{\mathrm{FT}\left[I_H(x,y)\right]\cdot FT\left[\exp\left[\frac{i\pi}{\lambda d}(x^2+y^2)\right]\right]\right\}\\ &= A\cdot\Gamma^I(\xi,\eta)\mathrm{FT}^{-1}\left\{\mathrm{FT}\left[I_H(x,y)\right]\cdot\exp\left[-i\pi\lambda d(\nu_x^2+\nu_y^2)\right]\right\},\end{aligned} \quad (2.34)$$

where $\nu_x$ and $\nu_y$ are the coordinates in the spatial frequencies domain and FT the Fourier transform. The discrete formulation of the Eq. 2.34 is

$$\begin{aligned}\Psi(m,n) &= \Gamma^I(m,n)\cdot A\cdot\mathrm{FFT}^{-1}\left\{\mathrm{FFT}\left[I_H\right]\cdot\exp\left[-i\pi\lambda d(\nu_k^2+\nu_l^2)\right]\right\}\\ &= \Gamma^I(m,n)\cdot\Omega(m,n).\end{aligned} \quad (2.35)$$

where $\nu_k = k/(N\Delta x)$, $\nu_l = l/(N\Delta y)$.

### 2.6.3 Advantages and Disadvantages

#### Scaling and time consuming

The two discrete formulations (Eqs. 2.26 and 2.35) have different advantages and disadvantages. First of all, CF is a little more time consuming [Dem74, Sch02], essentially due to one more FFT to compute. On the

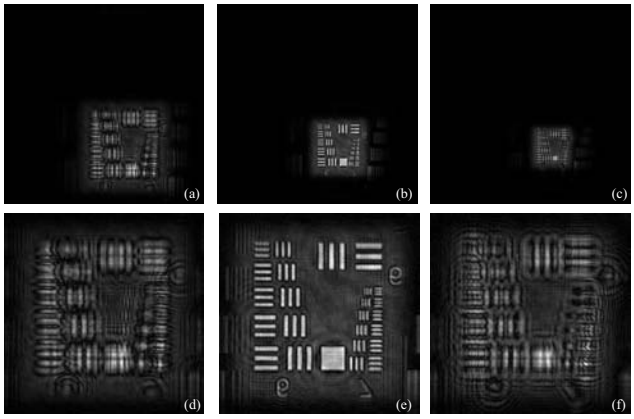


*Figure 2.6: Comparison of the reconstructed amplitude with SFTF (a-c) and CF for the reconstruction distances: $d = 7$ cm (a,d), $d = 11$ cm (b,e) and $d = 15$ cm (c,f).*

other hand, CF has the advantage that the size of the propagated image is at the same scale as the one in the hologram plane; that is not the case for SFTF. Indeed, the propagated and the hologram images have different scales. Considering the hologram sampled in $N$ x $N$ points with a sampling steps $\Delta x$ and $\Delta y$, a reconstruction distance $d$ and a wavelength $\lambda$, the sampling steps $\Delta\xi$ and $\Delta\eta$ are given by Eq. 2.27 (Ref. [Cuc00a])

The image is thus scaled by a factor $\alpha$ given by

$$\alpha_\xi = \frac{N\Delta x^2}{\lambda d} \text{ and } \alpha_\eta = \frac{N\Delta y^2}{\lambda d}. \tag{2.36}$$

At first sight one seems to loose (or gain) resolution by applying SFTF. On closer examination, we recognize that $\lambda d/(N\Delta x)$ corresponds to the resolution limit given by the diffraction theory of optical system: the hologram is the aperture of the optical system with side length $N$ x $\Delta x$. According to the theory of diffraction at a distance $d$ behind the hologram, $\Delta\xi = \lambda d/(N\Delta x)$ is therefore the diameter of the Airy disk (or speckle diameter) in the plane of the reconstructed image, which limits the resolution. This can be regarded as the "automatic scaling" algorithm, setting the resolution of the reconstructed image in the Fresnel approximation always to the physical limit.

Equation 2.36 shows that the scaling depends on the wavelength $\lambda$ and on the reconstruction distance $d$ as shown in Fig. 2.6(a-c). Therefore CF is often preferred when it is necessary to compare reconstruction images performed with different wavelengths (color holography [Kat02], tomography [Mon05] or synthetical wavelength [Gas03]) or different distances of reconstruction [Fig. 2.6(d-f)]. In recent work, Ferraro *et al.* presented in Ref. [Fer04] a zero-padding method permitting to control the image size in SFTF. The drawback of this technique is that the pixel number of the

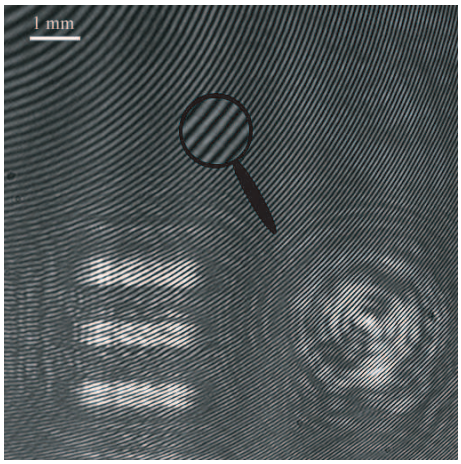


*Figure 2.7: Digital hologram of a USAF test target recorded with a X40 MO in a reflection setup.*

resulting padded holograms are not of the form $N = 2^n$ which is an optimal condition for FFT in terms of time consumption. We will demonstrate in Section 4.4 that scaling is also possible in CF by keeping constant the number of pixel.

## 2.7 Automatic Numerical Parametric Lens Adjustment

### 2.7.1 Principle

We will now describe the iterative procedure that allows the adjustment of the parameters ($P_{00}$, $P_{10}$, $P_{01}$, $P_{20}$, $P_{02}$) defined in Eq. 2.28. To illustrate the procedure, a hologram of a USAF test target taken in a reflection setup [Fig. 2.1(b)] with a X40 MO is used. The hologram is presented in Fig. 2.7. We can see the curvature of the fringes pattern due to the presence of the MO.

After hologram apodization (Section 2.2.1) and a spatial frequency filtering (Section 2.2.2), the reconstructed wavefront $\Omega(m, n)$ (Eqs. 2.26 and 2.35) is computed in SFTF and the Region Of Interest (ROI), corresponding to the location of the real image, is delineated inside the image plane.

Figure 2.8(a) presents the ROI of the phase image of the wavefront $\Omega(m, n)$. As no NPL is applied and as the phase is defined as modulo $2\pi$, the phase seems to be randomly distributed. In fact, this phase reconstruction contains the information that will be used to adjust automatically the phase reconstruction parameters. Indeed the reconstructed phase of Fig. 2.8(a),

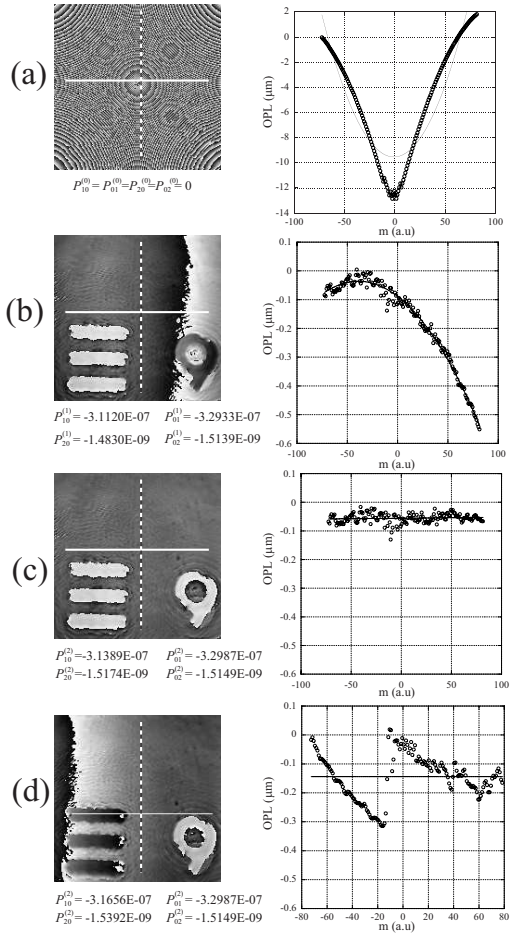


*Figure 2.8: Automatic adjustment of a second order NPL. The left column presents phase images obtained for different obtained values of the parameters computed from the white horizontal and vertical profiles. The right column presents plots of unwrapped optical path length, and fitted curve, for the horizontal direction. (a) Initial phase reconstruction parameters, (b) after first iteration, (c) second iteration. (d) shows that correct parameters can be obtained only with profiles position located in flat regions where the absolute phase contributions of the specimen are constant.*

is the addition of three contributions:

- i) The absolute phase of the specimen
- ii) The tilt aberration due to the off-axis geometry
- iii) The aberrations, or wavefront deformations induced by the setup, in particular the curvature produced by the MO.

The method for the adjustment of the phase reconstruction parameters consists in evaluating the last two contributions, in areas where the specimen contribution is known to be constant, or in other words in a flat reference area located near, or on the specimen. First, no phase aberration is assumed, excepting tilt due to the off-axis geometry and quadratic phase

curvature induced by the MO. The first operation consists in defining two perpendicular lines [see Fig. 2.8(a)], one for each direction $m$ and $n$, respectively the horizontal and the vertical directions (the origin is defined in the center of the ROI). Along both lines, phase profiles are extracted. With strongly aberrated wave fronts such as those presented in Fig. 2.8(a), the phase variation along the selected profiles exceed several times $2\pi$. that produces phase jumps (between $-\pi$ and $+\pi$). These phase jumps are suppressed by the application of a standard 1D phase unwrapping algorithm. The resulting continuous phase profiles are then converted to optical path length [multiplication of the phase value by $\lambda/(2\pi)$] to be fitted with a 1D polynomial function. This conversion is done to compute the parameters independently from the wavelength. Let us assume a correction limited to the second order, and let us define

$$Y_h = a_0 + a_1 x + a_2 x^2 \tag{2.37}$$

$$Y_v = b_0 + b_1 y + b_2 y^2. \tag{2.38}$$

the two optical path length curves fitted along respectively the horizontal, and the vertical profiles. In this case NPL becomes simply:

$$\Gamma^I(m,n) = \exp\left[-i\frac{2\pi}{\lambda}(a_1 m + b_1 n + a_2^2 m^2 + b_2^2 n^2)\right]. \tag{2.39}$$

where $a_1 = P_{10}$ and $b_1 = P_{01}$ compensate for the tilt aberration along respectively the horizontal and vertical directions, and where $a_2 = P_{20}$, and $b_2 = P_{02}$ compensate for a second order wavefront curvature along respectively the horizontal and vertical directions. In principle, this procedure should work immediately, but as shown in Fig. 2.8(b), residual aberrations may persist. The reason for this is that, without correction [Fig. 2.8(a)], or with initial parameters too far from the correct values, the phase distribution varies so rapidly that several phase jumps may occur over distances smaller than one pixel. In this case, the phase unwrapping procedure cannot work properly. To avoid this effect, the procedure described above is applied iteratively, starting from initial values $P_{\alpha\beta}^{(0)}$ provided by a first evaluation. At each iteration, the coefficients of the fitted curve are added to the parameters from the previous iteration. Let us define the fitting curves of the two profiles defined on the reconstructed phase image at iteration $j$:

$$\begin{aligned} Y_h^{(j)} &= a_0^{(j)} + a_1^{(j)} x + a_2^{(j)} x^2 \\ Y_v^{(j)} &= b_0^{(j)} + b_1^{(j)} y + b_2^{(j)} y^2. \end{aligned} \tag{2.40}$$

The new phase reconstruction parameters become ($k = 1, 2$):

$$\begin{aligned} P_{k0}^{(j)} &= P_{k0}^{(j-1)} + a_k^{(j)} \\ P_{0k}^{(j)} &= P_{0k}^{(j-1)} + b_k^{(j)}. \end{aligned} \tag{2.41}$$

The procedure converges very rapidly to the optimal values, and less than four iterations are sufficient in most cases [see Fig. 2.8(c)].

### 2.7.2 Profile Positioning

A key point for retrieving correct and accurate phase distributions is that the phase profiles, with which the polynomial functions are fitted, must be extracted from the image area where the specimen contribution is known to be constant. As shown in Fig. 2.8(d), if the profile is located on a non flat area (step height difference, or phase change on the specimen) the parameters are not adjusted correctly.

This condition represents a limitation for the application of the method. However, as described above, this condition can be satisfied for a very large variety of specimens, especially for microscopic ones.

The first and most simple case occurs when the specimen itself comprises the reference flat surface. This case is valid for most micro- or nano-fabricated structures. With thin films, the reference surface can be the film itself or the substrate on which the deposition is made. With flat layers (manufactured by deposition, evaporation, chemical attach,...) or with all semi-conductor devices, the substrate can be chosen as a flat reference surface.

With biological specimen and organisms (cells and tissues in particular) observed in air or in liquids, the standard preparations used for investigations with other microscopy methods are also well suited. Most of these preparations involve plastic, glass, semi-conductor or metallic surfaces, that offer a lot of opportunities to define a reference surface near the specimen. For example, with cells cultured on plastic or glass surfaces, the reference surface can be defined on the substrate, between the cells. Finally, if the specimen is not specifically attached on a flat surface, it is sufficient in most cases, to put it on a flat specimen holder, which will act as a reference surface. For transmission imaging, the specimen holder must be transparent (e.g. glass or plastic plate). For reflection imaging, the specimen holder must be reflective (e.g. a metallic or dielectric surface).

Finally, if a specific ROI on a specimen does not comprise any possibility to define a flat reference surface, it is possible to adjust the parameters

elsewhere on the specimen, or on the specimen holder. The specimen can then be relocated to obtain an image of the desired ROI.

### 2.7.3 Multi-Profiles Procedure

As explained in the last paragraph, the procedure needs profiles extracted in flat areas. It may occur that only small areas of the field of view are flat. In this case, the procedure for the adjustment of the phase reconstruction parameters may lack precision because the accuracy of the curve fitting procedure depends on the length of the extracted profiles. In other words, the longer the extracted profiles are, the better the procedure for parameter adjustment works.

Figure 2.9 presents the reconstruction of a wafer of quartz micro-lenses imaged with a X10 MO in a transmission setup. Since the lenses with diameter of 230 $\mu$m are distributed in a dense way on a wafer, the flat areas around the lenses are small and do not provide sufficiently long profiles [see Figs. 2.9(a) and (b)]. To avoid this problem, a multi-profiles procedure can be applied.

For simplicity, and as the procedure is identical for the horizontal and the vertical profiles, we will restrict the discussion here to the second order correction along the horizontal direction. Let us define $N_h$ horizontal profiles located at different places $p$, on or around the specimen, where a portion of reference flat surfaces can be defined. The $p^{th}$ profile ($1 \leq p \leq N_h$) has $n_p$ points. Let us define also $Y(x, p)$, the polynomial fitted on the $p^{th}$ profile:

$$Y(x, p) = a_0(p) + a_1(p)x + a_2(p)x^2. \tag{2.42}$$

Because of non-compensated aberrations, different profiles positions, provide different optical path length offsets $a_0(p)$ but the superior order coefficients should be identical as long as the corresponding aberrations are homogeneously distributed in the field of view. A first approach to define the parameters $a_j$ consists simply in calculating the mean value:

$$a_j = \frac{1}{N_h} \sum_{p=1}^{N_h} a_j(p). \tag{2.43}$$

With this method, each profile has the same weight when the coefficient $a_j$ are computed. In other words, the weight attributed to each optical path length value measured along profiles depends on the length of the profile: the shorter the profile length is, the larger the point weight is. Therefore

another method was developed in order to restore an equal share of point in the parameters estimation.

Let us define a system of equations involving each point of each profile. The experimental optical path length values $Y(k_p, p)$ at the position $x(k_p, p)$ corresponding to the $k_p^{th}$ point of the $p^{th}$ profile ($1 \leq k_p \leq n_p$) should be the solution of the linear equation:

$$Y(k_p, p) = a_0(p) + a_1 x(k_p, p) + a_2 x^2(k_p, p), \tag{2.44}$$

where $a_0(p)$ are the respective optical path length offsets of the $p^{th}$ profile as presented before and $a_1$, $a_2$ are the unknown coefficients of the second order polynomial to be determined. Equation 2.44 defines therefore an overdetermined linear system with $N_h + 2$ unknown factors for $N_{eq}$ equations ($N_{eq} = \sum_{p=1}^{N_h} n_p$) that can be solved easily by computing in the least-square sense the solution of

$$\boldsymbol{M} \times \boldsymbol{A} = \boldsymbol{Y}, \tag{2.45}$$

where $\boldsymbol{A}$ is the vector of the $N_h + 2$ coefficients

$$\boldsymbol{A} = \left[ \; a_0(1) \cdots a_0(p) \cdots a_0(N_h) \quad a_1 \quad a_2 \; \right]. \tag{2.46}$$

$\boldsymbol{Y}$ the vector of the $N_{eq}$ phase values

$$\boldsymbol{Y} = [Y(1,1)...Y(n_1,1) \cdots Y(1,p)...Y(n_p,p) \cdots Y(1,N_h)...Y(n_{N_h},N_h)] \tag{2.47}$$

and $\boldsymbol{M}$ the matrix

$$\boldsymbol{M} = \overbrace{\left[\begin{array}{ccccccc}
1 & 0 & 0 & \cdots & 0 & x(1,1) & x^2(1,1) \\
\vdots & \vdots & \vdots & & \vdots & \vdots & \vdots \\
1 & 0 & 0 & \cdots & 0 & x(n_1,1) & x^2(n_1,1) \\
0 & 1 & 0 & \cdots & 0 & x(1,2) & x^2(1,2) \\
\vdots & \vdots & \vdots & & \vdots & \vdots & \vdots \\
0 & 1 & 0 & \cdots & 0 & x(n_2,2) & x^2(n_2,2) \\
 & & \vdots & & & \vdots & \vdots \\
0 & \cdots & 1 & 0 & 0 & x(1,p) & x^2(1,p) \\
\vdots & & \vdots & \vdots & \vdots & \vdots & \vdots \\
0 & \cdots & 1 & 0 & 0 & x(n_p,p) & x^2(n_p,p) \\
 & & \vdots & & & \vdots & \vdots \\
0 & \cdots & \cdots & 0 & 1 & x(1,N_h) & x^2(1,N_h) \\
\vdots & & & \vdots & \vdots & \vdots & \vdots \\
0 & \cdots & \cdots & 0 & 1 & x(n_{N_h},N_h) & x^2(n_{N_h},N_h)
\end{array}\right]}^{N_h+2} \Bigg\} N_{eq}, \tag{2.48}$$

Whatever least-square linear fit method might be used to compute $\boldsymbol{A}$ and therefore to extract the value $a_1$ and $a_2$. The iterative procedure explained for the standard method [see Eqs. 2.40 and 2.41] can be applied to the multi-profiles procedure. As presented by Fig. 2.9, the accuracy of the parameters adjustment increases with the number of profiles. A 2D unwrapping of Fig. 2.9(c) provides a perspective view representation of the lenses wafer [Fig. 2.9(d)].

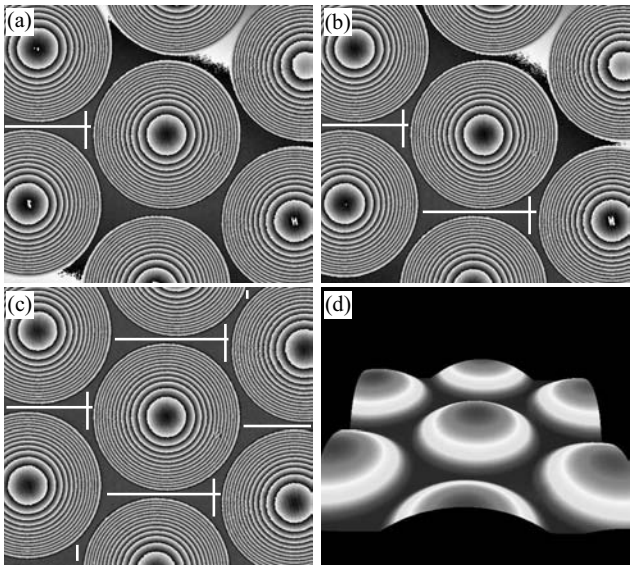


*Figure 2.9: Phase reconstructions of a wafer of quartz micro-lenses recorded in transmission with a X10 MO (field of view 0.5 mm). This figure illustrates a NPL multi-profiles adjustment procedure. The number of extracted profiles (white lines) increases from (a) (2 profiles) to (c) (9 profiles). (d) presents the perspective view of the 2D unwrapping of (c).*

### 2.7.4 Phase offset adjustment

As shown in Eq. 2.30, the parameter $P_{00}$ defines an offset that permits to compensate for the variation of $\varphi'$ originating from the phase delay $\varphi(t)$ between the object and reference waves and the phase shift introduced by the adjustment of $k_x$ and $k_y$ (see Eq. 2.17). $P_{00}$ can be extracted from one of the values $a_0(p)$ of $\boldsymbol{A}$ or the mean value of all of them if all the profiles are defined on the same flat area. The resulting phase along the profile $p$ is also 0 degree after the application of $P_{00} = a_0(p)$. The operator can choose a desired phase offset $\varphi_{off}$ by subtracting this value to the computed $a_0(p)$. The parameter $P_{00}$ is also written:

$$P_{00} = a_0(p) - \frac{\lambda}{2\pi}\varphi_{off}. \tag{2.49}$$

In the case of real-time reconstruction, this solution works only if the automatic adjustment is done for each hologram that is not efficient in terms of time consumption if a high reconstruction rate is desired. Therefore we developed another method to apply a desired phase offset $\varphi_{off}$ independently of the automatic fitting procedure. For this purpose, we define a complex array $\Gamma^{I,off}$ called Phase Offset Array (POA) independent of the wavelength defined as follows:

$$\Gamma^{I,off}(m,n) = \exp[i\varphi_{\text{POA}}] \tag{2.50}$$

that multiplies the computed wavefront $\Psi$ to achieve the offset corrected wavefront

$$\Psi_{off} = \Gamma^{I,off} \cdot \Psi. \tag{2.51}$$

The method to compute $\varphi_{\text{POA}}$ consists in three steps. First, the operator draws a ROI in the field of view where the specimen is known to be flat. Secondly, the histogram of the phase values contained in this ROI is computed. To avoid any problems on the evaluation of mean value inside this ROI due to its modulo $2\pi$ definition [Fig. 2.10(a)], the histogram is defined in the interval [-270;270] degrees by pasting the histogram values in the interval [-180;-90] to the interval [180;270] and the values between [90;180] to the interval [-270;-180] [Fig. 2.10(b)]. Finally the phase mean value $\varphi_{\text{mean}}$ is computed in a large interval centered on the maximum of the peak [gray rectangle in (b)] and the offset parameter $\varphi_{\text{POA}}$ becomes

$$\varphi_{\text{POA}} = -\varphi_{mean} + \varphi_{off}. \tag{2.52}$$

In the followed chapters, we omit the phase offset array in the definition of the reconstructed wavefront to reduce the notation.

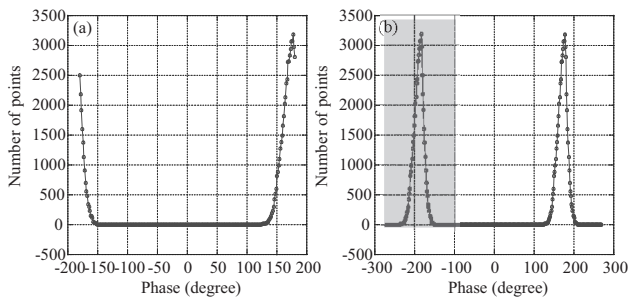


*Figure 2.10: (a) Phase histogram example where the peak position is nearby the extremal values. (b) extended histogram to the intervals [-270;-180] and [180;270], the mean value of the ROI is defined by the values contained in the interval defined by the gray rectangle*

# Chapter 3

# Aberrations Compensation in Image Plane

## 3.1 Introduction

The main difficulty for phase reconstruction in DHM is to separate the phase distribution specifically associated to the specimen from the contributions of the experimental setup. Each constituent of the setup, lenses especially, is a potential source of wavefront deformation. Another important point is the role of the reference wave, because holographic images are reconstructed from wave fronts defined by the product between the object wave and the reference wave. We introduced the concept of numerical parametric lens (NPL) in Chapter 2, that compensates the role of the reference wave and the wavefront deformation associated to the use of a MO. We show in present chapter that a generalized NPL defined with high order polynomials allows to compensate for higher order aberrations. Demonstration will be provided by the introduction of a thick tilted glass plate in the experimental setup. Furthermore, we show that the proposed procedure allows to compensate for the shape of the specimen and provides quantitative aberrations measurements on micro-optics.

## 3.2 Generalized Numerical Parametric Lens

### 3.2.1 Models

The expression of the NPL defined in Eq. 2.22 covers a very limited range of situations. In order to enable the compensation for higher orders aberrations, we introduce here two generalized polynomial formulations. First, a Standard polynomial model for the aberration is used. In this case, NPL is expressed as:

$$\Gamma_S^I(\xi,\eta) = \exp\left[-i\frac{2\pi}{\lambda}\sum_{\alpha=0}^{H}\sum_{\beta=0}^{V} P_{\alpha\beta}\cdot\xi^{\alpha}\eta^{\beta}\right], \tag{3.1}$$

where the index $S$ defined the Standard polynomial model, $P_{\alpha\beta}$ define a set of reconstruction parameters, $H$ and $V$ define the polynomial orders in the horizontal and vertical directions respectively. The discrete formulation of Eq. 3.1 is

$$\Gamma_S^I(m,n) = \exp\left[-i\frac{2\pi}{\lambda}\sum_{\alpha=0}^{H}\sum_{\beta=0}^{V} P_{\alpha\beta}\cdot m^{\alpha}n^{\beta}\right]. \tag{3.2}$$

Secondly, an accurate polynomial model to correct and study the optical aberrations is the Zernike polynomial model. In this model, the NPL is expressed as:

$$\Gamma_Z^I(\gamma,\zeta) = \exp\left[-i\frac{2\pi}{\lambda}\sum_{\alpha=0}^{o} P_{\alpha}\cdot Z_{\alpha}\right], \tag{3.3}$$

where the index $Z$ defines the Zernike polynomial model, $P_\alpha$ is the $\alpha^{th}$ coefficient of the Zernike term $Z_\alpha$ and $o$ the Zernike polynomial order. The terms $Z_\alpha$ form an orthonormal basis in a continuous fashion over the interior of a unit circle that defines the extremum values of $\gamma$ and $\zeta$ and the increment in the discrete case. A description of the Zernike coefficients and polynomial is done in Appendix A. The classification of the Zernike polynomials are arbitrary but in this thesis we choose the same classification used in the Zemax program, as presented in Table A.3.

## 3.3 Automatic Adjustment

### 3.3.1 1D Procedure for Standard Polynomial Model

As described in Section 2.7, the procedure restricted to the second order corrects the so-called tilt and defocusing aberrations. Astigmatism, which is one of the most common aberrations, is already partially corrected, because the wavefront curvature is compensated differently along the horizontal and vertical directions if the computed parameters $P_{20}$ and $P_{02}$ are different. But the method fails if the principal axes defining the astigmatism are not along these directions. Furthermore other standard aberrations such as coma or spherical, as well as higher order aberrations cannot be properly addressed by a second order correction.

A first approach for higher order corrections consists simply in increasing the polynomial order of the fit along the horizontal and vertical directions and in applying the same procedure explained in Section 2.7 to compute the phase reconstruction parameters. In the case of one profile procedure, Eq. 2.38 becomes

$$Y_h = a_0 + a_1 x + a_2 x^2 + \ldots + a_\alpha x^\alpha + \ldots + a_H x^H \tag{3.4}$$

$$Y_v = b_0 + b_1 y + b_2 y^2 + \ldots + b_\beta y^\beta + \ldots + b_V y^V . \tag{3.5}$$

where $H$ and $V$ are respectively the polynomial order for the horizontal and vertical directions. The computed parameters are therefore $P_{\alpha 0} = a_\alpha$ and $P_{0\beta} = b_\beta$ ($\alpha \leq H$, $\beta \leq V$).

In case of multi-profile procedure, increasing the polynomial order consists in keeping the same vector $\boldsymbol{Y}$ of measured phase value (see Eq. 2.47) and in writing the vector of the $(N_h + H)$ unknown factors as:

$$\boldsymbol{A} = \left[ \; a_0(1) \cdots a_0(p) \cdots a_0(N_h) \quad a_1 \quad a_2 \cdots a_H \; \right], \tag{3.6}$$

The matrix $\boldsymbol{M}$ is constructed as Eq. 2.48 by increasing its order. Using the same general least-square linear fit allows to compute the parameters $P_{\alpha 0}$ and $P_{0\beta}$ ($\alpha \leq H$, $\beta \leq V$).

However, according to the general formulation of the NPL [Eq. 3.2], this procedure is effective only for the calculation of $P_{\alpha 0}$ and $P_{0\beta}$ terms. For the $P_{\alpha\beta}$ cross-terms correction, it is necessary to extract others profiles in the image. The definition of these profiles and the solution of the corresponding equations systems allow to compute higher order crossed-terms. The details of the calculus are given in Appendix B.

**Procedure validation**

To illustrate the procedure for higher orders and crossed terms corrections, a theoretical and an experimental aberrated phase distributions are studied. First, we define arbitrary a polynomial phase distribution of fourth order, written as

$$\varphi(m,n) = \sum_{\alpha+\beta=1}^{\alpha+\beta=4} C_{\alpha\beta} m^{\alpha} n^{\beta}, \tag{3.7}$$

is computed with $-N/2 \leq m,n < N/2$ ($N = 220$) and with the coefficients: $C_{00} = 0$, $C_{10} = 1$, $C_{01} = -1.1$, $C_{20} = -1 \cdot 10^{-2}$, $C_{02} = -1.1 \cdot 10^{-2}$, $C_{30} = -1 \cdot 10^{-7}$, $C_{03} = 1.1 \cdot 10^{-7}$, $C_{40} = -1 \cdot 10^{-9}$, $C_{04} = 1.1 \cdot 10^{-9}$, $C_{11} = -1 \cdot 10^{-4}$, $C_{12} = -1 \cdot 10^{-7}$, $C_{21} = 1.1 \cdot 10^{-7}$, $C_{13} = C_{31} = C_{22} = 0$. Then, this computed phase distribution is wrapped between $-\pi$ and $+\pi$ as shown in the left image of Fig. 3.1(a). The white lines are the selected profiles defined to compute the cross-terms.

Secondly a strongly aberrated experimental configuration is realized by introducing a tilted thick plate between the beam splitter and the CCD camera in the reflection setup [Fig. 2.1(b)]. The analytical expressions for the corresponding aberration are described in the Ref. [Bra97]. A hologram of a mirror is recorded with a X10 MO. The right image of Fig. 3.1(a) presents the phase reconstruction of this hologram without aberration compensation.

Figure 3.1 presents the computed phase reconstructions for the theoretical specimen (left column) and for the experimental specimen (right column), for increasing orders of correction from top to bottom. The offset parameter $P_{00}$ is adjusted to have a mean phase value on the entire image equal to zero. The efficiency of the correction is evaluated by measuring the Standard Deviation (std) of the phase distribution over the entire field of view. As can be seen, std decreases rapidly, but the perfect correction for the theoretical specimen ($std = 0$) is achieved only when the polynomial order of the NPL is equal to the polynomial order of the generated phase distribution, where the procedure computes $P_{\alpha\beta} = (\lambda/2\pi)C_{\alpha\beta}$ for all phase reconstruction parameters.

In the experimental case, the aberrations are compensated up to a std of 5 degrees as shown in the right image of Fig. 3.1(e). In this case, the procedure computes the following coefficients values: $P_{10} = 3.1382 \cdot 10^{-7}$, $P_{01} = -3.1735 \cdot 10^{-7}$, $P_{20} = -1.0635 \cdot 10^{-9}$, $P_{02} = -1.0726 \cdot 10^{-9}$, $P_{30} = -3.4615 \cdot 10^{-14}$, $P_{03} = 3.3820 \cdot 10^{-14}$, $P_{40} = -1.0333 \cdot 10^{-16}$, $P_{04} = 1.1985 \cdot 10^{-16}$, $P_{11} = -1.3596 \cdot 10^{-11}$, $P_{12} = -4.6197 \cdot 10^{-14}$, $P_{21} = 3.4313 \cdot 10^{-14}$. The

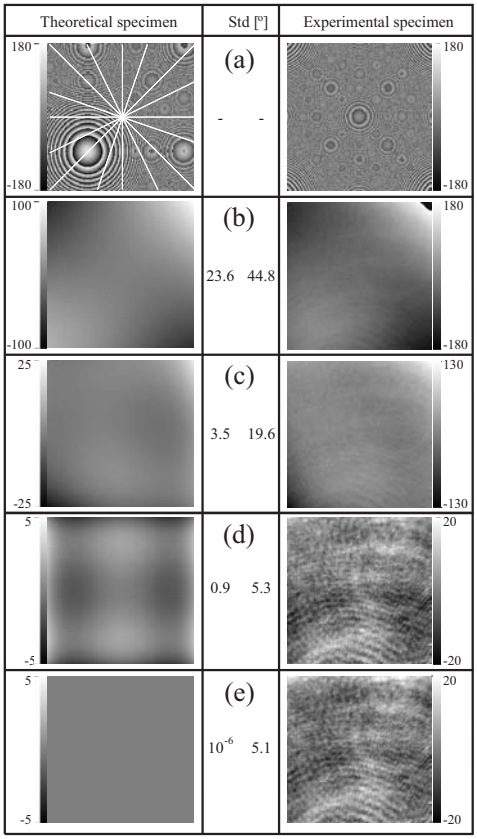


*Figure 3.1: Phase reconstructions for increasing order of a polynomial NPL. The computed coefficients are: (a) $P_{00}$ , (b) adding $P_{10}$, $P_{01}$, $P_{20}$ and $P_{02}$; (c) adding $P_{11}$; (d) adding $P_{\alpha\beta}$ with $\alpha + \beta = 3$ and (e) adding $P_{40}$ and $P_{04}$. Left column: compensation for a computed phase distribution. Right column: phase distributions reconstructed from a hologram recorded with a strongly aberrated microscope. The accuracy of the aberration compensation is measured by the computation of the phase distribution standard deviation evaluated over the entire field of view.*

residual noise may have several origins, such as uncorrected aberrations, surface defects on the mirror or on optical components of the microscope, as well as spatial phase fluctuations caused by dusts, parasitic reflections or diffraction effects.

A mirror is an ideal specimen because long profiles can be taken to evaluate the phase reconstruction parameters. As presented in Fig. 3.2, coefficients evaluated using a mirror can be used as calibrated values to correct high order and crossed terms aberrations for further uses of the microscope. Figure 3.2 presents the phase reconstructions, in 3D perspective views, obtained from a hologram recorded with a USAF 1950 resolution test target and with different phase reconstruction parameters. Figures 3.2(a) presents the reconstructed phase by computing the four parameters $P_{j0}$ and $P_{0j}$ ($j = 1$ to 2, second order correction) from flat areas on the specimen. As for the mirror, we see that these parameters do not compensate for the

aberrations due to the introduced tilted plate. Figure 3.2(b) presents the reconstructed phase computed with the phase reconstruction parameters, up to order four, obtained previously with the mirror. Phase jumps appear because the tilt has changed between the two specimens. Figure 3.2(c) presents the result after application of a first order procedure (tilt compensation) on the phase distribution of Fig. 3.2(b).

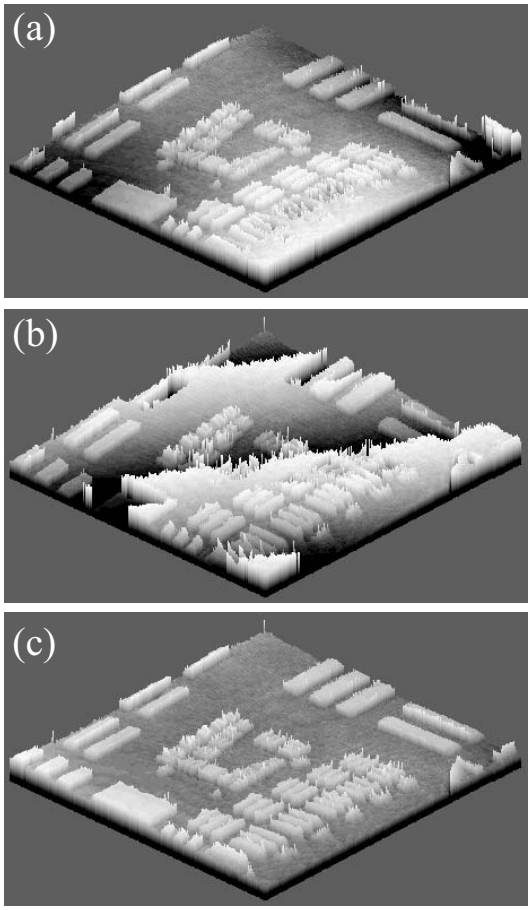


*Figure 3.2: Phase reconstructions in perspective view of a USAF test target obtained: (a) by computing a second order NPL with the method presented in Fig. 2.8; (b) by using the phase reconstruction parameters (cross and non-cross-terms up to order four) calibrated using a mirror [see Fig. 3.1(e)] and (c) by adding a first order (tilt compensation) procedure to the phase distribution of (b).*

### 3.3.2 2D Fitting Procedure

As shown in the Fig. 3.2, the main drawback of the single profiles and multi-profiles procedures is that a calibration with a flat object is necessary to adjust the cross-terms parameters. Therefore we developed a more general fitting method that considers two-dimensional areas (known to be flat) of

the specimen instead of profiles. This procedure will be applied for the two models presented in Section 3.2.1.

In assumed flat areas $F$ [inside white rectangle in Fig. 3.3 (a)], $N_{pts}$ points are selected. The $N_{pts}$ measured optical path length values $Y(\gamma, \zeta)$ $[(\gamma, \zeta) \in F]$ satisfy the following equations depending of the model used (Eqs. 3.2 and 3.3):

$$Y(\gamma, \zeta) = \sum_{\alpha=\beta=0}^{\alpha+\beta=o} a_{\alpha\beta} \cdot S_{\alpha\beta}, \text{ where } S_{\alpha\beta} = \gamma^{\alpha}\zeta^{\beta} \tag{3.8}$$

$$Y(\gamma, \zeta) = \sum_{\alpha=0}^{\alpha=o} a_{\alpha} \cdot Z_{\alpha}, \tag{3.9}$$

where $\gamma$ and $\zeta$ are computed from the pixel position $(m, n)$ to satisfy the condition that $F$ is inscribed in an unit circle; $o$ is the polynomial order. The Eqs. 3.8 and 3.9 define overdetermined linear systems with $N_{pts}$ equations and respectively a number of unknown coefficients $(o^2 + 3o + 2)/2$ and $o+1$. These systems are solved by computing in the least-square sense the solution of

$$\boldsymbol{M} \times \boldsymbol{A}_M = \boldsymbol{Y}, \tag{3.10}$$

where $\boldsymbol{M} = \boldsymbol{S}, \boldsymbol{Z}$ is the matrix of the fitting polynomials (the indexes S and Z are for respectively the standard and Zernike polynomial models), $\boldsymbol{Y}$ is the vector of the measured optical path length values, $\boldsymbol{A}_M$ the vectors of the unknown coefficients.

As presented in Section 2.7, an iterative procedure can be used to adjust the vectors $\boldsymbol{P}_M$ of the phase reconstruction parameters:

$$\boldsymbol{P}_M^{(i)} = \boldsymbol{P}_M^{(i-1)} + \boldsymbol{A}_M^{(i)}. \tag{3.11}$$

It is evident that this procedure fails if there are phase jumps in the areas $F$ due to initial parameters too different from the optimal ones. Therefore a simple procedure is used to define the initial parameters $\boldsymbol{P}_M^{(0)}$. The first step consists in computing initial parameters with the 1D fitting method:

$$\boldsymbol{P}_S^{(0)} = \begin{bmatrix} 0 & P_{10}^{1D} & P_{01}^{1D} & P_{20}^{1D} & P_{02}^{1D} \end{bmatrix}, \tag{3.12}$$

$$\boldsymbol{P}_Z^{(0)} = \begin{bmatrix} 0 & \frac{P_{10}^{1D}}{2} & \frac{P_{01}^{1D}}{2} \end{bmatrix}, \tag{3.13}$$

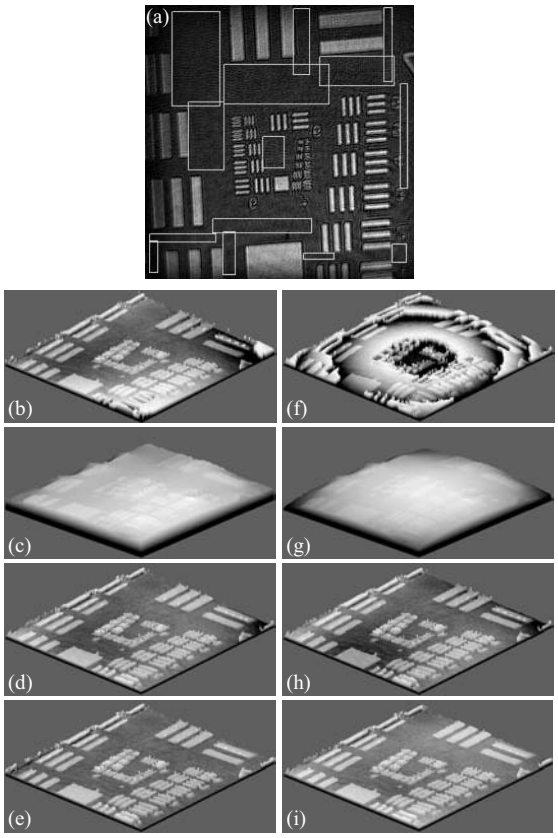


*Figure 3.3: 2D fitting procedure with standard polynomial model (left column) and Zernike polynomial model (right column). (a) is the reconstructed amplitude contrast with the assumed flat areas F inside the white rectangles. (b,f)reconstruction with initial parameters computed with 1D procedure; (c,g) 2D unwrap of (b,f). (d) and (e) are respectively the correction with 6 and 10 adjusted standard polynomial coefficients (o=2,3); (h) and (i) are respectively the correction with 6 and 8 adjusted Zernike polynomial coefficients (o=5,7).*

where $P_{\alpha\beta}^{1D}$ are the parameters adjusted by the 1D fitting procedure [Figs. 3.3 (b,f)].

The second step consists in applying a 2D unwrapping on the resulting reconstructed phase to suppress eventual remaining phase jumps due to aberrations [Figs. 3.3 (c,g)].

Finally, the 2D fitting procedure is applied by increasing the polynomial order if necessary. Figures 3.3 (d,e) and (h,i) present the reconstructed phases obtained with the adjustment of the phase reconstruction parameters in the respectively standard and Zernike polynomial models. The polynomial order used for (d,e) are respectively $o$=2 (6 parameters) and $o$=3 (10 parameters), wheras the one used for (h,i) are respectively $o$=5 (6 parameters) and $o$=7 (8 parameters).

## 3.4 Results and Applications

We demonstrated in this chapter that the NPL and its adjustment allow the reconstruction of the absolute phase with a single acquisition. In this section, we present different applications of this procedure. First, we show that this procedure can be applied to compensate for the specimen curvature itself and therefore to characterize its surface properties, like surface quality or roughness (Section 3.4.1). Finally, the technique is applied to compensate for the curvature of micro-optical components. In particular, the adjusted parameters in Zernike models give quantitative results about micro-lens aberrations (Section 3.4.2).

### 3.4.1 Specimen Curvature Compensation

Surface metrology and quality control, roughness measurements in particular, are important tasks in engineering today. In industry, the most popular techniques to inspect surfaces, and in particular for roughness measurements, are certainly the stylus type devices. They are very sensitive in height measurements and have a good lateral resolution, but the main drawback is that stylus devices perform punctual measurements that require scanning procedures along 1D profiles, making these techniques slow and sensitive to external perturbations. In addition, surface damages may occur as a result of the contact between the probe and the specimen. In recent years, many optical techniques are developed, including light scattering, speckle, fringe projection, and interferometry [Sto94, Ben92, Yam04, Spa02], because they offer the possibility to measure over a larger area in a non-contact way. In addition, optical techniques enable true surface measurements, on 2D surfaces, which are more relevant than 1D profile measurements; first of all because the resulting increase of acquired data is a benefit from the statistical point of view, but also because the resulting 3D description enables direct evaluation of the surface topography.

Among optical techniques, DHM is particularly well adapted for surface metrology since it enables to measure three-dimensional (3D) surface topography with nanometer vertical resolution, with similar performances than classical optical microscopy in terms of transverse resolution and field of view. Compared to other optical techniques, for instance phase shifting or white-light interferometry, DHM presents the advantages of an improved robustness and a higher reconstruction rate (15 images/sec), resulting from the fact that a single hologram acquisition, in the off-axis geometry, is necessary to reconstruct the surface topography. The absence of moving parts,

such as piezoelectric transducers, as well as the use of powerful numerical tools, such as those presented in this chapter, are also key ingredient of DHM, from both the ease of use and cost efficiency.

Furthermore we show here that DHM offers attractive and simple possibilities to compensate for the shape of a specimen by providing a flattened representation of the surface of curved specimens. This is of particular interest within the scope of surface metrology, since reliable surface parameters, such as roughness or texture, can only be obtained if the shape or form contributions can be eliminated from the topographic information. This can be achieved in DHM by a purely software operation based on an identical procedure for parameters adjustment described in this chapter.

### Specimen shape compensation procedure

The principle of the method to compensate for the shape of specimen is identical to the aberration compensation method. A second polynomial NPL $\Gamma^{I,SCL}$, called Shape Compensation Lens (SCL), is introduced in Eqs. 2.26 and 2.35 to produce a shape compensated wavefront:

$$\Psi^{SCL}(m,n) = \Gamma^{I,SCL}(m,n) \cdot \Psi(m,n). \tag{3.14}$$

where the shape compensation lens can be defined in standard or Zernike polynomial models:

$$\Gamma_S^{I,SCL}(m,n) = \exp\left[-i\frac{2\pi}{\lambda}\sum_{\alpha=\beta=0}^{\alpha+\beta=o} P_{\alpha\beta}^{SCL} \cdot m^\alpha n^\beta\right] \text{ or} \tag{3.15}$$

$$\Gamma_Z^{I,SCL}(m,n) = \exp\left[-i\frac{2\pi}{\lambda}\sum_{\alpha=0}^{o} P_{\alpha}^{SCL} \cdot Z_\alpha\right] \tag{3.16}$$

where $P_{\alpha\beta}^{SCL}$ or $P_{\alpha}^{SCL}$ define a new set of coefficients called shape compensation parameters. Here also, the accuracy or the shape of the compensation can be adapted by changing the polynomial orders $o$. The shape compensation parameters can be adjusted automatically by similar procedures that are applied to adjust the phase reconstruction parameters. There is however an important difference between the standard topographic imaging mode and the shape compensation imaging mode, which concerns the position of the profiles (1D procedure) or the areas (2D procedure) from which phase data are extracted for parameters evaluation. For the standard adjustment procedure of the phase reconstruction parameters, the profiles or areas are

positioned in areas of the field of view, where specimen contributions are known to be constant. For shape compensation, phase data are extracted along profiles or areas defined on the specimen itself. The consequence of this is that the fitting procedures provide coefficient values comprising contribution of the specimen shape such as its curvature.

Examples of standard topographic images are presented in Fig. 3.4(a) and in Fig. 3.5(a), for respectively a micro-lenses wafer (MLW)[230 $\mu$m diameter micro-lenses] and a metallic sphere. The real specimen shapes, without $2\pi$ ambiguities, are shown in Figs. 3.4(b) and 3.5(b), which present the corresponding phase distributions after the application of a standard phase unwrapping algorithm.

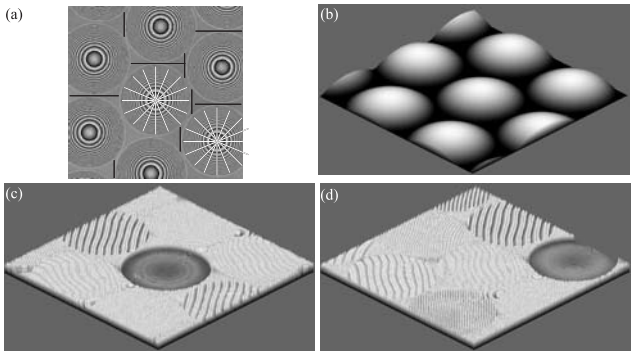


*Figure 3.4: (a) Reconstruction with the adjustment of the phase mask parameters defined on the flat area of the wafer, between the micro-lenses; (b) perspective view of the 2D unwrapped phase image; (c) and (d) perspective views obtained by adjusting the second order shape compensation parameters on respectively the centered and right lower micro-lenses. In (a), the black lines indicate the profiles used for a parameter adjustment in the standard topographic imaging mode, and the white lines indicate the position of the profile used for the shape compensation procedure.*

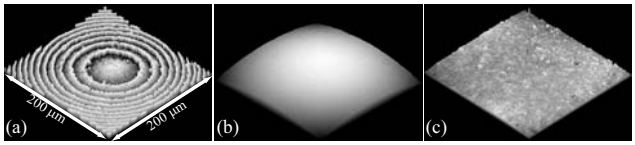


*Figure 3.5: (a) Phase reconstructions of the vertex of a metallic sphere. (b) 2D unwrapped phase image. (c) digitally flattened phase image revealing surface roughness*

The adjustment of the phase reconstruction parameters in Fig. 3.4 (a) is performed according to a multi-segment procedure described in Section 2.7.3, which consists in applying the curve fitting procedure on a series of several profiles positioned on flat regions of the wafer between the locations of the lenses [black lines in Fig. 3.4(a)]. For Fig. 3.5(a), the parameters adjustment is performed thanks to a calibration procedure using a mirror as

specimen, prior application to the metallic sphere, since this specimen does not comprise flat surfaces enabling a proper estimation of signal contributions independent from the specimen. Figures 3.4(c,d) and 3.5(c) present perspective views of phase images obtained by the shape compensation procedure with standard polynomial model. Figures 3.4(c,d) are obtained for profiles positions [see white lines in Fig. 3.4(a)] centered on two different micro-lenses and with the second order of the shape compensation lens without cross-term:

$$\Gamma_S^{I,SCL}(m,n) = \exp\left[-i\frac{2\pi}{\lambda}\left(P_{00}^{SCL} + P_{10}^{SCL}m + P_{01}^{SCL}n + (P_{20}^{SCL})^2m^2 + (P_{02}^{SCL})^2n^2\right)\right]. \quad (3.17)$$

As can be seen in Fig. 3.6(a), the procedure compensates only partially the lens shape. A ring pattern appears that results from the difference between the expected spherical shape of the lens, and the parabolic model used for calculating the shape compensation lens. If desired, the shape compensation can be improved by increasing the standard polynomial order of the shape compensation lens as shown in Fig. 3.6. Figures 3.6(a) and (b), are obtained respectively with a third and fourth order shape compensation lens computed on the centered lens of Fig. 3.4(a). The profiles defined by the arrows in Fig. 3.6(a,b) and plotted in Fig. 3.6(c) show that a fourth order shape compensation lens is necessary to compensate for the "ring effect". Once obtained, the flattened representation of the lens can be used to evaluate the surface roughness, and may also be used to observe fine defects, such as scratches, that would not be apparent on the standard topographic mode as a result of their small size with respect to the global lens shape. However the shape compensation is not yet perfect as shown in particular near the edges of the micro-lens in Fig. 3.6(b). This defect could result from a form defect of the lens or from an inadequate mathematical model to compensate for the shape of a micro-lens. However, the properly flattened part of the lens is sufficient to provide reliable measurement over its working surface. A characterization of micro-lenses with this method is presented in Ref. [Cha06a].

Figure 3.5(c) present the flattened representation of the metallic sphere vertex, obtained by application of a third order shape compensation lens, with profiles positioned on the center of the field of view. Figure 3.5(c) illustrates an interesting feature of the method. As can be seen, such a flattened representation of the specimen surface provides a straightforward access to the surface state, independently from the specimen shape, and reveals fine surface textures or topographical defects. For instance, parame-

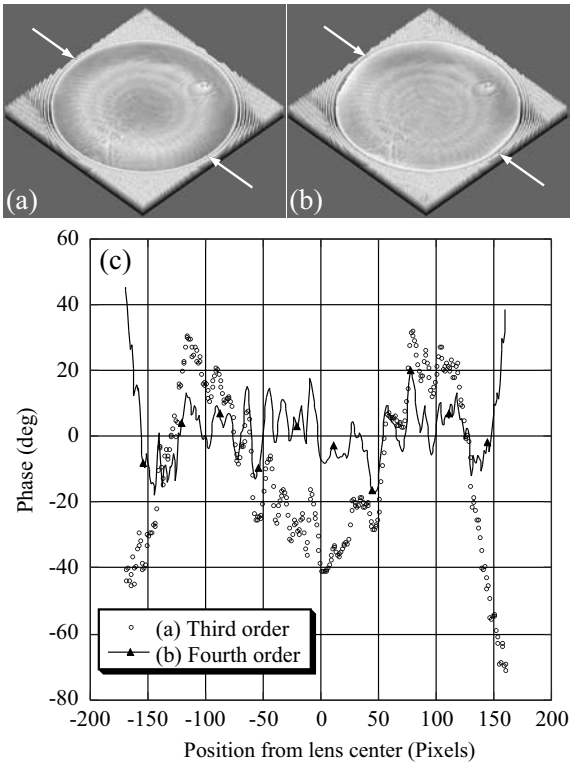


*Figure 3.6: Perspective views computed by compensating for the curvature induced by the lens with (a) a third order shape compensation mask and (b) a fourth order one. (c) Phase profiles defined along the directions of the white arrows of (a) and (b).*

ters such as the means roughness, in this case Ra=25.0 nm, can be directly evaluated as for a flat specimen.

### 3.4.2 Aberration and Topography of Micro-optics

The goal of this section is to show that the Zernike formulation used for shape compensation gives a direct evaluation of aberration of micro-optics as micro-lens for example. Figure 3.7(a) shows that the "flattening" is comparable with previous results (Fig. 3.6) with the adjustment of Zernike coefficients up to $Z_9$. The adjustment of the next Zernike coefficient $Z_{10}$ gives the Figure 3.7(b). The "flattening" is rather better and reveals that this micro-lens has spherical aberrations (see Table A.3). Finally, Figure 3.7(c) shows that the increase of order up to $Z_{20}$ does not allow a better aberration compensation. Figure 3.8 summarizes the repartition of the aberrations of the micro-lens. It shows an important astigmatism ($Z_4$ and $Z_5$) (more in direction $y$ than $x$), a coma amplitude ($Z_6$ and $Z_7$) equivalent in the two directions and a trefoil ($Z_8$ and $Z_9$) negligible in direction $y$ and finally an important primary spherical aberration ($Z_{10}$).

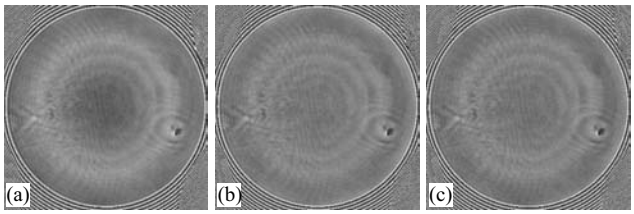


*Figure 3.7: Micro-lens shape compensation with Zernike formulation with (a) 10 parameters, (b) 11 parameters and (c) 21 parameters.*

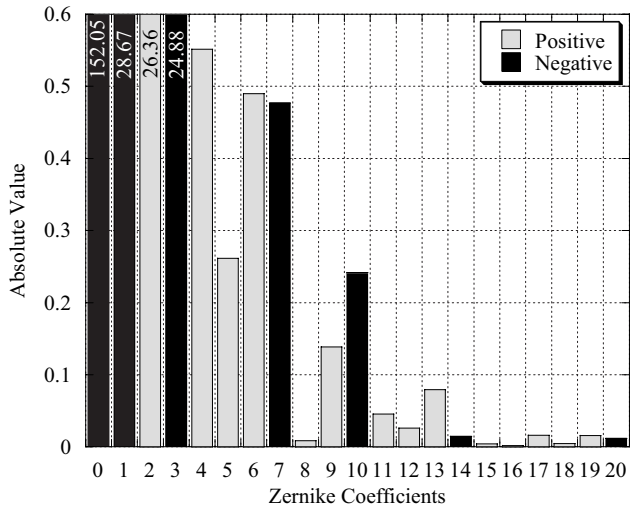


*Figure 3.8: Repartition of Zernike coefficients for an adjustment of 21 Coefficients. The absolute coefficients values are plotted. Black and grey patterns correspond respectively to negative and positive value.*

## 3.5 Conclusion

We presented in this chapter the fitting procedures allowing phase aberrations compensation in the reconstruction plane. Furthermore, we demonstrated that quantitative aberrations parameters could be measured in terms of Zernike polynomials parameters. An example of application was presented with the computation of the Zernike parameters for a micro-lens. Another example, presented in the Ref. [Cha06b], shows that the amplitude point spread function of high NA microscope objectives can be evaluated by DHM and the use of the Zernike 2D fitting method.

We considered in this chapter the aberrations effects on the phase image principally. But the aberrations introduce modification on the amplitudes images too as image distortion or astigmatism. In Chapter 4, we demonstrate that the use of a NPL placed in the hologram plane instead of reconstruction plane achieves a complete aberration compensation in terms of phase and amplitude.

# Chapter 4

# Numerical Parametric Lens in Hologram Plane

## 4.1 Introduction

It has already been proved that the wave front curvature introduced by MO and lenses can be successively removed in DHM [Cuc99b, Ped01b], as well as spherical aberration [Sta00], chromatic aberration [dN05a], astigmatism [dN02, Gri01], anamorphism [dN01, dN05b], or longitudinal image shifting introduced by a beam splitter cube [dN03]. Furthermore, the previous chapter demonstrates that automatic procedures allow the adjustment of parameters associated to a standard polynomial model of aberrations and achieve a complete compensation for phase aberrations in the reconstruction plane without prior knowledge of physical parameters of the setup like wave vector components, focal lengths and position of the optical components [Col06].

On the other hand, the two reconstruction formulations SFTF and CF have each of them several advantages and disadvantages as presented in Section 2.6.3. Among others, there is an important difference about the scaling of the ROI inside the reconstructed wave front plane. Indeed, the scaling in SFTF is dependent of the reconstruction distance, the pixel number of the hologram and the wavelength (Eq. 2.36) [Fer04], whereas it is independent for the CF if there is no chromatic aberration in the setup. This is why different solutions are proposed to control the scaling in SFTF to maintain the size of the ROI for a sequence of digital holograms recorded at different distances and to solve the problem of superimposition in multiwavelength methods for color holography [Kat02, Yam02, Alm04, Jav05a], tomographic holography [Ind99, Kim00, Dak03, Mas05, The05, ML05a, Yu05], or in optical dif-

fraction tomography [Cha06c]. Ferraro *et al.* propose to control the scaling in SFTF by padding the holograms with zeros before the reconstruction [Fer04]. This approach has the disadvantage to increase the computational load because the number of hologram pixels is no longer a power of 2. Indeed, the FFT algorithm is optimized to compute the Fourier transform in time $O(N \log N)$ instead of $O(N^2)$ with $N = 2^n$. Zhang *et al.* propose also another method to keep the original pixel number in SFTF [Zha04b]. A two-stage reconstruction algorithm control the scale of the reconstructed image by placing between the hologram and the reconstruction planes, a numerical lens with a focal and a position defined by the desired scale. The disadvantage of this method is that it needs the computation of two propagations.

Finally, the curvature and the propagation direction of the object wave could slightly change for different wavelengths if the optics are not completely achromatic. Therefore, even in CF, a different scale and position of the ROI can occur.

We propose in this chapter to place a Numerical Parametric Lens (NPL) in the hologram plane. It compensates completely in SFTF or CF, for the aberrations (phase aberrations and image distortions) by the use of automatic procedures explained in the previous chapter. An adjustable shifting and magnification procedure in CF, that maintain the original hologram pixels number and a unique propagation, are also presented.

## 4.2 Digital Reconstruction

As presented in the previous chapter, the phase aberrations could be compensated by introducing a Numerical Parametric Lens (NPL) in the image plane. In this chapter, we introduce a NPL in the hologram plane that allows to compensate for phase aberrations and image distortion. This new NPL $\Gamma^H$ has a shape defined by the phase reconstruction parameters in the hologram plane. Obviously, this NPL can be written in standard or in Zernike model. The reconstructed wavefront is written respectively in

SFTF and CF as:

$$\Psi(m,n) = \Gamma^I(m,n)\cdot A\cdot \exp\left[\frac{i\pi}{\lambda d}\left(m^2\Delta\xi^2+n^2\Delta\eta^2\right)\right]\cdot \text{FFT}\left\{\Gamma^H(k,l)I_H(k,l)\exp\left[\frac{i\pi}{\lambda d}\left(k^2\Delta x^2+l^2\Delta y^2\right)\right]\right\}_{m,n}, \quad (4.1)$$

$$\Psi(m,n) = \Gamma^I(m,n)\cdot A\cdot \text{FFT}^{-1}\left\{\text{FFT}\left[\Gamma^H(k,l)I_H(k,l)\right]\cdot\exp\left[-i\pi\lambda d(\nu_k^2+\nu_l^2)\right]\right\}. \quad (4.2)$$

It should be noticed that the particular case of $\Gamma^H = \boldsymbol{R}_D$ and $\Gamma^I = \Phi$ corresponds to the numerical expression of the Fresnel propagation of Eq. 2.6 [Cuc99a].

Now we represent the parametric numerical lenses in the plane $P = H, I$ as the superposition of three different lenses used to Shift, Magnify and Compensate for the aberrations:

$$\Gamma^P = \Gamma_S^{P,Sh}\cdot\Gamma_S^{P,M}\cdot\Gamma^{P,C}. \quad (4.3)$$

We demonstrate now how to define these NPL's by automatic procedures and present some advantages to correct different orders in the hologram plane instead of image plane. We show that the correction of the tilt with $\Gamma^{H,C}$ allows an automatic shift of the ROI in the center of the reconstruction and that $\Gamma_S^{P,Sh}$ permits a parametric shift. Then we show that the adjustment of the second order of standard polynomial of $\Gamma_S^{P,M}$ permits to do a numerical magnification in CF. Finally, a complete aberration compensation is presented with some examples, in particular the reconstruction of a wavefront from a hologram recorded with a cylindrical lens and with a lens ball as MO. For this purpose, we will introduce the concept of conjugated reference hologram that calibrates the setup to compensate for the aberrations.

## 4.3 Tilt Correction

### 4.3.1 Automatic Centering of the Region of Interest

As shown in Fig. 2.5(d-f) in Section 2.2.2 the central frequency and the ROI of the real or virtual images are not in the center of the reconstructed wavefront. This phenomena is understood by looking at the Fig. 4.1. As presented in the set-ups (Figs. 2.1 and 2.2), the object and reference waves

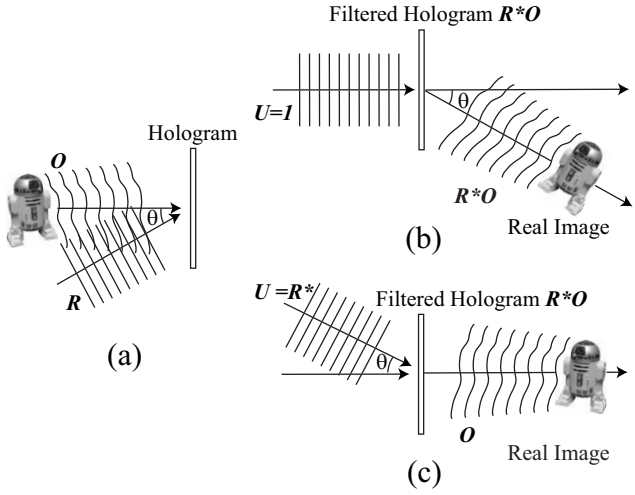


*Figure 4.1: Principle of digital reconstruction process to center the ROI. (a) Hologram recording; (b) Reconstruction with a digital reference wave* $\boldsymbol{U} = 1$ *(the ROI is not centered);(c) Reconstruction with a digital reference wave* $\boldsymbol{U} = \boldsymbol{R}^*$ *(the ROI is centered).*

propagate collinearly and at an angle $\theta$ from the hologram plane normal vector respectively [Fig. 4.1(a)]. We consider now the reconstruction with a filtered hologram containing only the real image (or the virtual image). Two reconstruction cases can be imagined. The first one [Fig. 4.1(b)] corresponds to the reconstruction process with the digital reference wave outside the Fresnel integral. In this case, the reconstructed wavefront in the hologram plane is $\boldsymbol{R}^*\boldsymbol{O}$ and propagates at an angle $-\theta$. The ROI is therefore not in the center of the reconstructed wavefront.

The second case [Fig. 4.1(c)] corresponds to the optical reconstruction process with the conjugated reference wave $\boldsymbol{R}^*$ as illuminating wave. Digitally it corresponds to compute the Eq. 4.1 or 4.2 with $\Gamma^H = \boldsymbol{R}^*$. In this case, the wavefront in the hologram plane is $\boldsymbol{O}$ that propagates normally to the hologram plane. Therefore, the ROI is centered in the reconstructed wavefront.

The shift of the ROI in the first case is not convenient in CF, as the image is no more centered in the window as shown in Figs. 4.2(e,f). In the case of SFTF, it may not be a problem if the sampling step is small enough to cover the off-axis propagation wavefront [Figs. 4.2(a-b)]. But because this sampling is inversely proportional to the reconstruction distance $d$ (Eq. 2.36), aliasing appears when $d$ is too small (Fig. 4.3). Therefore for any formulation, it is more judicious to suppress the shift or the ROI as presented in Figs. 4.2(c,d,g,h) for CF and in Figs 4.3(d) for SFTF.

The procedure to shift the ROI in the center can be done with two methods. The first one called "spectrum centering" consists in shifting the central frequency of the real (virtual) image in the center of the spectrum

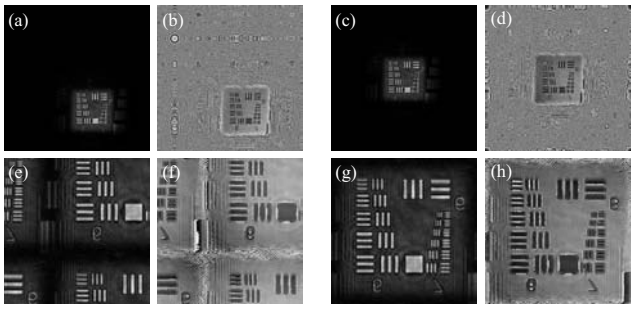


*Figure 4.2: Comparison between SFTF (a-d) and CF (e-h) with (c,d,g,h) or without (a,b,e,f) ROI centering. (a,c,e,g) are amplitude images; and (b,d,f,h) the corresponding phase reconstructions.*

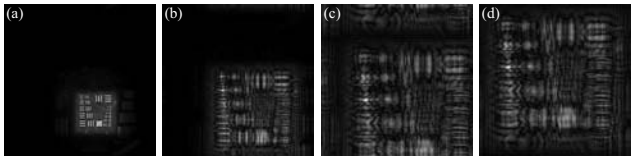


*Figure 4.3: Aliasing appears when the reconstruction distance is too small.(a) $d = 11$ cm; (b) $d = 5$ cm; (c) aliasing at $d = 3.3$ cm. With ROI centering, the reconstruction (d) can be achieved for $d = 3.3$ cm.*

image, in applying an inverse FT, then in propagating it. A simple procedure consists in detecting the position of the amplitude maximum corresponding to the central frequency of the real image [Fig. 4.4(a)]. Then this position is shifted in the center of the spectrum image [Fig. 4.4(b)]. This method has two drawbacks. The first one is that this shifting is one-pixel precise. Secondly, if the fringes on the hologram are curved (see Fig. 2.7), the central frequency is not a point in the spectrum [Fig. 4.4(c)] and it is more difficult to "center" the real image frequencies.

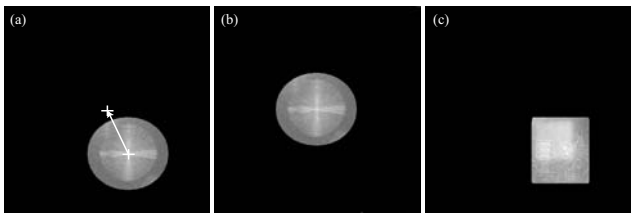


*Figure 4.4: Procedure of spectrum centering. (a)initial filtered spectrum; (b)spectrum centered. The arrow represents the shift between the amplitude maximum of the frequencies associated to the virtual image and the center of the entire spectrum.(c) is the spectrum of the hologram of Fig. 2.7, the fringe curvature induces a non punctual central frequency in the spectrum.*

We propose to compute automatically the tilt parameters $P_{10}^{H,C}$ and $P_{01}^{H,C}$ of $\Gamma^{H,C}$ by performing the fitting procedures explained in the previous chapters on known to be flat profiles or areas selected in the hologram plane. Figure 4.5 presents the hologram plane phase image before (a) and

after (c) the tilt adjustment and their respective image plane amplitude (b,d) reconstructed in SFTF. In this example, the 1D procedure is applied on the selected black profiles of (a). The resulting phase curvature on (c) corresponds to the non-corrected curvature induced by the MO. The ROI is centered in the image plane (d).

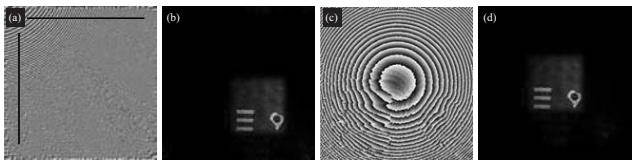


*Figure 4.5: Adjustment of the tilt parameters of the NPL $\Gamma^H$ by applying 1D procedure along black profiles. (a) the initial phase in the hologram plane and (b) the corresponding amplitude reconstruction; (c) tilt corrected phase in the hologram plane and (d) the corresponded centered amplitude reconstruction.*

### 4.3.2 Manual Shifting in Convolution Formulation

It could be interesting to shift the ROI in a specific region, for example to compensate for a specimen shift between two hologram acquisitions. For this purpose, we show how to define the Shifting NPL's $\Gamma^{H;Sh}$ and $\Gamma^{I;Sh}$ in the CF. The principle of the procedure has three steps. First of all, the operator draws two points defining the shift to achieve (arrows in Fig. 4.6). The second step consists in computing the parameters $P_{10}^{H,Sh}$ and $P_{01}^{H,Sh}$ of $\Gamma_S^{H,Sh}$. These parameters can be easily computed by considering Figure 4.7.

Let us define the desired shift in the two directions:

$$\Delta S_j = N_{Sj}\Delta j, \tag{4.4}$$

where $j = x, y$, $N_{Sj}$ is the number of pixels to shift in the $j$-direction. The Shifting NPL is written:

$$\begin{aligned}\Gamma_S^{H,Sh}(\boldsymbol{x}) &= \exp\left[i\frac{2\pi}{\lambda}\hat{\boldsymbol{S}}\boldsymbol{x}\right] \\ &= \exp\left[i\frac{2\pi}{\lambda}(S_x m\Delta x + S_y n\Delta y)\right],\end{aligned} \tag{4.5}$$

where $\hat{\boldsymbol{S}}$ is the unitary shift vector. The components of the vector $\hat{\boldsymbol{S}}$ are:

$$S_j = \sin(\theta_j) = \sin\left[\arctan\left(\frac{\Delta S_j}{d}\right)\right]. \tag{4.6}$$

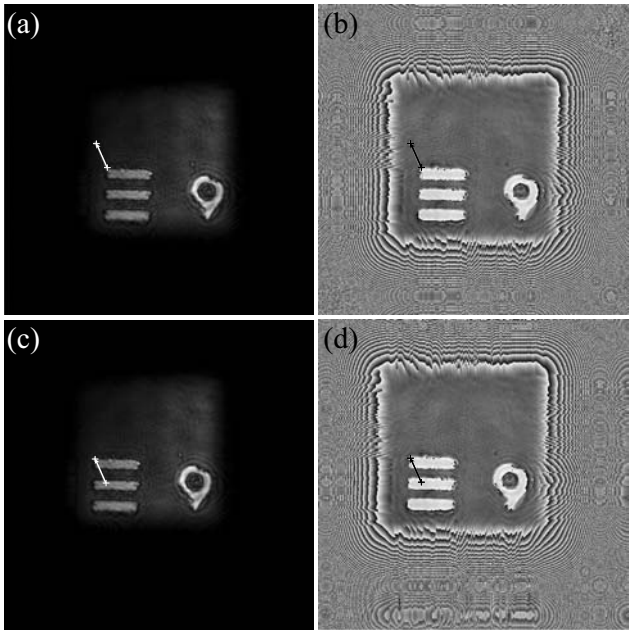


*Figure 4.6: Shifting procedure. (a) and (b) are respectively the amplitude and phase reconstruction after tilt compensation. The arrows define the desired shift of the ROI. (c) and (d) the respective amplitude and phase shifted reconstruction.*

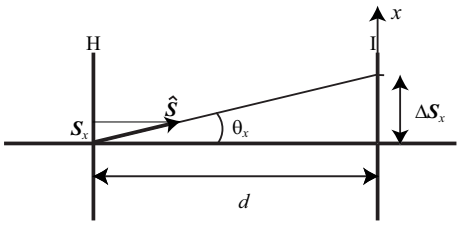


*Figure 4.7: H the hologram plane, I the image plane, $\Delta S_x$ the desired shift in the direction x, d the reconstruction distance and $\theta_x$ the shifting angle.*

The parameters $P_{10}^{H,Sh}$ and $P_{01}^{H,Sh}$ are also:

$$P_{10}^{H,Sh} = -\sin\left[\arctan\left(\frac{\Delta S_x}{d}\right)\right]\Delta x,$$
$$P_{01}^{H,Sh} = -\sin\left[\arctan\left(\frac{\Delta S_y}{d}\right)\right]\Delta y. \tag{4.7}$$

Obviously the shift introduced in the hologram plane produces a tilt in the image plane that should be compensated. We introduce therefore a predicted compensating Shifting NPL in the image plane defined as:

$$\Gamma_S^{I,Sh}(m,n) = \exp\left[-i\frac{2\pi}{\lambda}(P_{10}^{I,Sh}m + P_{01}^{I,Sh}n)\right], \tag{4.8}$$

where $P_{10}^{I,Sh} = -P_{10}^{H,Sh}$ and $P_{01}^{I,Sh} = -P_{01}^{H,Sh}$). Figures 4.6(c,d) present the shifted amplitude and phase reconstructions. It is important to notice that

this shifting method is limited by the desired shift and by the reconstruction distance. Indeed, the angle $\theta$ may satisfy the Eq. 2.3 and gives the inequality:

$$\arctan\left(\frac{\Delta Sj}{d}\right) \leq \theta_{\max} = \arcsin\left(\frac{\lambda}{2\Delta x}\right). \tag{4.9}$$

For example, with a sampling $\Delta x = 6.7$ $\mu$m, a wavelength $\lambda = 633$ nm and a reconstruction distance $d = 1$ cm, the maximum number of pixels to shift is $N_{S\max} = \frac{d}{\Delta x}\tan\left[\arcsin\left(\frac{\lambda}{2\Delta x}\right)\right] = 70.58$.

## 4.4 Numerical Magnification in CF

We propose here to adjust the magnification of ROI by computing the parametric focal distance of the NPL's $\Gamma^{H,M}$ and $\Gamma^{I,M}$. This method keeps constant the pixels number of the hologram and is based on a single propagation. Let us define $H$ the hologram plane where the NPL with focal $f$ is placed, $I$ the original image plane defining by the reconstruction distance $d$ and $I'$ the final image plane defined by the reconstruction distance $d'$. From these definitions, the real object is located at a distance $-d$ from the hologram plane. The magnification $M$ is also defined from the real object and image distances:

$$M = -\frac{d'}{-d} = \frac{d'}{d}. \tag{4.10}$$

The lens equation is:

$$\frac{1}{f} = \frac{1}{-d} + \frac{1}{d'}. \tag{4.11}$$

Let us define now the Magnification NPL described by thin lens transmittance formula [Sal91] or by the Eq. 3.2:

$$\Gamma_S^{H,M}(m,n) = \exp\left[i\frac{2\pi}{\lambda}\frac{1}{2f}(m^2\Delta x^2 + n^2\Delta y^2)\right], \tag{4.12}$$

$$= \exp\left[-i\frac{2\pi}{\lambda}(P_{20}^{H,M}m^2 + P_{02}^{H,M}n^2)\right], \tag{4.13}$$

where $P_{20}^{H,M} = P_{02}^{H,M}$ are the Magnification parameters associated with the focal of the NPL:

$$P_{20}^{H,M} = P_{02}^{H,M} = \frac{\Delta x^2}{2f}. \tag{4.14}$$

Finally, with the Eqs. 4.10, 4.11 and 4.14, the new reconstruction distance and the parameter $P_{02}^{H,M}$ can be computed from $M$ and the initial reconstruction distance $d$:

$$d' = Md, \tag{4.15}$$

$$P_{02}^{H,M} = P_{20}^{H,M} = \left(\frac{1}{M} - 1\right)\frac{\Delta x^2}{2d}. \tag{4.16}$$

Obviously, as for the shifting method, the phase curvature introduced in the hologram plane by the NPL has to be compensated in the new image plane *I'*. The predicted magnification NPL in the image plane *I'* is

$$\Gamma^{I',M}(m,n) = \exp\left[i\frac{2\pi}{\lambda}\frac{1}{2(f-d')}(m^2\Delta x^2 + n^2\Delta y^2)\right], \tag{4.17}$$

$$= \exp\left[-i\frac{2\pi}{\lambda}(P_{20}^{I',M}m^2 + P_{02}^{I',M}n^2)\right], \tag{4.18}$$

that defines the parameters

$$P_{20}^{I',M} = P_{02}^{I',M} = \frac{\Delta x^2(M-1)}{2M^2d}. \tag{4.19}$$

An example of application of this method is presented in Figure 4.8. Two different holograms of the same object are recorded with two different wavelengths $\lambda_1 = 480$ nm [Figs. 4.8(a,b)] and $\lambda_2 = 700$ nm [Figs. 4.8(c-f)]. We notice that the size of the interesting object is different because of the non-achromatic MO used in the setup (difference between the dashed and bold white rectangle). The quotient between the rectangles sized defined a magnification $M = 1.0038$. The magnification procedure gives the scaled reconstruction of Figs. 4.8(e,f).

We can mention here that a different scaling in the two directions can be done by applying two different magnifications in the respective directions.

## 4.5 Complete Aberration Compensation

For the manual shifting and the magnification procedures, only four parameters of the standard polynomial model are used. In this section we demonstrate that the adjustment of higher orders in standard polynomial or Zernike polynomial models allows a complete aberration compensation.

We mention here some works about correction of anamorphism done by De Nicola *et al.* that uses a "chirp function" applied in the hologram plane

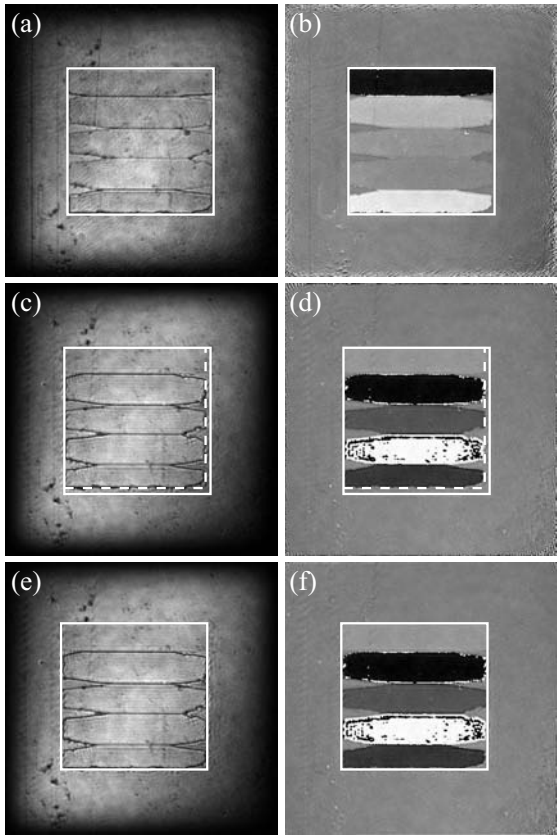


*Figure 4.8: The amplitude and the phase reconstructions are presented respectively on the left and on the right. The reconstructions are done from a hologram recorded with* $\lambda_1 = 480$ *nm (a,b) and* $\lambda_2 = 700$ *nm (c-f). The white rectangle defines the reference size. The white dashed rectangle defines the size of the same object without application of magnification. (e,f) are reconstructed from the same hologram as (c,d) with the application of a magnification* $M = 1.0038$ *defined by the quotient of the rectangle sizes.*

to compensate for the aberration introduced by a reflective grating [dN01]. Furthermore they introduce two reconstruction distances to compensate for astigmatism as Grilli *et al.* in Ref. [Gri01]. Here we propose a general method of aberration compensation that maintains a unique reconstruction distance.

### 4.5.1 Aberration Model

We assume here that the specimen does not introduce aberrations but only a phase delay $\varphi(x, y)$ coming from a difference height of the specimen in reflection configuration or from a refractive index or/and thickness difference in transmission configuration. Let us define here more generally the reference and object waves and a third wave $\boldsymbol{O'}$, corresponding to the object wave without presence of specimen, by adding the phase aberration terms $W_{\boldsymbol{R}}$ and $W_{\boldsymbol{O'}}$ to plane waves (the same reasoning can be done with spherical waves):

$$\boldsymbol{R}(x, y) = |\boldsymbol{R}| \exp\left[i(k_x x + k_y y)\right] \cdot \exp\left[iW_{\boldsymbol{R}}(x, y)\right], \tag{4.20}$$

$$\boldsymbol{O'}(x, y) = |\boldsymbol{O'}(x, y)| \cdot \exp\left[iW_{\boldsymbol{O'}}(x, y)\right], \tag{4.21}$$

$$\boldsymbol{O}(x, y) = |\boldsymbol{O}(x, y)| \exp\left[i\varphi(x, y)\right] \cdot \exp\left[iW_{\boldsymbol{O'}}(x, y)\right]. \tag{4.22}$$

Here we assume that the amplitude $|\boldsymbol{O'}(x, y)|$ and $|\boldsymbol{O}(x, y)|$ are not affected by aberrations in the hologram plane. Furthermore, we assume that the reference wave has no aberration ($W_{\boldsymbol{R}} = 0$). The filtered hologram is

$$I_H^F = \boldsymbol{R}^* \boldsymbol{O} = |\boldsymbol{R}||\boldsymbol{O}| \exp\left[-i(k_x x + k_y y)\right] \exp\left[i(\varphi + W_{\boldsymbol{O'}} - W_{\boldsymbol{R}})\right]. \tag{4.23}$$

Two different methods can be applied to suppress the aberration term $W = W_{\boldsymbol{O'}} - W_{\boldsymbol{R}}$. The first one consists simply in applying the 1D or 2D fitting procedures to adjust the standard or Zernike polynomial parameters of $\Gamma^H$ on the known flat areas in the hologram plane. The second one defined the NPL $\Gamma^H$ with a conjugated reference hologram.

### 4.5.2 Fitting Procedures

The fitting procedures are identical to the procedures presented in Chapter 3. The difference consists in adjusting the parameters on the phase of $I_H^F$. We already showed that the tilt adjustment in this plane allows to place the ROI in the center of the reconstruction plane [Fig. 4.9 (a-c)]. By increasing the order, it is possible to "flatten" the phase in the hologram

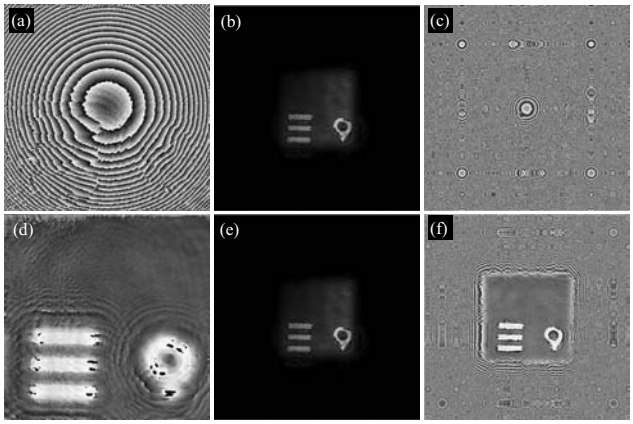


*Figure 4.9: (a) Correction of the tilt in the hologram plane and respective amplitude (b) and phase (c) reconstructions in SFTF at a distance $d = 17.46$ cm without NPL in image plane. (d) High order correction in the hologram plane and respective amplitude (e) and phase (f) reconstruction at a distance $d = 8.78$ cm. The correction in the hologram plane is conserving along the direction of propagation and no more NPL in image plane is necessary.*

plane as presented in Fig. 4.9(d). Because of the compensation of the curvature of the object wave, the NPL works also as a magnification lens: the reconstruction distances with or without the NPL are different and follows the Equations presented in Section 4.4.

In Fig. 4.9 the initial reconstruction distance is $d = 17.46$ cm (b,c), the adjusted term $P_{02}^{H} = 1.24558 \cdot 10^{-10}$ gives a magnification $M = 0.5122$ and a new reconstruction distance $d = 8.78$ cm is used to reconstruct (e,f). Because the reconstruction is done in SFTF, no magnification of the ROI appears. It is important to notice that no NPL was applied in the image plane for the reconstruction of image (c) and (f). We see that the correction in the hologram plane avoids the utilization of a NPL in the image plane for any reconstruction distance. Indeed, the term $\Gamma^{H} \cdot I_{H}^{F}$ is similar to a plane wave that propagates perpendicularly to the hologram plane. The aberrations are also corrected for any reconstruction distance.

### 4.5.3 Reference Conjugated Hologram

In this section we present a calibration procedure that computes the NPL $\Gamma_{RCH}^{H}$, where *RCH* is related to the Reference Conjugated Hologram. The principle of the method was presented already in 1966 by Upatnieks et al. [Upa66] and in 1971 by Ward *et al.* [War71] in the context of classical holography. The principle is as follows.

Let us record a reference hologram without specimen ("empty holo-

gram"). The filtered reference hologram is written:

$$I_H^{R,F} = \boldsymbol{R}^* \boldsymbol{O'} = |\boldsymbol{R}||\boldsymbol{O'}| \exp\left[-i(k_x x + k_y y)\right] \exp\left[i(W_{\boldsymbol{O'}} - W_{\boldsymbol{R}})\right]. \quad (4.24)$$

Let us now define the NPL $\Gamma_{RCH}^H$ with the conjugated phase of this filtered hologram:

$$\begin{aligned}\Gamma_{RCH}^H(m,n) &= \exp\left\{i \arg\left[I_H^{R,F*}\right]\right\} \\ &= \exp\left[i(k_x x + k_y y)\right] \exp\left[-i(W_{\boldsymbol{O'}} - W_{\boldsymbol{R}})\right]. \end{aligned} \quad (4.25)$$

The multiplication of $\Gamma_{RCH}^H$ with a filtered hologram recorded with a specimen (Eq. 4.23) gives:

$$\Gamma_{RCH}^H(m,n) \cdot I_H^F = |\boldsymbol{R}||\boldsymbol{O}| \exp\left[i\varphi(x,y)\right]. \quad (4.26)$$

Equations 4.1 and 4.2 propagate therefore an non-aberrated wavefront.

**Self-reference Conjugated Hologram**

The method of RCH have the disadvantages to need a reference hologram and to assume that the specimen does not produce phase aberration. We propose here to suppress these two last drawbacks by using the specimen hologram itself as the reference one.

Let us assume that the object is quite smooth, for example the hologram of a group of bacillus bacteria [Fig. 4.10(a)]. The first step of the procedure consists in filtering the specimen hologram in its spectrum to keep only the virtual image as presented in Figs. 4.10(b,c). Then, because the information of the details of the specimen have higher frequencies than the aberrations (contained in the central carrier frequency), the self-reference conjugated hologram is strongly filtered to keep only the central carrier frequency [Fig. 4.10(d)]. The reconstruction results are shown in Fig 4.11, where the reconstruction done by the adjustment of $\Gamma^H$ (2D fitting procedure) (a,b) and with the Self-RCH(c,d) are compared. No significative difference are observable.

## 4.6 Results and Discussion

### 4.6.1 Shifting and Magnification in Tomographic DHM

We present here an application of the shifting and magnification procedure in the context of sub-micron optical tomography by multiple wavelength

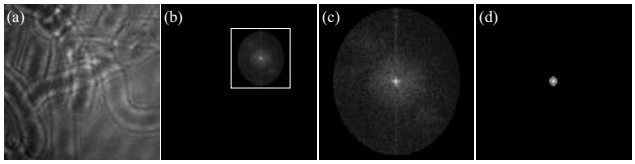


*Figure 4.10: (a) Hologram of bacillus; (b) the entire filtered spectrum; the spectrum inside the white rectangle is report in (c); (d) the filtered spectrum of Self-RCH in the region delimited by the white rectangle.*

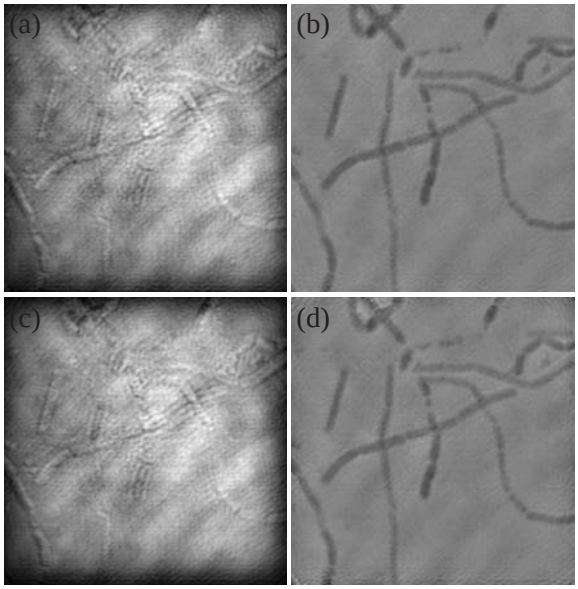


*Figure 4.11: The reconstructions of amplitude (a,c) and phase (b,d) are done by the adjustment of the NPL $\Gamma^H$ in the hologram plane (a,b) and by the self-RCH(c,d).*

DHM. The principle consists in recording several holograms with different wavelengths (typically 20 holograms with wavelengths between 480 nm and 700 nm) with a reflection DHM. The reconstruction of these holograms and their processing allows tomographic imaging [Mononb, Monona]. An important point for the tomographic reconstruction process is that the size of the ROI on each reconstructed image should be identical. Because of the presence of chromatic aberrations and laser pointing changes for each wavelength, the reconstruction distance, the size and the position of the ROI change as shown in Fig. 4.8(a-d). The Figure 4.12 compares the mean amplitude (a,b) and its mapping on the 3D specimen topography (c,d) when the magnification and the shift is not applied to all 20 superimposed images (a,c) or when they are applied (b,d). We can see clearly that (a) is blurred whereas (b) is not. The improvement of the method is also visible for (d) where the noise on the specimen edges is clearly diminished.

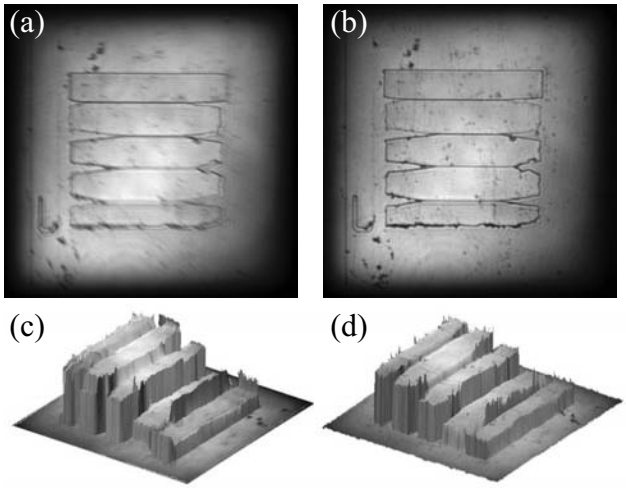


*Figure 4.12: (a,b) Reconstructed mean amplitude from 20 holograms recorded with different wavelengths and (c,d) mapping of it on the 3D topography of the specimen. (b,d) are processed with shift and magnification compensation.*

### 4.6.2 Compensation for Astigmatism Induced by a Cylindrical Lens

Grilly *et al.* present theoretically the potentialities of DHM for astigmatism evaluation and compensation [Gri01]. Furthermore, De Nicola *et al.* present a method with two different reconstruction distances to achieve astigmatism compensation [dN01]. Here we demonstrate experimentally that astigmatism introduced by a cylindrical lens can be compensated by the NPL in the hologram plane. This cylindrical lens is introduced in a reflection setup in the place of the MO [Fig. 2.1(b)]. Figure 4.13 presents the hologram of a USAF test target recorded with this setup. The fringes pattern is unusual and corresponds to the interference between an ellipsoidal wave and a plane wave.

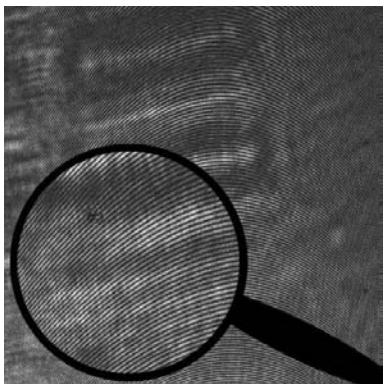

*Figure 4.13: Hologram of USAF test target recorded with a cylindrical lens as MO.*

Figure 4.14 presents amplitude reconstructions in SFTF along the z-

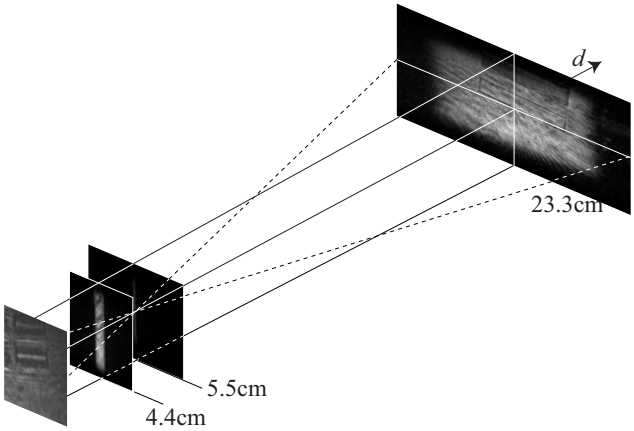


*Figure 4.14: Amplitude reconstruction in SFTF for different reconstruction distances. Due to the astigmatism of the cylindrical lens, there are two different focal points localized at $d = 5.5$ cm and $d = \infty$. The reconstructed image is almost focalized at $d = 23.3$ cm as shown in Fig. 4.15*

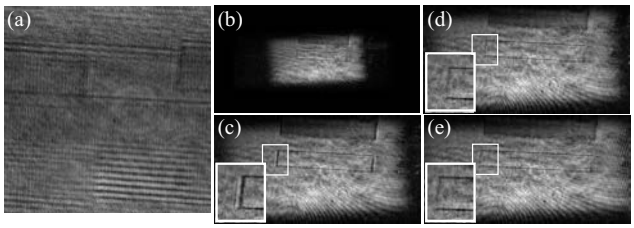


*Figure 4.15: Amplitude reconstruction with different parameters. (a) CF, $M = 1$, $d = 23.3$ cm; (b) SFTF, $d = 23.3$ cm, (c) CF, $M = 0.3$, $d = 6.99$. The astigmatism shown in detail in (c) is compensated by the adjustment of $P_{20}^{H,A} = 0.11 \times 10^{-10}$ (d) or by defining two reconstruction distances $d_1 = 6.99$ cm and $d_2 = 7.92$ cm (e).*

direction for different reconstruction distances. Because of astigmatism of the cylindrical lens, there are two focal points, one for each direction, localized at $d = \infty$ and $d = 5.5$ cm (the amplitude reconstruction shows a vertical line). The image is almost focalized at $d = 23.3$ cm as shown in Fig. 4.15(b) too. This astigmatism can be revealed better by using CF. Because aliasing appears in CF [Fig. 4.15(a)], due to a larger magnification of the cylindrical lens in horizontal direction, a numerical magnification $M = 0.3$ is applied and achieves Fig. 4.15(c). The detail on (c) shows clearly that the vertical edges of the USAF step are not focalized.

Let us define a new NPL written $\Gamma^{H,A}$ that is dedicated to astigmatism compensation and defined by two second order standard polynomial coefficients $P_{02}^{H,A}$ and $P_{20}^{H,A}$. The Figures 4.15(d,e) presents respectively the compensation for the astigmatism by the manual adjustment of $P_{20}^{H,A} = 0.11 \times 10^{-10}$ ($P_{02}^{H,A} = 0$) or by the adjustment of two reconstruction distances $d_1 = 6.99$ cm and $d_2 = 7.92$ cm as explained in Ref. [dN01]. We can see in the details that the two methods correct very well the astigma-

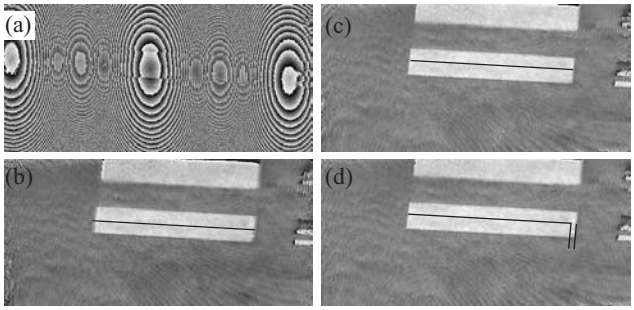


*Figure 4.16: (a) Phase reconstruction with $P_{20}^{H,A} = 0.11 \times 10^{-10}$ without $\Gamma^{I,C}$; the other images are compensated with $\Gamma^{I,C}$: (b) $P_{20}^{H,A} = 0$; (c) $P_{20}^{H,A} = 0.11 \times 10^{-10}$ and (d) two reconstruction distances. The black lines have the same length and reveals a dilatation in the horizontal direction for (d).*

tism, but there is a very small difference between the ROI sizes. Indeed, (e) is bigger in horizontal direction.

Figure 4.16 reveals that the two astigmatism compensations used for the amplitude image are not sufficient to compensate for the others phase aberrations if no NPL is applied in the image plane (a). Therefore, the NPL $\Gamma^{I,C}$ is adjusted in the image plane for the different cases of astigmatism correction: (b) without correction; (c) with $P_{20}^{H,C} = 0.11 \times 10^{-10}$ and (d) with two reconstruction distances. It can be noticed that NPL method conserves the geometry [the step length is equal between (b) and (c)] whereas it is not the case for the two reconstruction distances method (d).

Finally, we compare the two astigmatism compensation methods when the 2D fitting procedure is applied in the hologram plane to adjust $\Gamma_S^{H,C}$. It is also important to notice that as presented for the magnification method, the introduction of $\Gamma^{H,A}$ when $\Gamma^{H,C}$ is adjusted introduced a phase curvature in the image plane that can be compensated with the reciprocal predicted NPL $\Gamma^{I,A}$ in image plane with $P_{20}^{I,A}$ or $P_{02}^{I,A}$ computed from the Eqs. 4.16 and 4.18:

$$P_{20}^{I,A} = \frac{\Delta x^2}{\frac{\Delta x^2}{2P_{20}^{H}} - d}. \tag{4.27}$$

Figure 4.17 presents the phase image in the hologram plane before (a) and after (b) 2D fitting procedure for $\Gamma_S^{H,C}$. The "flattening" in the hologram plane increases the astigmatism as presented in Figs. 4.18(a,b). Indeed, two very different reconstruction distances allow to focalize along horizontal ($d = 13.3$ cm) or vertical direction ($d = -6.9$ cm). The astigmatism is therefore compensated by the two reconstructions distances method [Fig. 4.18(c)] or by the adjustment of $\Gamma^{H,A}$ for the two cases of reconstruction distances: (d) corresponds to ($d = -7.1$ cm, $P_{02}^{H,A} = -4.7 \times 10^{-10}$)

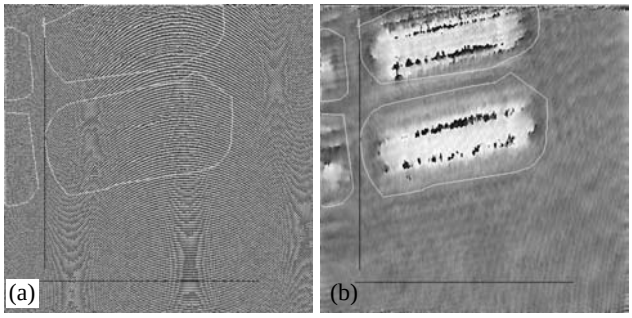


*Figure 4.17: Phase image in hologram plane. Phase image in hologram plane. (a) without* $\Gamma_S^{H,C}$ *adjustment, (b) after adjustment of standard polynomial order* $o = 3$*. The black lines defines the profiles used to define the initial 2D fitting parameters and the white curves delimit the areas excluded from the known to be flat areas.*

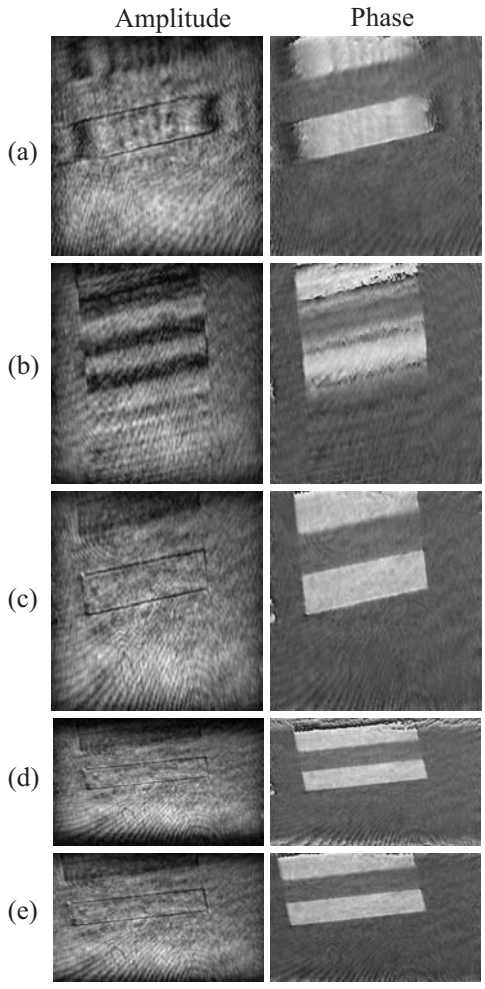


*Figure 4.18: Amplitude and phase reconstructions after* $\Gamma_S^{H,C}$ *adjustment. (a)* $d = 13.3$ *cm; (b)* $d = -6.9$ *cm; (c)* $d_1 = 13.3$ *cm and* $d_2 = -6.9$ *cm; (d)* $M = 0.56$ *(*$d = -7.1$ *cm) and* $P_{02}^H = -4.7 \times 10^{-10}$*; (e)* $M = 0.56$ *(*$d = 7.95$ *cm) and* $P_{20}^H = 4.7 \times 10^{-10}$*.*

and (e) to ($d = 7.95$ cm, $P_{20}^{H,A} = 4.7 \times 10^{-10}$). In short, we show that the two astigmatism compensation methods are not equivalent in terms of the

geometry conservation. Indeed, the two reconstruction distances method deforms the reconstructed images, whereas it is not the case with our method. Furthermore, our method associated with the aberration compensation in hologram plane achieves the astigmatism compensation for amplitude and phase image for any reconstruction distances. These results shows that a cylindrical lens can be used advantageously instead of MO, for example to study specimens with different characteristic length and width like optical fibers or waveguide among others.

### 4.6.3 Lens Ball as MO

To present the different techniques of aberration compensation, we introduce a lens ball (Edmund lens ball SF8 of 2mm diameter $n = 1.689$) as MO to produce very strong aberrations. An index liquid ($n = 1.6$) is used as immersion liquid. The specimen is a USAF test target. Figure 4.19 presents the holograms with (a) and without the specimen (b) and the respective filtered spectrum (c-d). Figure 4.20 presents the comparison between different methods of aberration compensation. In the column (a), only the tilt is compensated in the hologram plane. It is evident that aberrations introduced by the lens ball deformed the USAF test target. Furthermore, the NPL applied in the image plane does not "flatten" correctly the phase image. In the column (b), a 7 order standard polynomial 2D fitting is applied in hologram and image planes. The correction of distortion is good, but the phase aberrations cannot be totally compensated. Finally, the filtered RCH computed from Fig. 4.19(b,d) allows to reconstruct the column (c), where the aberrations are almost completely compensated.

The residual distortion comes from two facts. First, the assumption of a non-aberrated reference wavefront ($W_{\boldsymbol{R}} = 0$) is not achieved. Indeed, if the aberration term $W_{\boldsymbol{R}}$ is different of zero, the RCH method does not compensate exactly for the phase aberration $W_{\boldsymbol{O'}}$. For example in the extreme case where $W_{\boldsymbol{R}} = W_{\boldsymbol{O'}}$, $\Gamma^{H}_{RCH} = \exp\left[i(k_x x + k_y y)\right]$, and the method compensates only for the tilt due to the off-axis geometry. Usually, the phase aberrations in the reference wave are much smaller than for the object wave and can be therefore neglected. Indeed, less optics are used in the reference arm, in particular there is no MO.

Secondly, the model takes in account the phase aberrations in the hologram plane, but the description and the correction of the aberrations should be done in the pupil plane of the system. If the distance between the pupil plane and the hologram plane is not negligible, the automatic phase aberration compensation in the hologram plane is not sufficient to compensate

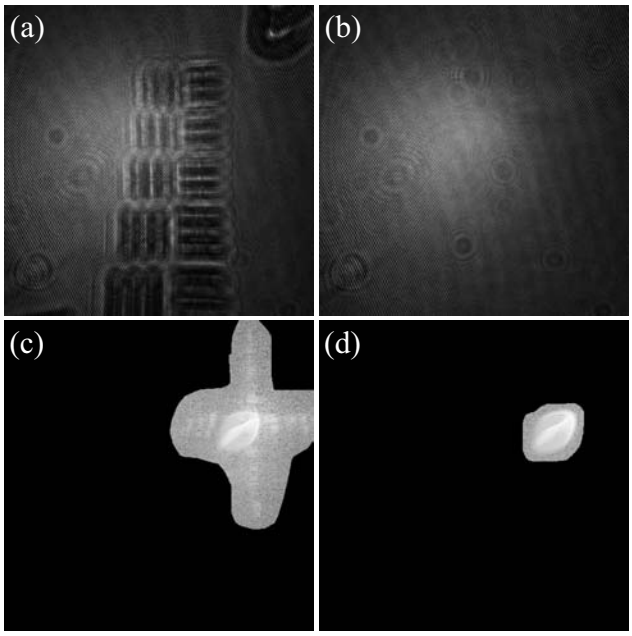


*Figure 4.19: (a,b) are respectively the hologram with and without the specimen; (c,d) are the respective filtered spectrums.*

totally for the distortion. Nevertheless, a compensation for the residual distortion can be done by a manual adjustment of the parameters of the NPL in the hologram plane to minimize the distortion as presented in Fig. 4.21. The manual adjustment of the primary spherical term ($Z_{10} = 9.83 \cdot 10^{-7}$) [Fig. 4.21(c)] allows to compensate totally for the distortion that is not yet totally compensated by the RCH method in (b).

### 4.6.4 Discussion

We present in this chapter numerical methods to compensate for all aberrations. Classically, the aberrations are minimized by use of different controlled optics placed successively in space. Our technique is similar but has the advantage to use a unique NPL located in a single place, the hologram plane. Furthermore, we demonstrated that this numerical lens can be computed to achieve a numerical magnification and shift of the ROI. This last feature gives the opportunity to compensate for the chromatic aberrations, the scaling coming from different reconstruction distances and the specimen shift that can occur between two hologram acquisitions.

In addition, the technique has the advantage to minimize the number of parameters that should be adjusted by the operator. Indeed, automatic fitting procedures and calibration method (RCH) showed that phase aberrations and image distortion can be suppressed, in particular with the compensation for aberration introduced by the use of a cylindrical lens or

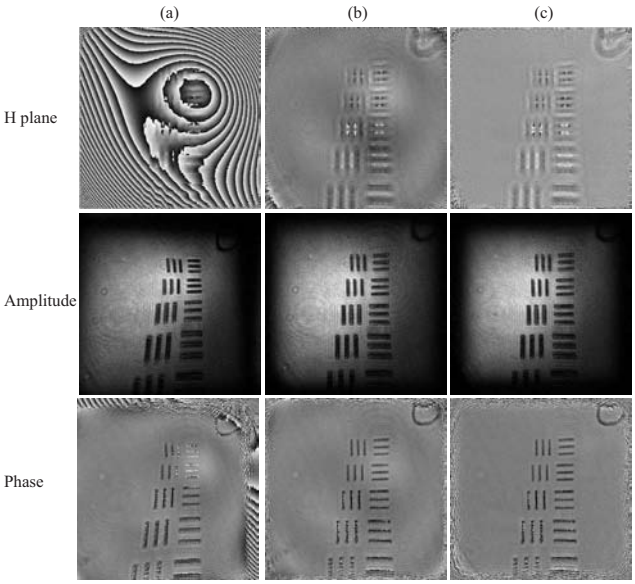


*Figure 4.20: The first row represents the phase in the hologram plane after the multiplication with the NPL, the second and third one the amplitude and phase reconstructions in image plane. (a) correction of tilt in hologram plane and aberration compensated in image plane;(b) compensation with* $\Gamma_S^H$ *and* $\Gamma_S^I$ *with 7 order standard polynomial 2D fitting; (c) compensation with* $\Gamma_{RCH}^H$.

a lens ball as MO. This feature allows to think that low-cost setup could be constructed with low-cost optics presenting aberrations.

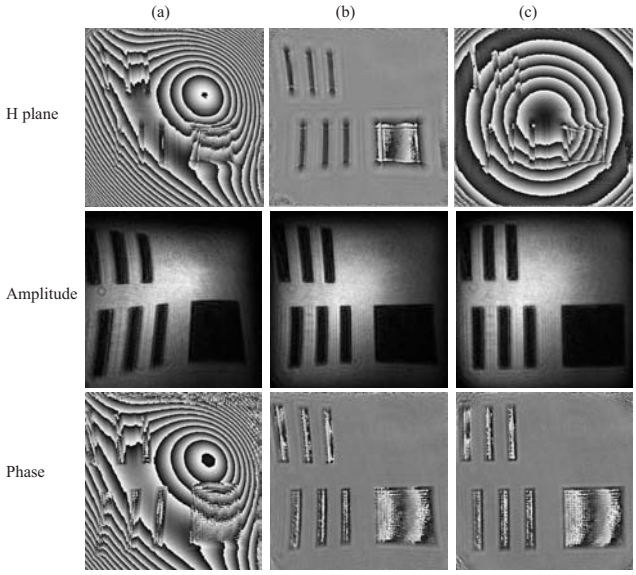


*Figure 4.21: The first row represents the phase in the hologram plane after the multiplication with the NPL, the second and third one the amplitude and phase reconstructions in image plane. (a) tilt compensation in the hologram plane;(b) compensation with* $\Gamma^{H}_{RCH}$*; (c) RCH method, with manual adjustment of* $\Gamma^{H,C}_{Z}$ *(primary spherical* $Z_{10} = 9.83 \cdot 10^{-7}$*) and automatic adjustment of* $\Gamma^{I,C}_{Z}$*.*

# Chapter 5

# Polarization imaging

## 5.1 Method

### 5.1.1 Polariscope Design

The configuration used for hologram recording is presented in Fig. 5.1. The basic architecture is that of a Mach-Zehnder interferometer with two orthogonally linearly polarized reference waves $\boldsymbol{R_1}$, $\boldsymbol{R_2}$ that interfere with an object wave $\boldsymbol{O}$ in off-axis geometry as presented in Fig. 5.1(b). A He-Ne laser (20 mW, $\lambda = 633$ nm) is used to generate the three interfering waves $\boldsymbol{R_1}$, $\boldsymbol{R_2}$ and $\boldsymbol{O}$.

The incident object plane wave $\boldsymbol{O_{in}}$ illuminates the specimen with a known linear polarization state determined by the orientation of a polarizer [Pol. $\delta^o$] in Fig. 5.1(a). The transmitted light produces a wavefront called object wave $\boldsymbol{O}$. The State Of Polarization (SOP) of the object wave is different from the illuminating wave $\boldsymbol{O_{in}}$ and results from the specimen birefringence properties integrated along the propagation direction. Then the wave $\boldsymbol{O}$ reaches the CCD. To simplify the theoretical analysis of polarization, we define a single propagation vector $\boldsymbol{k_O}$ perpendicular to the CCD plane $x_{\boldsymbol{O}}y_{\boldsymbol{O}}$. The reference waves $\boldsymbol{R_1}$ and $\boldsymbol{R_2}$, respectively polarized horizontally (along $x_{\boldsymbol{R1}}$) and vertically (along $y_{\boldsymbol{R2}}$) by polarizers [Pol. in Fig. 5.1(a)], reach the CCD camera with a small incidence angle $\theta_1$ and $\theta_2$. To avoid any interference between the reference waves, the vectors $x_{\boldsymbol{R1}}$ and $y_{\boldsymbol{R2}}$ should be orthogonal; therefore, the directions of propagation $\boldsymbol{k_{R1}}$ and $\boldsymbol{k_{R2}}$ should be respectively in the planes $y_{\boldsymbol{O}}z_{\boldsymbol{O}}$ and $x_{\boldsymbol{O}}z_{\boldsymbol{O}}$. The intensity (amplitude) of each wave is controlled by the orientation of the half-wave plates ($\lambda/2$) in Fig. 5.1. To achieve precise phase measurements, a particular attention is paid to select optical elements minimizing wave fronts distortions. The wave plates ($\lambda/2$ and $\lambda/4$), made in Crystal Quartz, have

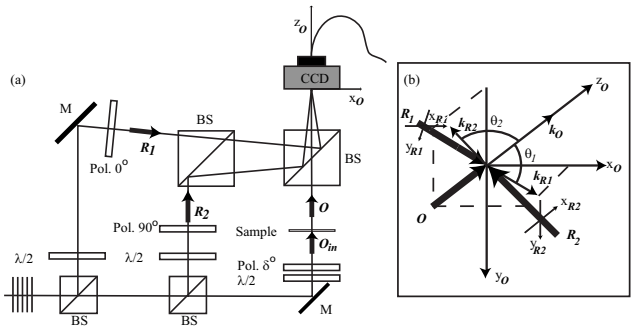


*Figure 5.1: (a) Experimental setup.* $\boldsymbol{O_{in}}$*, incident object wave;* $\boldsymbol{O}$*, object wave;* $\boldsymbol{R}_1$ *and* $\boldsymbol{R}_2$*, polarized reference waves; Pol.* $\delta^o$*, polarizer oriented at* $\delta^o$*;* $\lambda/2$*, half wave plate;* $\lambda/4$*, quarter wave plate; M, mirror; BS, beam splitter. (b) detail showing the off-axis geometry at the incidence on the CCD. The* $0xy$ *plane is parallel to the CCD camera.*

a wavefront distortion of $\lambda/10$ and the polarizers (Glan Laser Polarizers made in calcite with an extinction ratio of 200000:1) a wavefront distortion less than $\lambda/4$.

Using the Jones formalism presented in Section 1.3.1, the different waves are written:

$$\begin{aligned}\boldsymbol{O} &= \begin{pmatrix} |O_1|\exp[i\varphi_{\boldsymbol{O}}] \\ |O_2|\exp[i(\varphi_{\boldsymbol{O}}+\Delta\varphi_{\boldsymbol{O}})] \\ 0 \end{pmatrix}\exp[i(\boldsymbol{k_O x}-\varpi t] \\ &= \begin{pmatrix} O_1 \\ O_2 \\ 0 \end{pmatrix}\exp[i(\boldsymbol{k_O x}+\varphi_{\boldsymbol{O}}-\varpi t], \end{aligned} \tag{5.1}$$

$$\boldsymbol{R}_1 = \begin{pmatrix} R_1 \\ 0 \\ 0 \end{pmatrix}\exp[i(\boldsymbol{k_1 x}-\varpi t],\ \boldsymbol{R}_2 = \begin{pmatrix} 0 \\ R_2 \\ 0 \end{pmatrix}\exp[i(\boldsymbol{k_2 x}-\varpi t], \tag{5.2}$$

where $\boldsymbol{x}=(x,y,z)$ is the position vector, $\varphi_{\boldsymbol{O}}=\varphi_{\boldsymbol{O}}(x,y)$ is the specimen optical phase delay seen by a linear horizontal polarized wave and $\Delta\varphi_{\boldsymbol{O}}$ is the phase difference. The wave vectors are written:

$$\boldsymbol{k_O}=\frac{2\pi}{\lambda}\begin{pmatrix}0\\0\\1\end{pmatrix},\ \boldsymbol{k_1}=\frac{2\pi}{\lambda}\begin{pmatrix}0\\\sin(\theta_1)\\\cos(\theta_1)\end{pmatrix},\ \boldsymbol{k_2}=\frac{2\pi}{\lambda}\begin{pmatrix}-\sin(\theta_2)\\0\\\cos(\theta_2)\end{pmatrix}, \tag{5.3}$$

where $\lambda$ is the wavelength ($\lambda = 633nm$).

At the output of the interferometer the interference between $\boldsymbol{O}$, $\boldsymbol{R_1}$ and $\boldsymbol{R_2}$ creates the hologram intensity distribution:

$$\begin{aligned} I_H(x,y) &= (\boldsymbol{R_1}+\boldsymbol{R_2}+\boldsymbol{O})\cdot(\boldsymbol{R_1}+\boldsymbol{R_2}+\boldsymbol{O})^* \\ &= |\boldsymbol{R_1}|^2+|\boldsymbol{R_2}|^2+|\boldsymbol{O}|^2+\boldsymbol{R_1 O}^*+\boldsymbol{R_2 O}^*+\boldsymbol{R_1^* O}+\boldsymbol{R_2^* O}. \end{aligned} \tag{5.4}$$

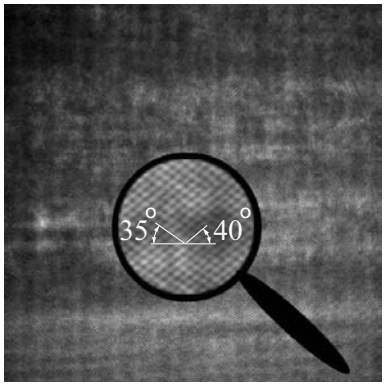


*Figure 5.2: Hologram of three different oriented layers of transparencies. Two fringe patterns can be observed one for each reference wave. Their orientation is determined by off-axis geometry presented in Fig. 5.1(b).*

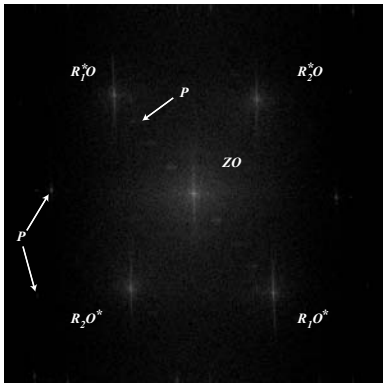


*Figure 5.3: Two-dimensional Fourier spectrum of the hologram presented in Fig. 5.2. ZO is the frequencies associated with the zero order of diffraction, and P indicates the contributions produced by parasitic interferences.* $\boldsymbol{R_1^* O}$ *and* $\boldsymbol{R_1 O^*}$ *are the frequencies associated with the horizontal polarization component corresponding, respectively, to the virtual and real images;* $\boldsymbol{R_2^* O}$ *and* $\boldsymbol{R_2 O^*}$ *are the frequencies associated with the vertical polarization component.*

The first three terms of Eq. 5.4 form the zero-order of diffraction; the fourth and fifth terms produce two real images corresponding respectively to the horizontal and vertical Jones vector components. The last two terms produce the virtual images.

A digital hologram is recorded according to the Eq. 2.1 by a black-and-white CCD camera and transmitted to the computer. An example of hologram recorded with this configuration is presented in Fig. 5.2. The specimen is formed by different oriented layers of transparencies. Two fringe patterns with fixed orientations ($-35^o$ and $40^o$ with respect to the horizontal) can be observed. The carrier frequency of these two fringe patterns is fixed by $\theta_1$ and $\theta_2$.

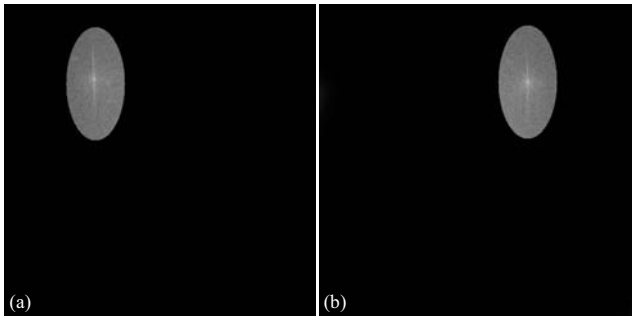


*Figure 5.4: Selection of the virtual image (a) for the horizontal polarization component, (b) for the vertical polarization component.*

### 5.1.2 Spatial Filtering

By computing the Fourier Transform (FT) of the hologram, we obtain its spectrum. Figure 5.3 presents the amplitude of this spectrum where the frequencies of the zero order of diffraction, of the real and virtual images and of parasitic interferences can be seen. By applying two different spatial filtering on this spectrum, the spatial frequencies components corresponding to each virtual image are selected separately as explained in Section 2.2.2 and in Ref. [Cuc00d] (Fig. 5.4). Computing the inverse FT of these filtered spectrums results in two filtered complex holograms, and the standard reconstruction algorithms (SFTF or CF) can be applied (on each filtered hologram) as explained in previous chapters. These two complex holograms are written ($j = 1, 2$):

$$I_{Hj}(x, y) = \boldsymbol{R_j^* O}. \tag{5.5}$$

### 5.1.3 Reconstruction of Polarization Parameters

The images of the SOP parameters $\varepsilon$ and $\Delta\varphi_{\boldsymbol{O}}$ defined in Section 1.3.1 are reconstructed as follows.

The first step consists in reconstructing the amplitude and the phase from the two filtered holograms (Eq. 5.5) in SFTF (Eq. 4.1) or in CF (Eq. 4.2). For example, in SFTF, the two wavefront are written ($j = 1, 2$):

$$\begin{aligned}\Psi_j(m,n) =& \Gamma_j^I(m,n) \cdot A \cdot \exp\left[\frac{i\pi}{\lambda d}\left(m^2\Delta\xi^2 + n^2\Delta\eta^2\right)\right] \cdot \\ & \mathrm{FFT}\left\{\Gamma_j^H(k,l) I_{Hj}(k,l) \exp\left[\frac{i\pi}{\lambda d}\left(k^2\Delta x^2 + l^2\Delta y^2\right)\right]\right\}_{m,n}. \end{aligned} \tag{5.6}$$

where $\Gamma_j^H$ and $\Gamma_j^I$ are the adjusted NPL's placed respectively in the hologram plane and in the image plane, used to compensate for the tilts and

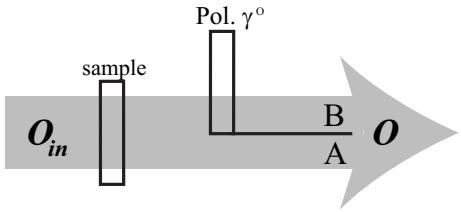


*Figure 5.5: Use of reference area in the object arm.* $\boldsymbol{O_{in}}$ *illuminating wave, Pol.* $\gamma$ *polarizer oriented at angle* $\gamma$*, used as reference area for the phase difference offset determination. B is the reference area where phase difference is 0 and A the area where the measurement of* $\boldsymbol{O}$ *is done.*

the aberrations associated to the filtered hologram $I_{Hj}$. Classically, the reconstruction is similar to a successive illumination with the two reference waves $\boldsymbol{R_1}$ and $\boldsymbol{R_2}$ (in our case two digital reference waves $\boldsymbol{R_{D1}}$ and $\boldsymbol{R_{D2}}$):

$$\Psi_j(m,n) = \boldsymbol{R_{Dj}} I_{Hj} = \boldsymbol{R_{Dj}} \boldsymbol{R_j^*} \boldsymbol{O}. \tag{5.7}$$

Using Eq. 5.2 in Eq. 5.7 and taking the amplitude and the phase contrasts of $\Psi_1$ and $\Psi_2$ yields:

$$|\Psi_j| = |R_j||O_j|, \tag{5.8}$$

$$\arg(\Psi_j) = \arg(O_j) - \arg(R_j) + \varphi_{\boldsymbol{O}}. \tag{5.9}$$

The adjustment of the half-wave plates orientation in the reference arms [$\lambda/2$ in Fig. 5.1(a)] achieves equal amplitudes for reference waves ($|R_1| = |R_2|$). Thus, the phase difference [$\Delta\varphi_{\boldsymbol{O}} = \arg(O_2) - \arg(O_1)$] and $\varepsilon$ [$\varepsilon = \arctan(|O_2|/|O_1|)$] parameters can be expressed from Eqs. 5.8 and 5.9:

$$\tan(\varepsilon) = \frac{|\Psi_2|}{|\Psi_1|} = \frac{|O_2|}{|O_1|}, \tag{5.10}$$

$$\Delta\varphi_{\boldsymbol{O}} = \arg(\Psi_2) - \arg(\Psi_1) + \Delta\varphi_{\boldsymbol{R}}, \tag{5.11}$$

where $\Delta\varphi_{\boldsymbol{R}} = \arg(R_2) - \arg(R_1)$ is cancelled by a calibrated phase difference offset applied to the phase difference image. Experimentally, this term is time-dependent because of vibrations, air flux, but it can be suppressed on the image by a phase difference offset equal to $-\Delta\varphi_{\boldsymbol{R}}$. To adjust this offset, a known polarization state area is used in the image. For example a polarizer, that produces a phase difference of 0 degree, is placed in the object wave as shown in Fig. 5.5. Therefore a measurement of the mean phase difference in this area (B) gives directly $\Delta\varphi_{\boldsymbol{R}}$.

The second step to achieve the reconstruction of the SOP parameters consists therefore in superposing the ROI and in computing pixel by pixel the Eq. 5.10 and 5.11. This procedure is achieved automatically by applying the tilt correction in the hologram plane as presented in Section 4.3.

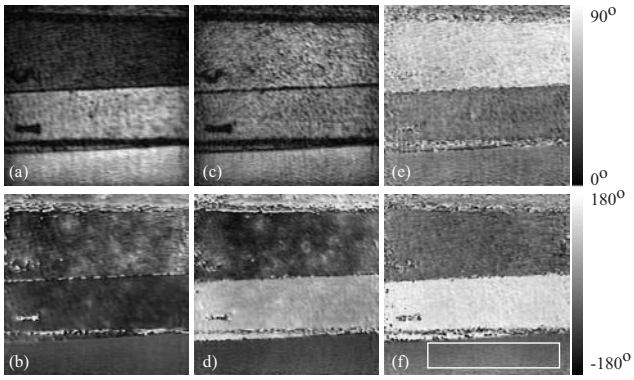


*Figure 5.6: Reconstruction of wave fronts and SOP images. (a) $|O_1|$; (b) $\arg(O_1)$; (c) $|O_2|$; (d) $\arg(O_1)$; (e) $\varepsilon$ and (f) $\Delta\varphi_{\boldsymbol{O}}$. The area defined by the white rectangle is used to calibrate the phase difference offset to compensate for $\Delta\varphi_{\boldsymbol{R}}$.*

Furthermore, if the superposition is not perfect, a manual shifting as presented in Section 4.3.2 can be done.

Figure 5.6 presents the reconstructions obtained from the hologram of Fig. 5.2 after the compensation for the aberrations and the tilt in the hologram plane in CF. (a,b) and (c,d) are respectively the amplitude and phase components of $O_1$ and $O_2$. The SOP images presented in (e,f) show clearly that the specimen has polarization properties. The phase difference image (f) informs about birefringence properties (see. Section 1.3.2), whereas the parameter $\varepsilon$ (e) informs about dichroism properties (see Section 1.3.2). The phase difference offset $\Delta\varphi_{\boldsymbol{R}}$ is calibrated inside the area delimited by the white rectangle.

## 5.2 Precision Limit

To evaluate the reconstruction algorithm, we simulate some series of holograms resulting from the interference between the reference waves and the object wave having a known SOP. Then, we compare the theoretical values with those calculated by the hologram reconstruction. The input object wave $\boldsymbol{O_{in}}$ is chosen (wave in the object arm before transmission through the specimen) as a linear polarization oriented at 45 degrees (Fig. 5.1 polarizer angle $\delta = 45^o$). By suppressing the component in z-direction that is always equal to zero, the Jones vector of this wave is

$$\boldsymbol{J_{O_{in}}} = \begin{pmatrix} 1 \\ 1 \\ 0 \end{pmatrix} = \begin{pmatrix} 1 \\ 1 \end{pmatrix}. \tag{5.12}$$

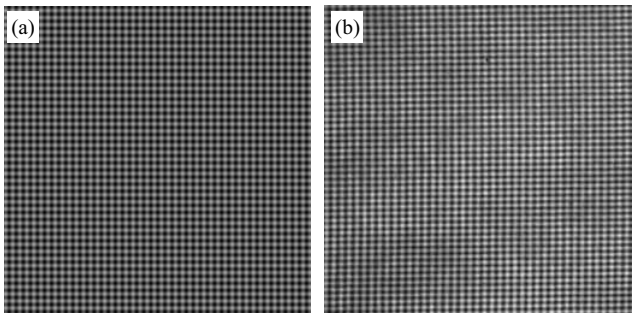


*Figure 5.7: Comparison between (a) simulated hologram and (b) experimental hologram.*

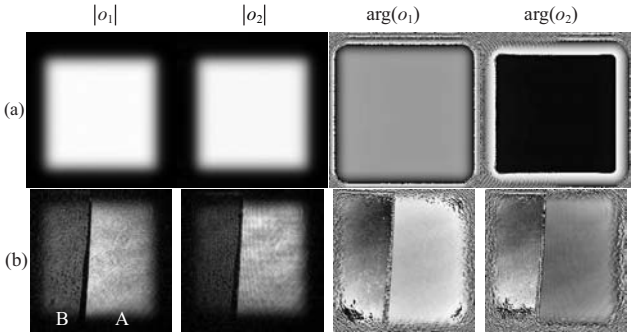


*Figure 5.8: Amplitude and phase contrasts reconstructed for (a) simulated hologram and (b) experimental hologram. In experimental images, the area B on the left is the polarizer and A the half-wave plate.*

Then, a half-wave plate is used as specimen and different holograms are simulated (or recorded) for different orientations of it. A wave retarder with an orientation $\delta$ is represented by the Jones matrix

$$T(\delta) = R(-\delta) \begin{bmatrix} 1 & 0 \\ 0 & \exp[-i\Lambda] \end{bmatrix} R(\delta). \tag{5.13}$$

where $\Lambda = \pi$ for half-wave retarder. $R$ is the matrix of the coordinates transformation

$$R(\delta) = \begin{bmatrix} \cos(\delta) & \sin(\delta) \\ -\sin(\delta) & \cos(\delta) \end{bmatrix}. \tag{5.14}$$

Therefore, the Jones vector of $\boldsymbol{O}$ becomes

$$\boldsymbol{J_O} = T(\delta)\boldsymbol{J_{O_{in}}}. \tag{5.15}$$

The results compare the theoretical SOP of $\boldsymbol{J_O}$, with the parameters obtained by the reconstruction of the simulated holograms and finally with the parameters obtained by the reconstruction of the experimental holograms.

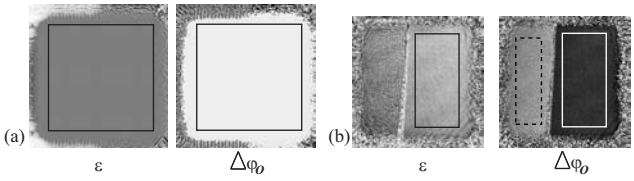


*Figure 5.9: Polarization parameters images for simulated hologram (a) and experimental hologram (b). The calculus of SOP mean values and std's are calculated with pixel values inside the ROI delimited by the solid rectangles. In case of experimental phase difference image, the mean value calculated in the dashed ROI permits to adjust the phase difference offset.*

### 5.2.1 Results and Discussion

For the simulation and experimentation, the same parameters are used. The laser is a He-Ne with a wavelength of 632.8 nm. The angles between each reference wave and the object wave are $\theta_1 = \theta_2 = 0.72$ degrees and the pixel size of the CCD camera used (Hitashi KP-M2 CCIR) is 8.6 $\mu$m. These parameters allow to simulate $N$x$N$ holograms with Eqs. 5.4 and 2.1. The reconstruction algorithm uses usually 512x512 pixels holograms, but for comparison 256x256 pixels holograms are presented in Fig. 5.7.

In Fig. 5.8 the amplitude and the phase contrasts of the reconstructed wave fronts are presented. For the experimental reconstruction, a polarizer is introduced as a reference area (A in Fig. 5.8) as explained previously (Fig. 5.5). The computation pixel per pixel of Eq. 5.10 and 5.11 gives the SOP images of Fig. 5.9.

Simulating or recording holograms for different orientations of a half-wave plate used as specimen ($0^o$ to $180^o$ by $1^o$ step) permits to compare theoretical SOP and reconstructed SOP mean value calculated in ROI's (defined by solid rectangles in Fig. 5.9). To determine the phase difference with the experimental holograms, the phase difference offset $\Delta\varphi_{\boldsymbol{R}}$ is computed as explained before by using the mean value in the ROI of the reference area (dashed rectangle in Fig. 5.9). The result is presented in Fig. 5.10. An almost perfect superposition of the theoretical and simulated curves is achieved, while the experimental curves are in good agreement. To permit a better comparison, the Fig. 5.11 presents the difference between theoretical and reconstructed SOP values. The precision of SOP parameters for a single pixel is evaluated in Fig. 5.12 by computing the std of SOP parameters in the same ROI's.

The graphs about mean values (Fig. 5.11) show that there is an important difference between errors for the simulated and errors for the experimental setup (0.01 and 1 degree for $\varepsilon$ for respectively simulated and experimental setup, and 0.03 and 5 degrees for phase difference). How-

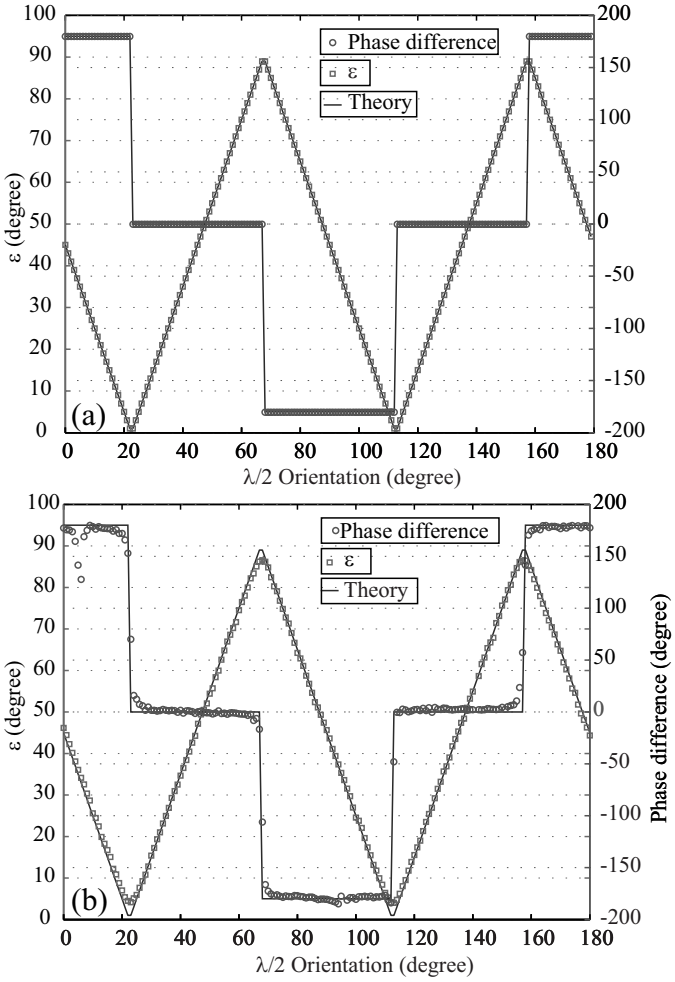


*Figure 5.10: Comparison between theory and (a) simulated reconstructed holograms and (b) experimental reconstructed holograms*

ever a similar behavior can be observed. The experimental results on $\varepsilon$ errors show four peaks [arrows in Fig. 5.11(a)], also observable on simulation results [fit in Fig. 5.11(a))]. These four critical orientations of the half-wave plate correspond to a linear horizontal ($\delta = 22.5^o, 112.5^o$) and vertical ($\delta = 67.5^o, 157.5^o$) polarized object wave. For these orientations, the amplitude corresponding to an orthogonal polarization should be zero. Different contributions appearing in the image account for the observed amplitude offset. The first very low contribution comes from algorithm and will be called "numerical noise". It provides the explanation of the observed offset on simulations. The experimental setup gives a higher offset amplitude component. Indeed the experimental holograms are disturbed by different noise sources. The first source is the "structural noise" coming from a coherent interference between parasitic waves (reflection on optics, diffraction on dust...). The second one comes from the CCD camera which is affected by such as electronic noise, shot noise, dark noise and so on.

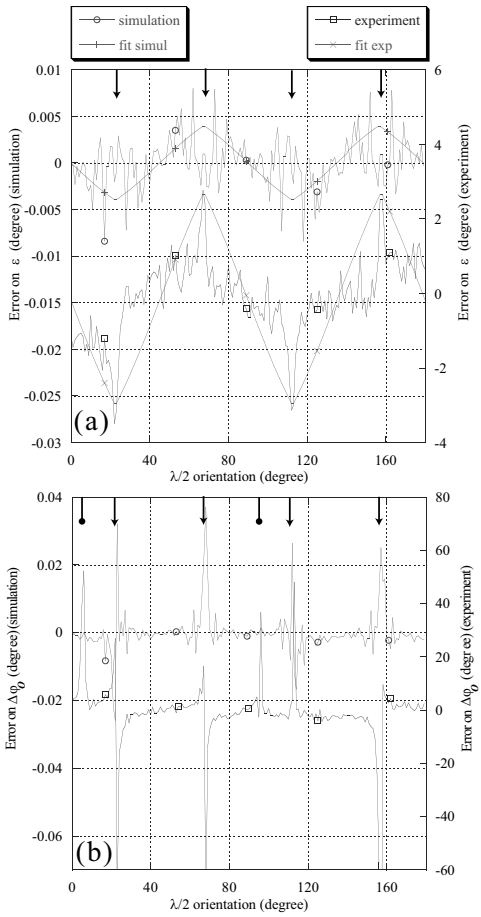


*Figure 5.11: Difference between theoretical values and SOP reconstructed values. (a) $\varepsilon$ and (b) phase difference. The arrows indicate the critical angles for which the object wave is polarized vertically or horizontally. The arrows with the point indicate the critical angles for which no light is passing through the reference polarizer. The lines on part (a) of the figure fits errors on $\varepsilon$ after adjustment of the background amplitude for $|O_1|$ and $|O_2|$ for the experimental and simulated holograms cases.*

Finally misalignments and small errors on the optics orientations are error sources. A simple model allows to fit the simulated and experimental values. Assuming an amplitude offset equal to a percentage $\alpha$ and $\beta$ of respectively maximum $|O_1|$ and $|O_2|$ amplitude, $\varepsilon$ error is written:

$$\varepsilon_t - \varepsilon_c = \varepsilon_t - \arctan\left(\frac{|O_2| + \alpha \max(|O_2|)|}{|O_1| + \beta \max(|O_1|)|}\right), \tag{5.16}$$

where $\varepsilon_t$ and $\varepsilon_c$ are respectively the theoretical and calculated $\varepsilon$, and $\max(|O_j|)$, the maximum of amplitude for the object wave polarized horizontally ($j = 1$) or vertically ($j = 2$). Fits in Fig. 5.11(a) are plotted with $\alpha = \beta = 0.007\%$ for the simulation and $\alpha = 5\%$, $\beta = 5.5\%$ for the experimentation.

Rapid variations in experimental values can be explained by time instabilities mostly due to vibrations, air turbulence, that produce intensity variations for all interferences (interference between the object and reference waves and "structural noise"). For the simulation, truncated values in the algorithm can explain the rapid variation phenomena. A solution to avoid error due to the background is to calibrate the method by suppressing the background numerically before calculating $\varepsilon$. On the contrary it is difficult to suppress the errors because of the time instability. The graph of the phase difference errors in Fig. 5.11(b) shows as expected a huge error for the critical orientations [arrows in Fig. 5.11(b)]. Indeed, for these orientations, the fringe pattern corresponding to the orthogonally polarized reference wave disappears. Therefore the algorithm cannot reconstruct the phase image and a random phase image is obtained. The substraction between the two phase contrasts contains also a random phase and an undefined phase difference is also reconstructed. Moreover, a similar phenomenon [arrows with point in Fig. 5.11(b)] appears when the polarizer used as a reference area stops the input object wave. In this case, the reference area is undefined and therefore the phase difference offset cannot be calibrated.

The std on the images provides an evaluation of the quality of the imaging method. Figure 5.12 shows that the limit of the algorithm is a std of about 0.12 degree for $\varepsilon$ and 0.3 degree for the phase difference (for an orientation different that the critical angles defined in the last paragraph). Experimentally, the limits are higher because of the same reasons explained before. For $\varepsilon$ measurement, Fig. 5.12(a) shows that experimentally the std is minimal for the critical angles. It can be understood with a simple error

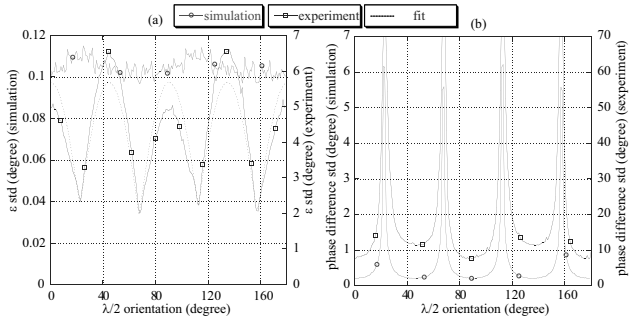


*Figure 5.12: Std of the polarization parameters for the measurement in object area. (a)$\varepsilon$ and (b) phase difference.*

calculation:

$$\begin{aligned}\Delta\varepsilon &= \frac{\partial\varepsilon}{\partial|O_1|}\Delta|O_1| + \frac{\partial\varepsilon}{\partial|O_2|}\Delta|O_2| \\ &= \frac{|O_2|\Delta|O_1|}{|O_1|^2+|O_2|^2} + \frac{|O_1|\Delta|O_2|}{|O_1|^2+|O_2|^2}.\end{aligned} \tag{5.17}$$

Figure 5.13 shows a linear relation ($j = 1, 2$):

$$\Delta|O_j| = \alpha_{j1} + \alpha_{j2}|O_j|. \tag{5.18}$$

Using Eq. 5.15 with $\Lambda = \pi$, a simple calculus gives:

$$|O_1| = |\sin(2\delta) + \cos(2\delta)|, \tag{5.19}$$

$$|O_2| = |\sin(2\delta) - \cos(2\delta)|. \tag{5.20}$$

Assuming $|O_1|^2 + |O_2|^2 = 1$ and introducing Eq. 5.18 and 5.20 in Eq. 5.17 gives:

$$\begin{aligned}\Delta\varepsilon =&(\alpha_{12}+\alpha_{22})|\cos(4\delta)| + \alpha_{21}|\sin(2\delta)+\cos(2\delta)| \\ &+ \alpha_{11}|\sin(2\delta)-\cos(2\delta)|.\end{aligned} \tag{5.21}$$

The $\varepsilon$ std is therefore minimal when $\cos(4\delta) = 0$ and therefore when $4\delta = 90 + n\cdot 180$ ($n$ an integer). These orientations correspond to an object wave polarization orthogonal to one of the reference waves. The maximum std occurs when $4\delta = n \cdot 180$. An experimental data fit, plotted in dashed line in Fig. 5.12(a) with $\alpha_{12} + \alpha_{22} = 2.79$, $\alpha_{21} = 1.53$ and $\alpha_{11} = 1.35$, is well adapted for the critical angles. But the model does not explain the difference between the maxima that is understood by a different quality of the reconstructed amplitude contrasts.

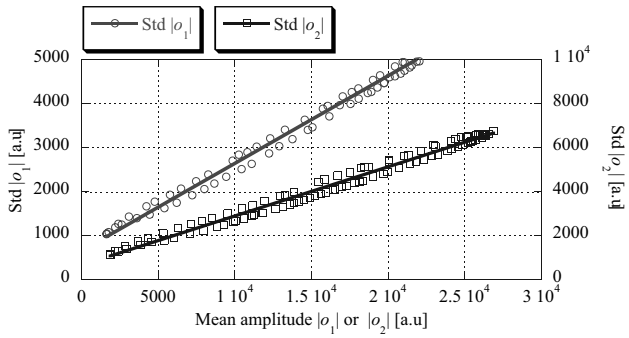


*Figure 5.13: Std for the amplitude contrasts versus mean amplitudes.*

The phase difference std presents peaks for the critical angles for which random phase contrast is reconstructed. Between the critical angles, imperfect optics, dust and all noises expressed before give contributions to the phase difference std seen on the experimental reconstruction in Fig. 5.8. A quality difference between the two reconstructed phase images explains, as for $\varepsilon$ std, the different minimal values between the different critical orientations.

### 5.2.2 Discussion

The estimation of errors made on calculated holograms demonstrates that the method is able to image and to determine the SOP of an unknown object wave with about 0.01 degree for $\varepsilon$ and 0.03 degree for the phase difference out of the critical angles (when the object wave is polarized linearly horizontally or vertically). Moreover, it allows to measure the std limit introduced by the algorithm on the SOP images: 0.12 degree for $\varepsilon$ and 0.3 degree for the phase difference. Then, the experimental holograms show that the method works well even if the errors are larger. We demonstrated that with only one image acquisition the method calculates the SOP parameters with an error smaller than 1 degree for $\varepsilon$ and smaller than 5 degrees for the phase difference out of the critical angles. Setup optimization, better optics and suppression of parasitic interferences by use of a low coherence source for example, should increase the accuracy.

## 5.3 Experimental Results

To evaluate the measurement of the amplitudes $|O_1|$ and $|O_2|$, an object composed of two polarizers presented in Fig. 5.14 is used. The first polarizer $P1$ has a variable orientation and the second polarizer $P2$ has a fixed orientation ($-45^o$). This object is illuminated by a circularly polarized wave

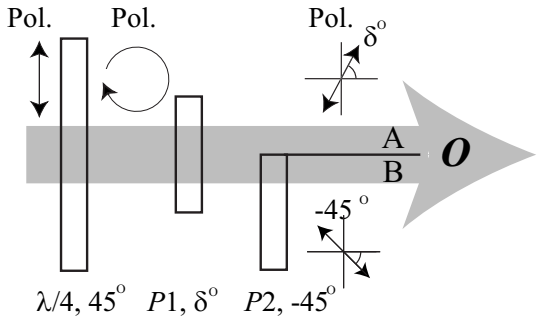


*Figure 5.14: (a) Setup in the object arm for the results presented in Figs. 5.15 and 5.16. P1 is a linear polarizer with a variable orientation $\delta$ and P2 a linear polarizer oriented at $-45^o$. $\lambda/4$ a quarter wave retarder oriented at $45^o$. In part B of the beam, which crosses P2 (oriented at $45^o$), similar intensities are expected for both components of the polarization state for any P1 orientation.*

produced by a quarter wave plate $\lambda/4$ oriented at $45^o$ with respect to the linearly polarized wave from the laser source. The entire illumination wave passes through $P1$ but only a part (part $B$ in Figs. 5.14 and 5.15) passes through $P2$. Reconstructed amplitude-contrast images obtained for three different values of $\delta$ ($0^o$, $45^o$ and $90^o$) are shown in Fig. 5.15. Only the virtual images are presented. Images in the left-hand column correspond to the horizontal polarization state and images in the right-hand column to the vertical polarization state. Figures 5.15(a-b) present the results obtained for $\delta = 0^o$, (c-d) for $\delta = 45^o$ and (e-f) for $\delta = 90^o$. In part $B$ of the images, the amplitudes are identical for both orthogonal states for any value because $P2$ is oriented at $-45^o$. In part $A$, the amplitude of the parallel component is maximal for $\delta = 0^o$ and minimal for $\delta = 90^o$. For the perpendicular component we observe the opposite behavior. As expected similar amplitudes can be observed for both polarization states when $P1$ is oriented at $\delta = 45^o$. In this case, the intensities in part $B$ are near zero because the relative orientation of $P1$ and $P2$ is $90^o$.

The results of Fig. 5.15 demonstrate qualitatively that the method behaves as expected for a well-known particular situation. If we now consider intermediate $\delta$ values, the measured amplitude in part $A$ is theoretically given by the product between the Jones matrix of a linear polarizer and the Jones vector of a right circularly polarized wave:

$$\begin{aligned} \boldsymbol{J_O} &= \frac{1}{\sqrt{2}} \begin{bmatrix} \cos^2(\delta) & \sin(\delta)\cos(\delta) \\ \sin(\delta)\cos(\delta) & \sin^2(\delta) \end{bmatrix} \begin{pmatrix} 1 \\ i \end{pmatrix} \\ &= \frac{1}{\sqrt{2}} \begin{pmatrix} \cos(\delta) \\ \sin(\delta) \end{pmatrix} \exp\left[i\delta\right]. \end{aligned} \tag{5.22}$$

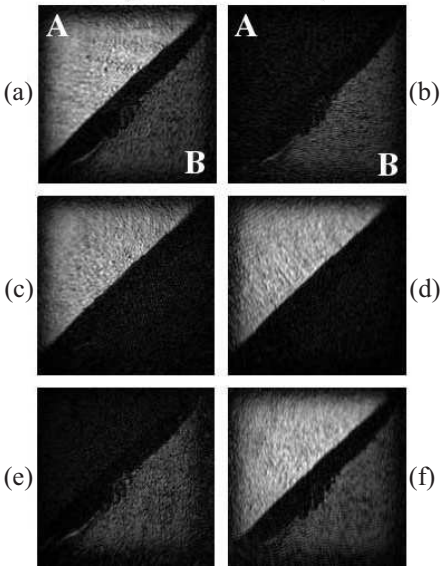


*Figure 5.15: (a), (c) and (e) are the reconstructed virtual images corresponding to the horizontal polarization component and (b), (d) and (f) to the vertical polarization component. 3 orientations $\delta$ of P1 are presented: (a)-(b) $\delta = 0^o$, (c)-(d) $\delta = 45^o$ and (e)-(f) $\delta = 90^o$.*

As $|O_1|$ and $|O_2|$ represent amplitudes that are positive by definition, Eq. 5.22 can be written as follows:

$$\begin{aligned} \boldsymbol{J_O} &= \frac{1}{\sqrt{2}} \begin{pmatrix} |\cos(\delta)| \\ |\sin(\delta)| \exp[i\gamma] \end{pmatrix} \exp[i\delta] \\ &= \frac{1}{\sqrt{2}} \begin{pmatrix} |O_1| \\ |O_2| \exp[i\gamma] \end{pmatrix} \exp[i\delta]\,. \end{aligned} \tag{5.23}$$

where $\gamma$ is $0^o$ if $\delta$ is in the interval $[0; \pi/2] \cup [\pi; 3\pi/2]$ and $\pi$ elsewhere. It must also be noted that Eq. 5.23 gives normalized amplitudes. Figure 5.16 presents the comparison between theoretical (Eq. 5.23) and experimental values for different orientations $\delta$ of the polarizer. The correlation between experimental and theoretical data is better for $|O_2|$ than for $|O_1|$, because $\boldsymbol{R}_1$ undergoes one reflection fewer than $\boldsymbol{R}_2$ before reaching the CCD camera (see Figure 5.1).

To evaluate now the measurement of the phase difference $\Delta\varphi_{\boldsymbol{O}}$, we take a quarter-wave plate oriented at an angle $\delta$ ($\delta = 0^o$ to $180^o$), illuminated by a linearly polarized wave oriented at $45^o$, as the object (Fig. 5.17). To estimate the value of $\Delta\varphi_{\boldsymbol{R}}$ (Eq. 5.11), we create a reference area in the image by placing a linear polarizer oriented at $45^o$ in a part of the beam after the quarter-wave plate. In this area (part $B$ in Figs. 5.17 and 5.18), the theoretical phase difference between the components of the object wave is zero. The reconstructed phase difference distribution presented in Fig. 5.18

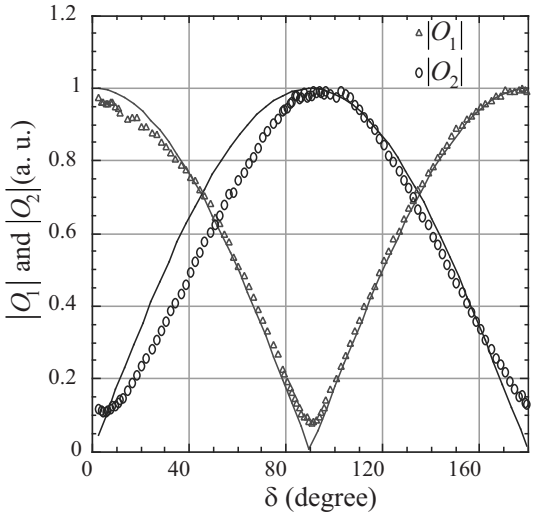


*Figure 5.16: Theoretical (solid line) and experimental (dots) values for $|O_1|$ and $|O_2|$ as a function of the orientation $\delta$ of polarizer P1.*

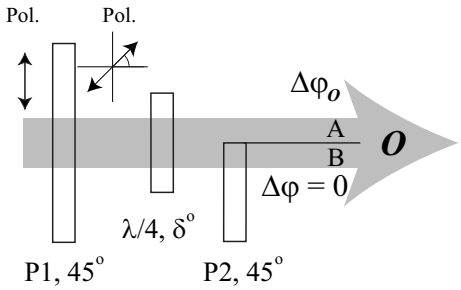


*Figure 5.17: Setup in the object arm for the results presented in Figs. 5.18 and 5.19. $\lambda/4$ is a quarter wave plate oriented at an angle $\delta$; P1 and P2 are polarizers oriented at $45^o$. Part B, which crosses P2 serves as reference area for measuring the phase difference between the two reference waves.*

permits us therefore to determine the phase difference $\Delta\varphi_{\mathbf{R}}$ between the two reference waves by measuring the phase difference in part *B*. In the other part of the object wave (part *A* in Figs. 5.17 and 5.18), the measured phase difference is given by Eq. 5.11 and $\Delta\varphi_{\boldsymbol{O}}$ can be obtained when the measured value of $\Delta\varphi_{\boldsymbol{R}}$ is added. Theoretically the Jones vector for the light emerging from a quarter-wave plate oriented at $\delta^o$ and illuminated by a linearly polarized wave at $45^o$ is written

$$\boldsymbol{J_O} = \frac{1}{\sqrt{2}} \begin{bmatrix} a\cos^2(\delta) + b\sin^2(\delta) & \sqrt{2}i\sin(\delta)\cos(\delta) \\ \sqrt{2}i\sin(\delta)\cos(\delta) & b\cos^2(\delta) + a\sin^2(\delta) \end{bmatrix} \begin{pmatrix} 1 \\ 1 \end{pmatrix}, \qquad (5.24)$$

where $a = \exp[i\pi/4]$ and $b = \exp[-i\pi/4]$.

The function describing $\Delta\varphi_{\boldsymbol{O}}$, derived from Eq. 5.24 in relation to $\delta$, is reported in the plot of Fig. 5.19, which also presents experimental data for comparison.

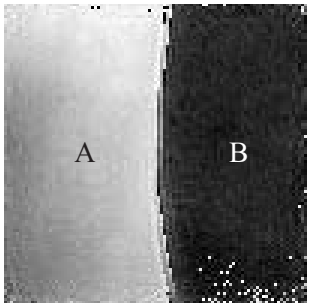


*Figure 5.18: Image of phase difference induced by a quarter wave plate. A is an area in the object surface (quarter wave plate) and B, is an area in the reference part used to estimate $\Delta\varphi_{\boldsymbol{R}}$. The effective value of $\Delta\varphi_{\boldsymbol{O}}$ is calculated by subtracting $\Delta\varphi_{\boldsymbol{R}}$ from the phase difference measured in A.*

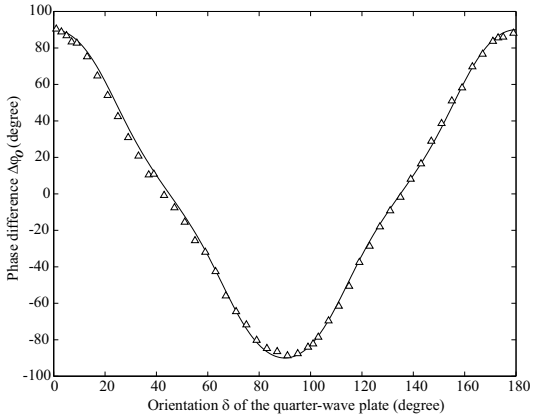


*Figure 5.19: Theoretical (solid line) and experimental (triangles) values of the phase difference between the horizontal and vertical components of the SOP induced by a quarter-wave plate oriented at an angle $\delta$ and illuminated by a linearly polarized wave at $45^o$.*

To illustrate its polarization imaging capabilities, the method is applied to study a polymethylmethacrylate specimen (PMMA) for which a birefringence can be induced by applying a constraint. Figure 5.20 presents the setup used to create the stressed PMMA specimen. The illuminating beam (circle) is polarized linearly at $45^o$ and a part of it (part $A$) passes through the specimen while another (part $B$), serving as reference area, passes outside the specimen. Examples of results obtained with this specimen are presented in Fig. 5.21. Part $A$, delimited by white lines, is the PMMA specimen and part $B$ is the reference area. The arrows indicate the compression point. Figures 5.21(a) and (b) represent the spatial distribution of $|O_1|$ and $|O_2|$ respectively. $\varepsilon$ is presented in Figure 5.21(c). Figures 5.21(d) and (e) present the reconstructed phase distributions corresponding respectively to the horizontal and vertical components of the SOP. As the phase distribution is defined as modulo $2\pi$, phase jumps (between $-\pi$ and $\pi$) appear in the images. The birefringence properties of

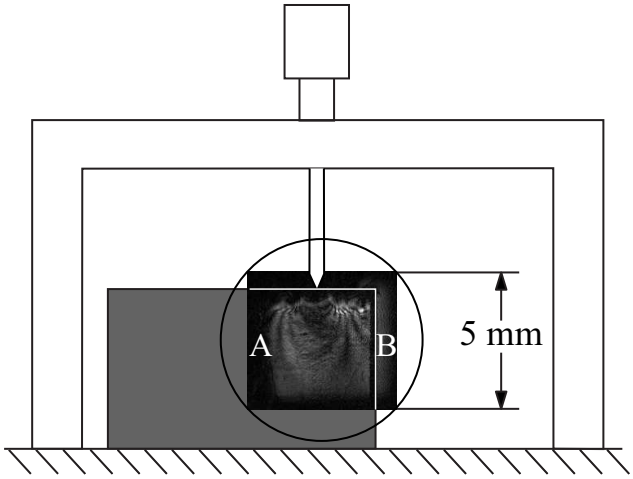


*Figure 5.20: Compressed PMMA specimen. The circle is the illuminated area. Part A is the illuminated area of the plastic sheet and part B serves as reference area.*

the specimen are expressed by a different phase delay for the two components of the object wave and are imaged by the spatial distribution of $\Delta\varphi_O$ presented in Fig. 5.21(f).

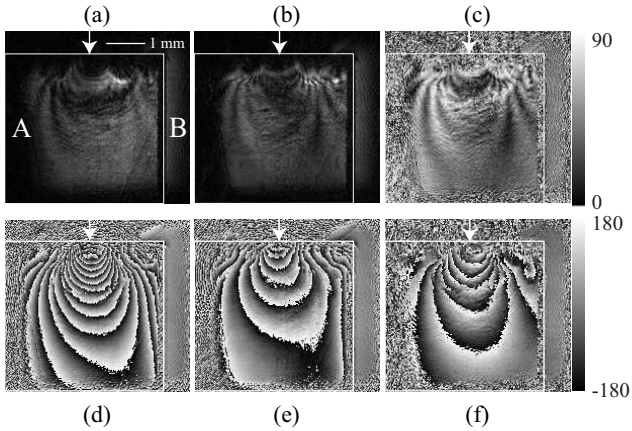


*Figure 5.21: Images obtained for a stressed PMMA specimen. (a) $|O_1|$; (b) $|O_2|$; (c) $\varepsilon$; (d) $\arg(O_1)$; (e) $\arg(O_2)$; (f) $\Delta\varphi_O$. The arrow indicates the compression point and the white lines delimit the PMMA specimen.*

## 5.4 Discussion

The obtained results show that digital holographic imaging with two reference waves of perpendicular polarization states can be used to obtain the distributions of the Jones vector at the surface of the specimen with a single image acquisition. The method proposed here combines the standard experimental difficulties of polarization measurements with those of interferometry and is therefore sensitive to external perturbations such as

mechanical vibrations, thermal drifts and air movements. The precision of the measurements depends on the quality of the interfering wave fronts and on the precision of their polarization states adjustment. For this reason, high quality optical components introducing low wavefront distortion and with well-defined birefringent behavior are recommended. An important source of noise comes from parasitic reflections occurring at optical interfaces in the setup. Even image processing methods, as spatial filtering (see Section 2.2.2) and anti-reflection coatings, can reduce these effects; it remains difficult to suppress them completely because of the inherently high sensitivity of interferometric methods to low light intensities. Because of the high coherence of the light source, this parasitic light interferes with the reference and object waves, and its main effect is that the measured values of $|O_1|$ and $|O_2|$ are never equal to zero, as can be seen in Fig. 5.16.

Another crucial point is that the two polarizers in the reference arms must be very carefully adjusted so that the linear polarization states of $\boldsymbol{R}_1$ and $\boldsymbol{R}_2$ form a perpendicular base. In particular, this adjustment must take into account the fact that the reflection by a beam splitter slightly modifies the polarization state. In Fig. 5.16, we can see that the correlation between experimental and theoretical data is better for $|O_1|$ than for $|O_2|$ . This is because $\boldsymbol{R}_1$ undergoes one reflection fewer than $\boldsymbol{R}_2$ before reaching the CCD camera.

The adjustment of the three half-wave plates, in particular the one in the object arm (Fig. 5.1), is also very important and must be ideally performed so that, without object, equal amplitudes and phases are obtained for the two polarization components. For the results presented here, the polarizers and the half-wave plates are adjusted to optimize phase difference measurements for which an excellent agreement between theory and experiment is obtained (see Fig. 5.19). However, this adjustment is not optimal for amplitude measurements and, as can be seen in Fig. 5.16, the maximum of $|O_1|$ and the minimum of $|O_2|$ are shifted by approximately $4^o$.

It is important to point out also that the precision of the phase difference determination depends on the polarization state of the object wave. In an extreme case, if the object wave is horizontally polarized, no interference occurs with $\boldsymbol{R}_2$ and the phase difference is undetermined. Therefore, to obtain maximum precision, the illuminating beam polarization must be adapted, depending on the specimen. The main drawback of the method is that the presence of a reference area is required for measuring $\Delta\varphi_{\boldsymbol{R}}$ (the phase difference between the two reference waves). It cannot be calibrated in the beginning of an experiment because mechanical vibrations, air tur-

bulence and thermal effects modify this value during the measurement duration. However, the reference area can be avoided for imaging purposes if only relative information is needed.

Results obtained with a stressed PMMA specimen (Fig. 5.21) demonstrate the capacity of the method to provide images of SOP at the surface of a specimen. As expected the stress field induces black curves in Figs. 5.21(a) and (b). These figures could be obtained with a standard polariscope [Ram00], with a first polarizer oriented at $45^o$ (as illuminating beam) and with a second polarizer oriented at $0^o$ and $90^o$ as analyzer. The interesting point in Fig. 5.21 is that we can observe that the images corresponding to the two orthogonal components are clearly different because of the birefringent property of the specimen. Figures 5.21(c) and (f), which compare the amplitude-contrast and phase-contrast values, show the difference between the two orthogonal components and reveal therefore the birefringence induced by the constraint. Standard polariscopes could obtain these images, but only with several image acquisitions, versus only one for the method presented here.

Another characteristic of the method that remains to be discussed is the transverse resolution. As presented here, the transverse resolution approaches 40 $\mu$m. However, microscopic observations with the same transverse resolution as classical optical microscopy can be achieved with an implementation that includes a MO, as presented in next chapter.

# Chapter 6

# Application of DHM Polariscope

## 6.1 Introduction

Different techniques allow to image SOP but most of them need polarizing-analyzing optics (polarizors, rotators and retarders) that must be adjusted at various settings, requiring a long setting time compared to the acquisition performances of a CCD. The temporal resolution can be improved by use of a liquid-crystal universal compensator in place of analyzing optics [Old95], but the technique still needs several images to reconstruct SOP. Finally other methods very similar to holographic ones allow to image SOP with a single acquisition [Oka03,Oht94], but their main drawback is a relatively low spatial resolution compared to polarizing-analyzing techniques that can use a MO to improve the spatial resolution.

In this chapter, by the introduction of a MO in the setup, the polarization digital holography (DH-Polariscope) method evolves to polarization digital holographic microscopy (DHM-Polariscope). To illustrate the method a thin concrete specimen and a bent optical fiber are used to study the induced birefringence. To evaluate the precision of the method, the birefringence due to fiber internal stresses is measured by DHM-Polariscope and compared with the birefringence profile captured with a high-resolution standard method.

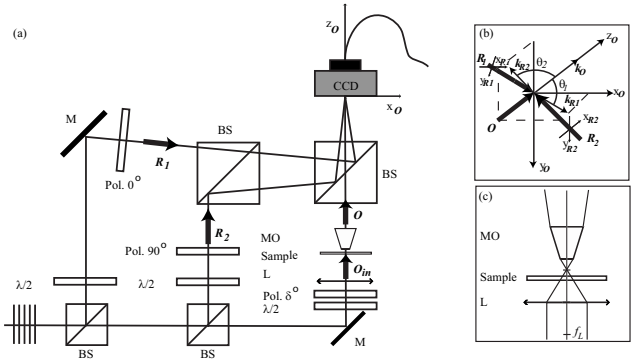


*Figure 6.1: (a) Experimental setup.* $\boldsymbol{O_{in}}$ *illuminating wave,* $\boldsymbol{O}$ *object wave;* $\boldsymbol{R}_1$ *and* $\boldsymbol{R}_2$*, polarized reference waves; Pol.* $\alpha^o$*, polarizer oriented at* $\alpha^o$*;* $\lambda/2$*, half wave plate; M, mirror; BS, beam splitter; L, lens with focal length* $f_L$*; MO, the microscope objective and CCD, the couple-charge device. (b) detail showing the off-axis geometry at the incidence on the CCD. The* $x_{\boldsymbol{O}}y_{\boldsymbol{O}}$ *plane is parallel to the CCD camera.* $\boldsymbol{R}_1$ *in the* $y_{\boldsymbol{O}}z_{\boldsymbol{O}}$ *plane and* $\boldsymbol{R}_2$ *in the* $x_{\boldsymbol{O}}z_{\boldsymbol{O}}$ *plane are coming from different directions. (c) detail showing the ray tracing in the object arm. The collimated beam focalized with the lens L illuminates a small portion of the specimen placed between the lens L and its focal plane. The MO magnifies the specimen and produces produce a divergent beam that covers the entire chip area of the CCD.*

# 6.2 Method

## 6.2.1 Setup

The DHM-Polariscope geometry presented in Fig. 6.1 is designed for transmission imaging with transparent specimens. The basic architecture is that of a Mach-Zehnder interferometer with two orthogonally linearly polarized reference waves that interfere with an object wave in off-axis geometry as presented in Fig. 6.1 (b).

The incident object plane wave $\boldsymbol{O_{in}}$ is focalized by a lens $L$ (focal $f_L = 30mm$, $NA \simeq 0.07$) to illuminate a small portion of the specimen with a known linear SOP determined by the orientation of a polarizer [Pol. $\delta^o$ in Fig. 6.1(a), $\delta = 45^o$ for the applications presented here]. The position of the specimen is adjusted to produce a magnified image of the specimen with the MO at a distance $d$ behind the CCD ($d \simeq 5$ cm). The transmitted light collected by the MO produces a wavefront called object wave $\boldsymbol{O}$. The SOP of the object wave is different from the illuminating wave $\boldsymbol{O_{in}}$ and results from the specimen birefringence properties integrated along the propagation direction. Then the wave $\boldsymbol{O}$ diverges from the MO to cover the entire chip of the CCD placed at 15 cm from the MO. To simplify the theoretical analysis of polarization, we define a single propagation vector $k_{\boldsymbol{O}}$ perpendicular to the CCD plane $x_{\boldsymbol{O}}y_{\boldsymbol{O}}$.

The reference waves $\boldsymbol{R}_1$ and $\boldsymbol{R}_2$, respectively polarized horizontally

(along $x_{R1}$) and vertically (along $y_{R2}$) by polarizers [Pol. in Fig. 6.1(a)], reach the CCD camera with a small incidence angle $\theta_1$ and $\theta_2$ respectively ($\theta_1 = 2.5^o$, $\theta_2 = 3^o$). To avoid any interference between the reference waves, the vectors $x_{R1}$ and $y_{R2}$ should be orthogonal; therefore, the directions of propagation $k_{R1}$ and $k_{R2}$ should be respectively in the planes $y_O z_O$ and $x_O z_O$.

### 6.2.2 Hologram

Figure 6.2 presents a digital hologram recorded with the experimental setup presented in Fig. 6.1, with a 10 times magnification MO. The specimen is a non-stripped bent optical fiber doped with 9 mol.% Germanium (made by Cabloptic SA, Switzerland) immersed in a refractive index liquid of 1.4571 at 632 nm and room temperature ($25^o$C) matching the cladding refractive index (1.45704 at 632 nm) of the fiber.

We can see in Fig. 6.2 that the hologram appears as the superposition of two interference fringes patterns, one interference pattern for each reference wave. These fringes are curved because of the phase curvature produced by the MO and are not concentric with respect to the center of the image as a consequence of the off-axis geometry.

*Figure 6.2: Hologram of the non-stripped bent fiber. The magnifying glass permits to visualize the two different curved fringes patterns corresponding to the interference of the object wave with the two orthogonally polarized reference waves.*

## 6.3 Concrete Specimen Measurement

To illustrate the DHM-Polariscope, a 25 $\mu$m thin concrete specimen is studied. The concrete contains different kind of crystals (calcite, silica,...) coming from the stones that compose it. These strongly birefringent crystals form aggregates that could have different orientations. The Figure 6.3

shows the amplitude (a,b) and phase images (d,e) of a the thin concrete specimen for the horizontal (a,d) and vertical (b,e) SOP components. Because of the crystals, a high contrast appears in $\varepsilon$ (c) and phase difference (f) images. The SOP images allow to distinguish different aggregates that are mostly invisible in amplitude images and only partially visible in phase images. Finally, the Fig. 6.3 shows that SOP images are more uniform in the aggregate areas. Indeed, the contributions of none birefringent elements in the absorption or in the optical path length integrated along the specimen are equal for the two polarizations and therefore disappear in $\varepsilon$ and the phase difference images.

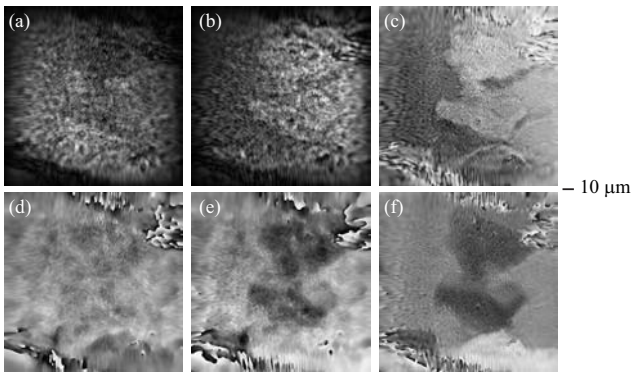


*Figure 6.3: Reconstructed images of a 25 µm thin concrete specimen. $\varepsilon$ (c) and the phase difference (f) are computed from the amplitude images (a-b) and the phase images (d-e) images of horizontal (a-d) and vertical (b-e) components.*

## 6.4 Measurement of Stress in Optical Fiber

### 6.4.1 Bent Optical Fiber

The goal of this section is to show that the DHM-Polariscope method permits to image SOP of a microscopic object. A bent fiber is used because it is known that the stress induced by the bending creates birefringence [ED99]. The idea in this section is not to demonstrate the quantitative possibility of the method (discussed in next Section 6.4.2), but to present the imaging capability. Indeed to analyze quantitatively birefringence, it is better to strip off the coating of the fiber to study only the cladding. Here SOP parameters imaging of the entire fiber will be performed.

Figure 6.4 compares the amplitude and phase images for a unbent fiber (a-d) and a bent fiber (e-h). The fiber core is visible in the amplitude images in the center of the cladding region [(i) in Fig. 6.4]. On the right, the coating region (j) and the refractive index liquid region (k) are shown. The

illuminating wave is transmitted through the entire fiber and therefore the images presented in Figs. 6.4 and 6.5 are the integration of light properties over the depth of the fiber.

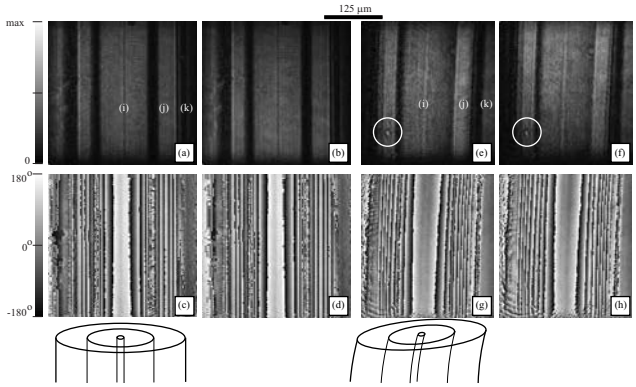


*Figure 6.4: Amplitude and phase reconstructions for a unbent fiber (a-d) and for a bent fiber (e-h). (i) is the cladding region with focusing core in the middle, (j) is the coating region and (k) is the refractive index liquid region. (a,e)* $|O_1|$*, (b,f)* $|O_2|$*, (c,g)* $\arg(O_1)$*, (d,h)* $\arg(O_2)$*. Circles indicate positions of inhomogeneity in* $\varepsilon$ *due to some dust particles. The center of curvature is on the right of bent fiber reconstructed images.*

The borders between coating and cladding appear as dark lines on amplitude images and have an undefined phase. This phenomenon is explained by the high refractive index differences between each side of the borders, therefore the light passing near the borders undergoes a great deviation and is not collected by the MO so that no light coming from these areas reaches the CCD sensor.

There is an important difference of optical path length because of the high mismatch between the refractive indices of liquid and coating and between coating and cladding; therefore phase jumps appear in the phase images. On the other hand, a particle of dust floating in the liquid gives some contributions in amplitude [inside circles in Fig. 6.4(e-f)].

Figure 6.5 presents the SOP parameters of the unbent (a-b) and bent fiber (c-d). It can be seen that the effect of the dust particle disappears on the $\varepsilon$ image [Fig. 6.5(c)]. The reason of this phenomenon is that this dust particle does not affect the polarization of the illuminating wave.

Figure 6.6 presents SOP values measured along the transverse section. A rectangular ROI with the major axis perpendicular to the fiber is selected on the SOP images (dashed rectangle in Fig. 6.5). The mean value along the small axis direction is taken for each point of the major axis. The $\varepsilon$ parameter and the phase difference mean profile are plotted for the SOP images of the unbent and bent fibers.

The graph of Fig. 6.6(a) shows an uniform $\varepsilon$ for the unbent fiber except in the borders areas where $\varepsilon$ is not well defined. For the bent fiber, $\varepsilon$

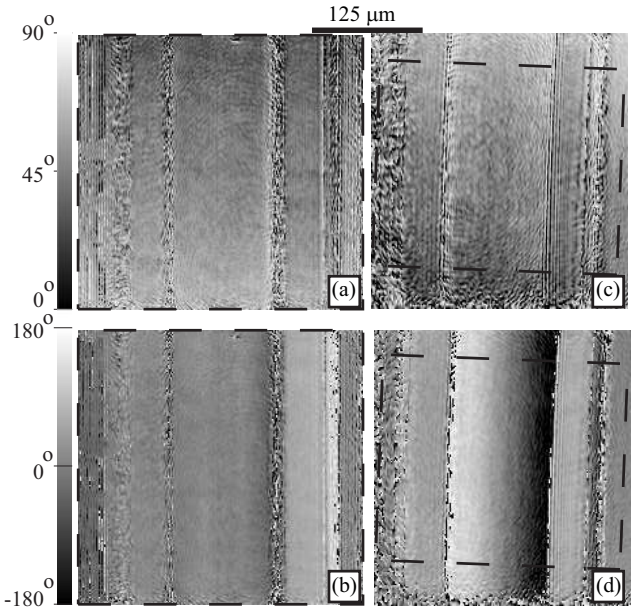


*Figure 6.5: SOP images reconstructed from images of Fig. 6.4: (a,c) $\varepsilon$ and (b,d) the phase difference $\Delta\varphi_{\mathbf{O}}$ for an unbent fiber (a,b) and a bent fiber (c,d). Mean profiles of Fig. 6.6 are defined along the major axis of dashed dark rectangles*

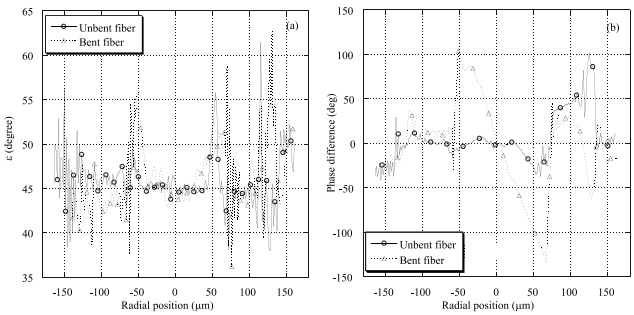


*Figure 6.6: Graphs of mean profiles defined by rectangle of Fig. 6.5. (a) is $\varepsilon$ and (b) the phase difference.*

increases symmetrically from the center of the cladding region. The graph of Fig. 6.6(b) shows first that without bending, the phase difference is not constant. Indeed, the phase difference profile in the cladding region changes because of the fiber internal stress due to the fabrication process and the right coating region has a phase difference of about $40^o$, due to the residual stress resulting from the winding of the fiber.

In the case of the bent fiber, the phase difference in the cladding region follows the theory [ED99]. Indeed, the refractive index changes only in the direction perpendicular to the fiber axis (horizontal refractive index) and is constant in the direction parallel to the fiber axis (vertical refractive index). Furthermore, the horizontal refractive index increases for compressed areas and decreased for expanded area. Thus, because the phase difference is proportional to the opposite of the horizontal refractive index (see Eq. 1.17),

it decreases in a compressed area and increases in an expanded area.

The bending of the fiber induces birefringence in the coating too. The comparison between the two curves indicates that the phase difference for the coating increases in the expanded area and decreased in the compressed area when the fiber is bent as we can expect for the same reason explained before.

This example shows that the introduction of a MO permits a 2D mapping of SOP parameters for microscopic objects. In the case of an optical fiber, the comparison between SOP images of an unbent fiber and a bent fiber reveals clearly a SOP modification due to the bending. The SOP images contrast is also due uniquely to the optical properties induced by the stresses. Therefore a map of the stresses in the optical fiber is obtained without suppressing the coating. It can be interesting for a quality control application for instance.

### 6.4.2 Internal Stress in Optical Fiber

To evaluate the resolution of the phase difference imaging obtained with DHM-Polariscope, the same fiber with suppressed coating and without bending is used as specimen. The goal is to image the birefringence due to the internal stress created during the fiber fabrication process [Chu82]. The fiber is immersed in the same refractive index liquid as before. Figure 6.7 presents reconstructed images achieved with a 20 times magnification MO and a numerical aperture $NA = 0.5$: (a) $\arg(O_1)$, (b) $\arg(O_1)$ and (c) the phase difference. Because the refractive index liquid is very close to the cladding refractive index, there are no phase jumps and the core is visible in the center of the fiber. The phase difference image shows clearly the birefringence due to internal stress. However, to evaluate the precision, a comparison with a reference method is necessary.

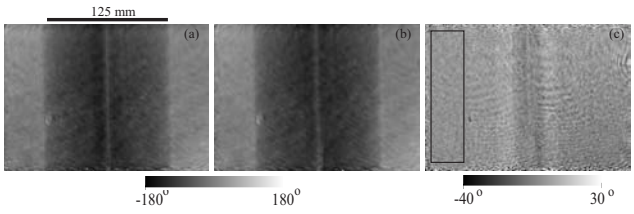


*Figure 6.7: (a)* $\arg(O_1)$*, (b)* $\arg(O_2)$ *and (c) phase difference. The rectangle delineates the area where std phase difference is measured.*

The setup used to obtain the reference birefringence profile is similar to the one presented in Ref. [Par02] and is a further development of a method already demonstrated in 1982 [Chu82]. Light from a He-Ne laser is

scattered by a rotating diffuser, collected by a lens, and linearly polarized at an angle $\rho$. The polarized light passes successively through a quarter-wave plate and the optical fiber. The fiber axis is adjusted to an angle of $45^o$ with respect to the optical axes of the quarter-wave plate. Thus, the light is again linearly polarized after having passed the fiber. The axis of polarization of the beam leaving the fiber is shifted by a certain angle $\Delta\rho$ with respect to the axis of the beam impinging on the quarter-wave plate. The angle shift $\Delta\rho$ is proportional to the birefringence introduced by the fiber. The shift in polarization angle is converted to an intensity modulation by an analyzer following the optical fiber. The resulting intensity distribution of the light behind the analyzer is

$$I(x,z) = I_{\max} \sin^2 \left[\rho + \Delta\rho(x,z)\right]. \tag{6.1}$$

The intensity profile (Eq. 6.1) is captured by a CCD camera for different angles $\rho$ of the light impinging on the quarter-wave plate. This allows the determination of the intensity minima with high accuracy, using a least-square fitting algorithm. At minimum intensity, $\rho = -\Delta\rho(x,z)$ in Eq. 6.1. Thus the spatial profile of the fiber induced birefringence can be determined. The fiber is imaged on the CCD camera using a 20 times MO with a numerical aperture of 0.5, limiting the spatial resolution to about 0.8 $\mu$m. Std in $\Delta\rho$ is better than 0.1 degree.

As to compare the DHM-Polariscope with the reference method, a phase difference mean profile is taken from the Fig. 6.7(c) by computing the average phase difference on each column. Figure 6.8 presents the comparison between the phase difference measured with the reference method (solid line) and with the DHM-Polariscope method (triangle).

In the reference method the intensity is measured over 36 different angles to determine the angle of minimum intensity. This leads to a phase difference resolution of 0.1 degree. In contrary, to obtain a phase difference profile by DHM-Polariscope, only one single acquisition is performed. In this case a one-dimensional phase difference resolution smaller than 2 degrees is obtained, which is comparable to standard methods [ED99]. The two-dimensional phase difference resolution is evaluated by considering std measured out of the fiber area (rectangle in Fig. 6.7) that gives a 2D phase difference resolution about 6 degrees.

The lateral resolution of DHM is approximately equal to the diffraction limit of the MO as shown in Ref. [Cuc99b]. Therefore, the spatial resolution should be $0.61\lambda/NA \simeq 0.8\mu$m. However, because the MO was not used in its best performance in terms of spatial resolution for technical reasons, the effective spatial resolution is evaluated to about 2 $\mu$m by considering

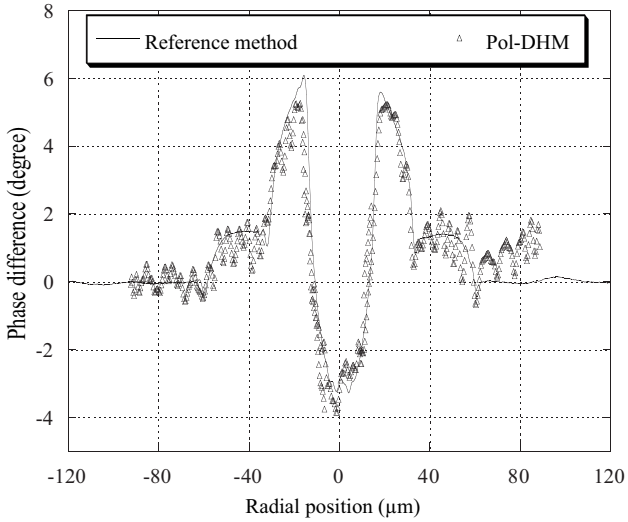


*Figure 6.8: Comparison between the phase difference measurements performed with the reference method (solid line) and performed with the DHM-Polariscope.*

that the edges and middle of fiber core (6.7 $\mu$m) are well distinguishable. Figure 6.9 presents the $|O_1|$ reconstruction of a standard USAF target hologram recorded with the same setup. The smaller elements corresponding to 228 lines per millimeter are distinguishable, and therefore it confirms a spatial resolution better than 2 $\mu$m.

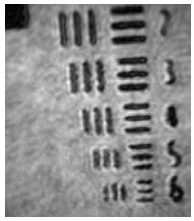

*Figure 6.9: $|O_1|$ image reconstruction of standard USAF target hologram recorded with a X20 MO. The smallest elements correspond to 228 lp/mm.*

## 6.5 Conclusion

In this chapter, the existing techniques of polarization digital holography, presented in Chapter 5, and DHM, presented in the previous chapters, were joined together to achieve a new type of polarized light microscope, the DHM-Polariscope. We have shown that this method permits, by the acquisition of a single hologram in off-axis geometry, to image the SOP parameters of the object wave transmitted through a microscopic sample with a spatial resolution about 2 $\mu$m. Concrete specimen, non-stripped bent and unbent fibers were used as microscopic specimens to illustrate the

principle of the method and its imaging capability. Finally, birefringence induced by internal stress in a stripped optical fiber was measured and compared with the results obtained with a reference method. The results of the two methods match quite well and the DHM-Polariscope has a phase difference resolution better than 6 degrees that is comparable to standard methods. The next step of the DHM-Polariscope is to image SOP of other birefringent objects, in transmission and reflection configuration, biological specimens in particular.

# Chapter 7

# Conclusion

This thesis presents a digital holographic method allowing, from a single hologram acquisition, the reconstruction of the entire wavefront reflected by or transmitted through a specimen: the amplitude, the phase, and as a new feature, the polarization state.

First, we demonstrated that a numerical parametric lens applied in the reconstruction plane defined using a polynomial function enables to compensate digitally for the wavefront deformations in digital holographic microscopy, even in the presence of strong, high order aberrations. The proposed method uses the hologram itself to evaluate automatically and accurately the values of parameters involved by the numerical parametric lens; thanks to polynomial fitting procedures applied on phase data extracted along profiles or inside 2D areas defined in region of the field of view, where specimen contribution are known to be constant. We demonstrated also that parametric values associated to high order terms of the numerical parametric lens can be calibrated using a flat reference specimen. Finally, we demonstrate that the proposed method can be applied to compensate for the specimen shape, that allows to image and to evaluate the surface quality of specimen with curved surface. The procedure is applied to characterize a micro-lenses array and the vertex of a metallic sphere. These applications show that DHM and the shape compensation procedure permit to obtain a flattened representation of curved specimens that provide a straightforward access to the surface state of the specimen, independently from the specimen shape. Furthermore, the fitting procedure in terms of Zernike polynomials coefficients performs quantitative measurements about aberrations of micro-optics.

Secondly, the concept of numerical parametric lens was generalized to be applied in the hologram plane. We demonstrated that this numerical parametric lens allows a numerical shifting, a magnification and especially

a complete aberrations compensation. We introduced also the concept of conjugated reference hologram as a simple calibration method for defining the numerical parametric lens without fitting procedure but needing a reference hologram. The results illustrate an interesting feature of digital holographic techniques, which offer unique possibilities for the digital processing of wave fronts. In particular, the possibility to perform accurate phase measurements using optical systems comprising strong aberrations offers attractive possibilities for the development of cost-effective solutions dedicated to metrology applications requiring interferometric resolutions.

Finally, we demonstrated that a new application of digital holography called DHM-polariscope permits, by the acquisition of a single hologram in off-axis geometry, to image the state of polarization parameters of the object wave transmitted through or reflected by a microscopic specimen with a lateral resolution better than 2 $\mu$m. Indeed, experiments and simulations evaluate the resolution of the method that is comparable to standard methods, but with the advantage of a single acquisition. Examples of measurement of birefringence induced in concrete sample, non-stripped bent and unbent fibers or induced by internal stress in a stripped optical fiber were achieved. A comparison with a reference method allowed to estimate the phase difference resolution better than 6 degrees.

# Bibliography


[Ahn05] A. Ahn, C. Yang, A. Wax, G. Popescu, C. Fang-Yen, K. Badizadegan, R. R. Dasari and M. S. Feld. "Harmonic phase-dispersion microscope with a Mach-Zehnder interferometer". Appl. Opt. **44**(7): 1188–1190 (2005).

[Ale04] S. Alexandrov, R. Meredith, T. McIntyre and A. Zvyagin. "Holographic digital Fourier microscopy for selective Imaging of biological tissue". International journal of imaging systems and technology **14**(6): 253–258 (2004).

[All03] E. Allaria, S. Brugioni, S. D. Nicola, P. Ferraro, S. Grilli and R. Meucci. "Digital holography at 10.6 $\mu$m". Opt. Commun. **215**(4-6): 257–262 (2003).

[Alm04] P. Almoro, M. Cadatal, W. Garcia and C. Saloma. "Pulsed full-color digital holography with a hydrogen Raman shifter". Appl. Opt. **43**(11): 2267–2271 (2004).

[Apo04] V. Apostolopoulos, L. Laversenne, T. Colomb, C. Depeursinge, R. P. Salathé and M. Pollnau. "Femtosecond-irradiation-induced refractive-index changes and channel waveguiding in bulk Ti3+:Sapphire". Appl. Phys. Lett. **85**(7): 1122–1124 (2004).

[Awa04] Y. Awatsuji, M. Sasada and T. Kubota. "Parallel quasi-phase-shifting digital holography". Appl. Phys. Lett. **85**(6): 1069–1071 (2004).

[Bac05] B. L. Bachim and T. K. Gaylord. "Microinterferometric optical phase tomography for measuring small, asymmetric refractive-index differences in the profiles of optical fibers and fiber devices". Appl. Opt. **44**(3): 316–327 (2005).

[Beg99] D. Beghuin, E. Cuche, P. Dahlgren, C. Depeursinge, G. Delacretaz and R. P. Salathe. "Single acquisition polarisation imaging with digital holography". Electron. Lett. **35**(23): 2053–2055 (1999).

[Ben92] J. M. Bennett. "Recent developments in surface roughness characterization". Measurement Science and Technology **3**(12): 1119–1127 (1992).

[Boe97] J. D. Boer, T. E. Milner, M. J. C. van Gemert and J. S. Nelson. "Two dimensional birefringence imaging in biological tissue by polarization-sensitive optical coherence tomography". Opt. Lett. **22**(12): 934–936 (1997).

[Boe98] J. D. Boer, Z. Chen, J. S. Nelson, S. Srinivas and A. Malekafzali. "Imaging thermally damaged tissue by polarization sensitive optical coherence tomography". Opt. Express **3**(6): 212–218 (1998).

[Bor80] M. Born and E. Wolf. *Principles of Optics* (Pergamon Press, New York, 1980).

[Bor05] D. N. Borza. "Mechanical vibration measurement by high-resolution time-averaged digital holography". Measurement Science and Technology **16**(9): 1853–1864 (2005).

[Bra97] J. Braat. "Analytical expressions for the wave-front aberration coefficients of a tilted plane-parallel plate". Appl. Opt. **36**(32): 8459–8466 (1997).

[Car04] D. Carl, B. Kemper, G. Wernicke and G. von Bally. "Parameter-optimized digital holographic microscope for high-resolution living-cell analysis". Appl. Opt. **43**(36): 6536–6544 (2004).

[Cha69] E. B. Champagne and N. G. Massey. "Resolution in holography". Appl. Opt. **8**(9): 1879–1885 (1969).

[Cha06a] F. Charrière, J. Kühn, T. Colomb, F. Monfort, E. Cuche, Y. Emery, K. Weible, P. Marquet and C. Depeursinge. "Characterization of microlenses by digital holographic microscopy". Appl. Opt. **45**(5): 829–835 (2006).

[Cha06b] F. Charrière, A. Marian, T. Colomb and C. Depeursinge. "Amplitude point spread function measurement of high NA microscope objectives by digital holographic microscopy" (in preparation) (2006).

[Cha06c] F. Charrière, A. Marian, F. Montfort, J. Kuehn, T. Colomb,E. Cuche, P. Marquet and C. Depeursinge. "Cell refractive index tomography by digital holographic microscopy". Opt. Lett. **31**(2): 178–180 (2006).

[Chu82] P. L. Chu and T. Whitbread. "Measurement of stresses in optical fiber and preform". Appl. Opt. **21**(23): 4241–4245 (1982).

[Coe02] S. Coetmellec, D. Lebrun and C. Ozkul. "Application of the two-dimensional fractional-order Fourier transformation to particle field digital holography". J. Opt. Soc. Am. A-Opt. Image Sci. Vis. **19**(8): 1537–1546 (2002).

[Col71] R. J. Collier, D. B. Burckhardt and L. H. Lin. *Optical holography* (New York, 1971).

[Col02a] T. Colomb, E. Cuche, P. Dahlgren, A. M. Marian, F. Montfort, C. D. Depeursinge, P. Marquet and P. J. Magistretti. "3D imaging of surfaces and cells by numerical reconstruction of wavefronts in Digital Holography applied to transmission and reflection microscopy". In "2002 Ieee International Symposium on Biomedical Imaging, Proceedings", (2002), pp. 773–776.

[Col02b] T. Colomb, P. Dahlgren, D. Beghuin, E. Cuche, P. Marquet and C. Depeursinge. "Polarization imaging by use of digital holography". Appl. Opt. **41**(1): 27–37 (2002).

[Col04] T. Colomb, E. Cuche, F. Montfort, P. Marquet and C. Depeursinge. "Jones vector imaging by use of digital holography: simulation and experimentation". Opt. Commun. **231**(1-6): 137–147 (2004).

[Col05a] T. Colomb, E. Cuche and C. Depeursinge. "Birefringence measurement by use of digital holographic microscopy: examples with fiber optics and concrete samples". In "Proc. SPIE", (Munich, 2005), vol. 5856, pp. 1022–1027.

[Col05b] T. Colomb, F. Dürr, E. Cuche, P. Marquet, H. Limberger, R.-P. Salathé and C. Depeursinge. "Polarization microscopy by use of digital holography: application to optical fiber birefringence measurements". Appl. Opt. **44**(21): 4461–4469 (2005).

[Col06] T. Colomb, E. Cuche, F. Charrière, J. Kühn, N. Aspert, F. Montfort, P. Marquet and C. Depeursinge. "Automatic procedure for aberration compensation in digital holographic microscopy and applications to specimen shape compensation". Appl. Opt. **45**(5): 851–863 (2006).

[Cop04] G. Coppola, P. Ferraro, M. Iodice, S. D. Nicola, A. Finizio and S. Grilli. "A digital holographic microscope for complete characterization of microelectromechanical systems". Measurement Science and Technology **15**(3): 529–539 (2004).

[Coq95] O. Coquoz, R. Conde, F. Taleblou and C. Depeursinge. "Performances of Endoscopic Holography with a Multicore Optical- Fiber". Appl. Opt. **34**(31): 7186–7193 (1995).

[Cuc99a] E. Cuche, F. Bevilacqua and C. Depeursinge. "Digital holography for quantitative phase-contrast imaging". Opt. Lett. **24**(5): 291–293 (1999).

[Cuc99b] E. Cuche, P. Marquet and C. Depeursinge. "Simultaneous amplitude-contrast and quantitative phase-contrast microscopy by numerical reconstruction of Fresnel off-axis holograms". Appl. Opt. **38**(34): 6994–7001 (1999).

[Cuc00a] E. Cuche. "Numerical reconstruction of digital holograms: application to phase-contrast imaging and microscopy" (2000).

[Cuc00b] E. Cuche and C. Depeursinge. "Method for simultaneous amplitude and quantitative phase contrast imaging by adjusting reconstruction parameters for definition of digital replica of reference wave and aberration parameters correction digitally" (2000).

[Cuc00c] E. Cuche, P. Marquet and C. Depeursinge. "Aperture apodization using cubic spline interpolation: application in digital holographic microscopy". Opt. Commun. **182**(1-3): 59–69 (2000).

[Cuc00d] E. Cuche, P. Marquet and C. Depeursinge. "Spatial filtering for zero-order and twin-image elimination in digital off-axis holography". Appl. Opt. **39**(23): 4070–4075 (2000).

[dA04] M. de Angelis, S. D. Nicola, A. Finizio, G. Pierattini, P. Ferraro, S. Grilli and M. Paturzo. "Evaluation of the internal field in lithium niobate ferroelectric domains by an interferometric method". Appl. Phys. Lett. **85**(14): 2785–2787 (2004).

[Dak03] A. Dakoff, J. Gass and M. K. Kim. "Microscopic three-dimensional imaging by digital interference holography". Journal of Electronic Imaging **12**(4): 643–647 (2003).

[Dem74] T. H. Demetrakopoulos and R. Mittra. "Digital and optical reconstruction of images from suboptical diffraction patterns". Appl. Opt. **13**(3): 665–670 (1974).

[dN98] S. de Nicola and P. Ferraro. "A two-dimensional fast Fourier transform method for measuring the inclination angle of parallel fringe patterns". Opt. Laser Technol. **30**(3-4): 167–173 (1998).

[dN01] S. de Nicola, P. Ferraro, A. Finizio and G. Pierattini. "Correct-image reconstruction in the presence of severe anamorphism by means of digital holography". Opt. Lett. **26**(13): 974–976 (2001).

[dN02] S. de Nicola, P. Ferraro, A. Finizio and G. Pierattini. "Wave front reconstruction of Fresnel off-axis holograms with compensation of aberrations by means of phase-shifting digital holography". Optics and Lasers in Engineering **37**(4): 331–340 (2002).

[dN03] S. de Nicola, P. Ferraro, A. Finizio, S. Grilli and G. Pierattini. "Experimental demonstration of the longitudinal image shift in digital holography". Opt. Eng. **42**(6): 1625–1630 (2003).

[dN04] S. de Nicola, P. Ferraro, A. Finizio, S. Grilli, G. Coppola, M. Iodice, P. D. Natale and M. Chiarini. "Surface topography of microstructures in lithium niobate by digital holographic microscopy". Measurement Science and Technology **15**(5): 961–968 (2004).

[dN05a] S. de Nicola, A. Finizio, G. Pierattini, D. Alfieri, S. Grilli, L. Sansone and P. Ferraro. "Recovering correct phase information in multiwavelength digital holographic microscopy by compensation for chromatic aberrations". Opt. Lett. **30**(20): 2706–2708 (2005).

[dN05b] S. de Nicola, A. Finizio, G. Pierattini, P. Ferraro and D. Alfieri. "Angular spectrum method with correction of anamorphism for numerical reconstruction of digital holograms on tilted planes". Opt. Express **13**(24): 9935–9940 (2005).

[Dub99] F. Dubois, L. Joannes, O. Dupont, J. L. Dewandel and J. C. Legros. "An integrated optical set-up for fluid-physics experiments under microgravity conditions". Measurement Science and Technology **10**(10): 934–945 (1999).

[Dub02a] F. Dubois, C. Minetti, O. Monnom, C. Yourassowsky, J. C. Legros and P. Kischel. "Pattern recognition with a digital holographic microscope working in partially coherent illumination". Appl. Opt. **41**(20): 4108–4119 (2002).

[Dub02b] F. Dubois, O. Monnom, C. Yourassowsky and J. C. Legros. "Border processing in digital holography by extension of the digital hologram and reduction of the higher spatial frequencies". Appl. Opt. **41**(14): 2621–2626 (2002).

[Duc99] M. G. Ducros, J. F. de Boer, H.-E. Huang, L. C. Chao, Z. Chen, J. S. Nelson, T. E. Milner and H. G. Rylander. "Polarization Sensitive Optical Coherence Tomography of the Rabbit Eye". IEEE Journal of selected topics in quantum electronics **5**(4): 1159–1167 (1999).

[Dun03] C. Dunsby, Y. Gu and P. M. W. French. "Single-shot phase-stepped wide-field coherence-gated imaging". Opt. Express **11**(2): 105–115 (2003).

[ED99] F. El-Diasty. "Interferometric determination of induced birefringence due to bending in single-mode optical fibers". J. Opt. A: Pure Appl. Opt **1**: 197–200 (1999).

[Fer03a] P. Ferraro, G. Coppola, S. D. Nicola, A. Finizio and G. Pierattini. "Digital holographic microscope with automatic focus tracking by detection sample displacement in real time". Opt. Lett. **28**(14): 1257–1259 (2003).

[Fer03b] P. Ferraro, S. D. Nicola, A. Finizio, G. Coppola, S. Grilli, C. Magro and G. Pierattini. "Compensation of the inherent wave front curvature in digital holographic coherent microscopy for quantitative phase-contrast imaging". Appl. Opt. **42**(11): 1938–1946 (2003).

[Fer04] P. Ferraro, S. D. Nicola, G. Coppola, A. Finizio, D. Alfieri and G. Pierattini. "Controlling image size as a function of distance and wavelength in Fresnel-transform reconstruction of digital holograms". Opt. Lett. **29**(8): 854–856 (2004).

[Fra87] M. Françon. *Holographie* (Paris, 1987).

[Gas03] J. Gass, A. Dakoff and M. K. Kim. "Phase imaging without 2 pi ambiguity by multiwavelength digital holography". Opt. Lett. **28**(13): 1141–1143 (2003).

[Goo67] J. W. Goodman and R. W. Lawrence. "Digital image formation from electronically detected holograms". Appl. Phys. Lett. **11**(3): 77–79 (1967).

[Goo68] J. W. Goodman. *Introduction to Fourier Optics* (San Francisco, Calif., 1968).

[Gri01] S. Grilli, P. Ferraro, S. D. Nicola, A. Finizio, G. Pierattini and R. Meucci. "Whole optical wavefields reconstruction by digital holography". Opt. Express **9**(6): 294–302 (2001).

[Gri04] S. Grilli, P. Ferraro, M. Paturzo, D. Alfieri and P. D. Natale. "In-situ visualization, monitoring and analysis of electric field domain reversal process in ferroelectric crystals by digital holography". Opt. Express **12**(9): 1832–1842 (2004).

[Guo02] C. S. Guo, L. Zhang, H. T. Wang, J. Liao and Y. Y. Zhu. "Phase-shifting error and its elimination in phase-shifting digital holography". Opt. Lett. **27**(19): 1687–1689 (2002).

[Had92] W. S. Haddad, D. Cullen, J. C. Solem, J. W. Longworth, A. McPherson, K. Boyer and C. K. Rhodes. "Fourier-transform holographic microscope". Appl. Opt. **31**(24): 4973–4978 (1992).

[Han79] *Handbook of optical holography* (H.J. Caulfield Ed., New York, 1979).

[Har96] P. Hariharan. *Optical holography:principles, techniques, and applications* (1996).

[He05] M.-Z. He, L.-Z. Cai, Q. Liu and X.-L. Yang. "Phase-only encryption and watermarking based on phase-shifting interferometry". Appl. Opt. **44**(13): 2600–2606 (2005).

[Hin02] K. D. Hinsch. "Holographic particle image velocimetry". Measurement Science and Technology **13**(7): R61–R72 (2002).

[Hua03] X. R. Huang and R. W. Knighton. "Diattenuation and polarization preservation of retinal nerve fiber layer reflectance". Appl. Opt. **42**(28): 5737–5743 (2003).

[Iem05] U. Iemma, L. Morino and M. Diez. "Digital holography and Karhunen-Loève decomposition for the modal analysis of two-dimensional vibrating structures". Journal of Sound and Vibration (in press) (2005).

[Ike05] T. Ikeda, G. Popescu, R. R. Dasari and M. S. Feld. "Hilbert phase microscopy for investigating fast dynamics in transparent systems". Opt. Lett. **30**(10): 1165–1167 (2005).

[Ind99] G. Indebetouw and P. Klysubun. "Optical sectioning with low coherence spatio-temporal holography". Opt. Commun. **172**: 25–29 (1999).

[Ind01] G. Indebetouw and P. Klysubun. "Spatiotemporal digital microholography". J. Opt. Soc. Am. A-Opt. Image Sci. Vis. **18**(2): 319–325 (2001).

[Jar93] Z. Jaroszewicz, J. Sochacki, A. Kolodziejczyk and L. R. Staronski. "Apodized annular-aperture logarithmic axicon: smoothness and uniformity of intensity distributions". Opt. Lett. **18**(22): 1893–1895 (1993).

[Jav00] B. Javidi and T. Nomura. "Securing information by use of digital holography". Opt. Lett. **25**(1): 28–30 (2000).

[Jav05a] B. Javidi, P. Ferraro, S.-H. Hong, S. D. Nicola, A. Finizio, D. Alfieri and G. Pierattini. "Three-dimensional image fusion by use of multiwavelength digital holography". Opt. Lett. **30**(2): 144–146 (2005).

[Jav05b] B. Javidi, I. Moon, S. Yeom and E. Carapezza. "Three-dimensional imaging and recognition of microorganism using single-exposure on-line (SEOL) digital holography". Opt. Express **13**(12): 4492 – 4506 (2005).

[Jeo05] K. Jeong, L. Peng, J. J. Turek, M. R. Melloch and D. D. Nolte. "Fourier-domain holographic optical coherence imaging of tumor spheroids and mouse eye". Appl. Opt. **44**(10): 1798–1805 (2005).

[Jia03] S. Jiao, W. Yu, G. Stoica and L. V. Wang. "Contrast Mechanisms in Polarization-Sensitive Mueller-Matrix Optical Coherence Tomography and Application in Burn Imaging". Applied Optics-OT **42**(25): 5191–5197 (2003).

[Kat02] J. Kato, I. Yamaguchi and T. Matsumura. "Multicolor digital holography with an achromatic phase shifter". Opt. Lett. **27**(16): 1403–1405 (2002).

[Keb99] V. Kebbel, M. Adams, H. J. Hartmann and W. Juptner. "Digital holography as a versatile optical diagnostic method for microgravity experiments". Measurement Science and Technology **10**(10): 893–899 (1999).

[Kem99] Q. Kemao, M. Hong and W. Xiaoping. "Real-time polarization phase shifting technique for dynamic deformation measurement". Optics and Lasers in Engineering **31**(4): 289–295 (1999).

[Kem05] N. J. Kemp, J. Park, H. N. Zaatari, H. G. Rylander and T. E. Milner. "High-sensitivity determination of birefringence in turbid media with enhanced polarization-sensitive optical coherence tomography". J. Opt. Soc. Am. A-Opt. Image Sci. Vis. **22**(3): 552–560 (2005).

[Kim00] M. K. Kim. "Tomographic three-dimensional imaging of a biological specimen using wavelength-scanning digital interference holography". Opt. Express **7**(9): 305–310 (2000).

[Kli90] D. S. Kliger, J. W. Lewis and C. E. Randall. *Polarized light in optics and spectroscopy* (Academic Press, Inc., San Diego, 1990).

[Kol92] C. L. Koliopoulos. "Simultaneous phase-shift interferometer". In V. J. Doherty, ed., "Advanced Optical Manufacturing and Testing II", (SPIE, 1992), vol. 1531, pp. 119–127.

[Kol03] E. Kolenovic, W. Osten, R. Klattenhoff, S. C. Lai, C. von Kopylow and W. Juptner. "Miniaturized digital holography sensor for distal three-dimensional endoscopy". Appl. Opt. **42**(25): 5167–5172 (2003).

[Kro72a] M. A. Kronrod, N. S. Merzlyakov and L. P. Yaroslavsky. "Reconstruction of holograms with a computer". Sov Phys-Tech Phys **17**: 333–334 (1972).

[Kro72b] M. A. Kronrod, L. P. Yaroslavsky and N. S. Merzlyakov. "Computer synthesis of transparency holograms". Sov Phys-Tech Phys **17**: 329–332 (1972).

[Lai00a] S. Lai and M. A. Neifeld. "Digital wavefront reconstruction and its application to image encryption". Opt. Commun. **178**(4-6): 283–289 (2000).

[Lai00b] S. C. Lai, B. King and M. A. Neifeld. "Wave front reconstruction by means of phase-shifting digital in-line holography". Opt. Commun. **173**(1-6): 155–160 (2000).

[Leb03] D. Lebrun, A. M. Benkouider, S. Coetmellec and M. Malek. "Particle field digital holographic reconstruction in arbitrary tilted planes". Opt. Express **11**(3): 224–229 (2003).

[Lei97] E. N. Leith. "Overview of the developments of holography". Journal of imaging science and technology **41**(3): 201–204 (1997).

[Lie03] M. Liebling, T. Blu and M. Unser. "Fresnelets: New multiresolution wavelet bases for digital holography". IEEE Trans. Image Process. **12**(1): 29–43 (2003).

[Lie04a] M. Liebling. "On Fresnelets, Interference fringes, and digital holography" (2004).

[Lie04b] M. Liebling, T. Blu and M. Unser. "Complex-wave retrieval from a single off-axis hologram". J. Opt. Soc. Am. A-Opt. Image Sci. Vis. **21**(3): 367–377 (2004).

[Loh65] A. W. Lohmann. "Reconstruction of vectorial wavefronts". Appl. Opt. **4**: 1667–1668 (1965).

[Ma04] L. H. Ma, H. Wang, Y. Li and H. Z. Jin. "Numerical reconstruction of digital holograms for three-dimensional shape measurement". J. Opt. A-Pure Appl. Opt. **6**(4): 396–400 (2004).

[Mar03] P. Marquet. "Développement d'une nouvelle technique de microscopie optique tridimensionnelle, la microscopie holographique digitale. Perspectives pour l'étude de la plasticite neuronale" (2003).

[Mar05] P. Marquet, B. Rappaz, P. J. Magistretti, E. Cuche, Y. Emery, T. Colomb and C. Depeursinge. "Digital holographic microscopy: a noninvasive contrast imaging technique allowing quantitative visualization of living cells with subwavelength axial accuracy". Opt. Lett. **30**(5): 468–470 (2005).

[Mas03] P. Massatsch, E. Cuche and C. D. Depeursinge. "Low coherence digital holographic tomography". In "Novel Optical Instrumentation for Biomedical Applications", (2003), vol. 5143, pp. 18–21.

[Mas05] P. Massatsch, F. Charrière, E. Cuche, P. Marquet and C. Depeursinge. "Time-domain optical coherence tomography with digital holographic microscopy". Appl. Opt. **44**(10): 1806–1812 (2005).

[Mil86] J. P. Mills and B. J. Thompson. "Effect of aberrations and apodization on the performance of coherent optical systems. II. Imaging". J. Opt. Soc. Am. A-Opt. Image Sci. Vis. **3**(5): 704–716 (1986).

[Mil01] J. E. Millerd and N. J. Brock. "Methods and apparatus for splitting, imaging, and measuring wavefronts in interferometry" (2001).

[Mil05] G. A. Mills and I. Yamaguchi. "Effects of quantization in phase-shifting digital holography". Appl. Opt. **44**(7): 1216–1225 (2005).

[Mül04] J. Müller, V. Kebbel and W. Jüptner. "Characterization of spatial particle distributions in a spray-forming process using digital holography". Measurement Science and Technology **15**(4): 706–710 (2004).

[ML05a] L. Martínez-León, G. Pedrini and W. Osten. "Applications of short-coherence digital holography in microscopy". Appl. Opt. **44**(19): 3977–3984 (2005).

[Mül05b] J. Müller, V. Kebbel and W. Jüptner. "Digital holography as a tool for testing high-aperture micro-optics". Optics and Lasers in Engineering **43**(7): 739–751 (2005).

[Mon05] F. Montfort. "Tomography using multiple wavelengths in digital holographic microscopy" (2005).

[Monona] F. Montfort, T. Colomb, F. Charrière, E. Cuche and C. Depeursinge. "Use of weights in sub-micron optical tomography by multiple wavelength digital holographic microscopy: improvement of signal to noise ratio" (in preparation).

[Mononb] F. Montfort, T. Colomb, F. Charrière, E. Cuche, S. Herminjard and C. Depeursinge. "Sub-micron optical tomography by multiple wavelength digital holographic microscopy" (in preparation).

[Mur00] S. Murata and N. Yasuda. "Potential of digital holography in particle measurement". Opt. Laser Technol. **32**(7-8): 567–574 (2000).

[Nil98] B. Nilsson and T. E. Carlsson. "Direct three-dimensional shape measurement by digital light-in-flight holography". Appl. Opt. **37**(34): 7954–7959 (1998).

[Nil00] B. Nilsson and T. E. Carlsson. "Simultaneous measurement of shape and deformation using digital light-in-flight recording by holography". Opt. Eng. **39**(1): 244–253 (2000).

[Nis04] N. K. Nishchal, J. Joseph and K. Singh. "Fully phase encryption using digital holography". Opt. Eng. **43**(12): 2959–2966 (2004).

[Nom04] T. Nomura, K. Uota and Y. Morimoto. "Hybrid optical encryption of a 3-D object using a digital holographic technique". Opt. Eng. **43**(10): 2228–2232 (2004).

[Oht94] Y. Ohtsuka and K. Oka. "Contour Mapping of the Spatiotemporal State of Polarization of Light". Appl. Opt. **33**(13): 2633–2636 (1994).

[Oka03] K. Oka and T. Kaneko. "Compact complete imaging polarimeter using birefringent wedge prisms". Opt. Express **11**(13): 1510–1519 (2003).

[Old95] R. Oldenbourg and G. Mei. "New polarized light microscope with precision universal compensator". Journal of Microscopy **180**(2): 140–147 (1995).

[Ono98] R. Onodera and Y. Ishii. "Two-wavelength interferometry that uses a Fourier-transform method". Appl. Opt. **37**(34): 7988–7994 (1998).

[Ort03] M. Ortuno, S. Gallego, C. Garcia, C. Neipp and I. Pascual. "Holographic characteristics of a 1-mm-thick photopolymer to be used in holographic memories". Appl. Opt. **42**(35): 7008–7012 (2003).

[Pan03] G. Pan and H. Meng. "Digital holography of particle fields: reconstruction by use of complex amplitude". Appl. Opt. **42**(5): 827–833 (2003).

[Par02] Y. Park, T.-J. Ahn, Y. H. Kim, W.-T. Han, U.-C. Paek and D. Y. Kim. "Measurement method for profiling the residual stress and the strain-optic coefficient of an optical fiber". Appl. Opt. **41**(1): 21–26 (2002).

[Pat05] M. Paturzo, P. Ferraro, S. Grilli, D. Alfieri, P. D. Natale, M. de Angelis, A. Finizio, S. D. Nicola, G. Pierattini, F. Caccavale, D. Callejo and A. Morbiato. "On the origin of internal field in Lithium Niobate crystals directly observed by digital holography". Opt. Express **13**(14): 5416–5423 (2005).

[Ped97] G. Pedrini and H. J. Tiziani. "Quantitative evaluation of two-dimensional dynamic deformations using digital holography". Opt. Laser Technol. **29**(5): 249–256 (1997).

[Ped01a] G. Pedrini and S. Schedin. "Short coherence digital holography for 3D microscopy". Optik **112**(9): 427–432 (2001).

[Ped01b] G. Pedrini, S. Schedin and H. J. Tiziani. "Aberration compensation in digital holographic reconstruction of microscopic objects". J. Mod. Opt. **48**(6): 1035–1041 (2001).

[Ped02] G. Pedrini and H. J. Tiziani. "Short-coherence digital microscopy by use of a lensless holographic imaging system". Appl. Opt. **41**(22): 4489–4496 (2002).

[Ped03] G. Pedrini, I. Alexeenko, W. Osten and H. J. Tiziani. "Temporal phase unwrapping of digital hologram sequences". Appl. Opt. **42**(29): 5846–5854 (2003).

[Pop04] G. Popescu, L. P. Deflores, J. C. Vaughan, K. Badizadegan, H. Iwai, R. R. Dasari and M. S. Feld. "Fourier phase microscopy for investigation of biological structures and dynamics". Opt. Lett. **29**(21): 2503–2505 (2004).

[Ram00] K. Ramesh and D. Tamrakar. "Improved determination of retardation in digital photoelasticity by load stepping". Optics and Lasers in Engineering **33**: 387–400 (2000).

[Rap05] B. Rappaz, P. Marquet, E. Cuche, Y. Emery, C. Depeursinge and P. J. Magistretti. "Measurement of the integral refractive index and dynamic cell morphometry of living cells with digital holographic microscopy". Opt. Express **13**(23): 9361 – 9373 (2005).

[Roo03] G. Roosen, A. Godard, S. Maerten, V. Reboud, N. Dubreuil and G. Pauliat. "Self-organization of laser cavities using dynamic holograms". Optical Materials **23**(1-2): 289–293 (2003).

[Sal91] B. E. Saleh and M. C. Teich. *Fundamentals of Photonics* (John Wiley and Sons, INC, New York, 1991).

[Sch94a] U. Schnars. "Direct phase determination in hologram interferometry with use of digitally recorded holograms". J. Opt. Soc. Am. A **11**: 2011–2015 (1994).

[Sch94b] U. Schnars and W. Jüptner. "Direct recording of holograms by a CCD target and numerical reconstruction". Appl. Opt. **33**(2): 179–181 (1994).

[Sch99] S. Schedin, G. Pedrini, H. J. Tiziani and F. M. Santoyo. "All-fibre pulsed digital holography". Opt. Commun. **165**(4-6): 183–188 (1999).

[Sch01] S. Schedin, G. Pedrini, H. J. Tiziani and A. K. Aggarwal. "Comparative study of various endoscopes for pulsed digital holographic interferometry". Appl. Opt. **40**(16): 2692–2697 (2001).

[Sch02] U. Schnars and W. P. O. Jüptner. "Digital recording and numerical reconstruction of holograms". Measurement Science and Technology **13**(9): R85–R101 (2002).

[Seb05] M. Sebesta and M. Gustafsson. "Object characterization with refractometric digital Fourier holography". Opt. Lett. **30**(5): 471–473 (2005).

[She97] R. M. Shelby, J. A. Hoffnagle, G. W. Burr, C. M. Jefferson, M.-P. Bernal, H. Coufal, R. K. Grygier, H. Günther, R. M. Macfarlane and G. T. Sincerbox. "Pixel-matched holographix data storage with megabit pages". Opt. Lett. **22**(19): 1509–1511 (1997).

[Sin05] P. Singh, M. S. Faridi, C. Shakher and R. S. Sirohi. "Measurement of focal length with phase-shifting Talbot interferometry". Appl. Opt. **44**(9): 1572–1576 (2005).

[Sit05] G. Situ and J. Zhang. "Multiple-image encryption by wavelength multiplexing". Opt. Lett. **30**(1306-1308) (2005).

[Smi69] H. Smith. *Principles of holography* (New York, 1969).

[Soo02] S. Soontaranon, J. Widjaja and T. Asakura. "Direct analysis of in-line particle holograms by using wavelet transform and envelope reconstruction method". Optik **113**(11): 489–494 (2002).

[Spa02] G. S. Spagnolo and D. Ambrosini. "Diffractive optical element based sensor for roughness measurement". Sensors and Actuators A **100**(2-3): 180–186 (2002).

[Sta00] A. Stadelmaier and J. H. Massig. "Compensation of lens aberrations in digital holography". Opt. Lett. **25**(22): 1630–1632 (2000).

[Sto94] K. J. Stout and W. Dong. *Three dimensional surface topography: measurement, interpretation and applications: a survey and bibliography* (Penton Press ed, London, 1994).

[Str69] G. Stroke. *An introduction to coherent optics and holography* (Academic press, New York, 1969).

[Sun05] H. Sun, M. A. Player, J. Watson, D. C. Hendry, R. G. Perkins, G. Gust and D. M. Paterson. "The use of digital/electronic holography for biological applications". J. Opt. A-Pure Appl. Opt. **7**(6): S399–S407 (2005).

[Taj00] E. Tajahuerce and B. Javidi. "Encrypting three-dimensional information with digital holography". Appl. Opt. **39**(35): 6595–6601 (2000).

[Tak99] Y. Takaki and H. Ohzu. "Fast numerical reconstruction technique for high-resolution hybrid holographic microscopy". Appl. Opt. **38**(11): 2204–2211 (1999).

[The05] A. Thelen, J. Bongartz, D. Giel, S. Frey and P. Hering. "Iterative focus detection in hologram tomography". J. Opt. Soc. Am. A-Opt. Image Sci. Vis. **22**(6): 1176–1180 (2005).

[Tis01] T. V. Tishko and V. P. Titar. "Holographic microscopy. Methods, devices, applications". Lfnm'2001: Proceedings of the 3rd International Workshop on Laser and Fiber-Optical Networks Modeling pp. 162–167 (2001).

[Tis03] T. V. Tishko, V. P. Titar, T. M. Barchotkina and D. N. Tishko. "Application of the holographic interference microscope for investigation of ozone therapy influence on blood erythrocytes of patients In vivo". Advanced Optoelectronics and Lasers **5582**: 119–126 (2003).

[Tis05] T. V. Tishko, V. P. Titar and D. N. Tishko. "Holographic methods of three-dimensional visualization of microscopic phase objects". Journal of Optical Technology **72**(2): 203–209 (2005).

[Ume98] N. Umeda, H. Iijima, M. Ishikawa and A. Takayanagi. "Birefringence imaging with illumination mode near field scanning optical microscope". SPIE **3467**(Part of the SPIE Conference on Far -and Near- Field Optics): 13–17 (1998).

[Upa66] J. Upatnieks, A. V. Lugt and E. Leith. "Correction of lens aberrations by means of holograms". Appl. Opt. **5**(4): 589–593 (1966).

[Van66] R. F. Vanligte and H. Osterberg. "Holographic microscopy". Nature **211**: 282–283 (1966).

[vH04] R. van Hout and J. Katz. "A method for measuring the density of irregularly shaped biological aerosols such as pollen". Journal of Aerosol Science **35**: 1369–1384 (2004).

[Wag00] C. Wagner, W. Osten and S. Seebacher. "Direct shape measurement by digital wavefront reconstruction and multiwavelength contouring". Opt. Eng. **39**(1): 79–85 (2000).

[Wan04] C. Wang, S. H. Chen, X. G. Yang and L. Li. "Investigation of chloride-induced pitting processes of iron in the H2SO4 solution by the digital holography". Electrochem. Commun. **6**(10): 1009–1015 (2004).

[War71] J. Ward, D. Auth and F. P. Carlson. "Lens Aberration Correction by Holography". Appl. Opt. **10**(4): 896–900 (1971).

[Wya03] J. C. Wyant. "Dynamic interferometry". Optics and Photonics News **14**(4): 36–41 (2003).

[Xu01] L. Xu, X. Y. Peng, J. M. Miao and A. K. Asundi. "Studies of digital microscopic holography with applications to microstructure testing". Appl. Opt. **40**(28): 5046–5051 (2001).

[Xu03] W. Xu, M. H. Jericho, H. J. Kreuzer and I. A. Meinertzhagen. "Tracking particles in four dimensions with in-line holographic microscopy". Opt. Lett. **28**(3): 164–166 (2003).

[Yam97] I. Yamaguchi and T. Zhang. "Phase-shifting digital holography". Opt. Lett. **22**(16): 1268–1270 (1997).

[Yam01a] I. Yamaguchi, J. Kato and S. Ohta. "Surface shape measurement by phase-shifting digital holography". Opt. Rev. **8**(2): 85–89 (2001).

[Yam01b] I. Yamaguchi, J. Kato, S. Ohta and J. Mizuno. "Image formation in phase-shifting digital holography and applications to microscopy". Appl. Opt. **40**(34): 6177–6186 (2001).

[Yam02] I. Yamaguchi, T. Matsumura and J. Kato. "Phase-shifting color digital holography". Opt. Lett. **27**(13): 1108–1110 (2002).

[Yam03] I. Yamaguchi, J. Kato and H. Matsuzaki. "Measurement of surface shape and deformation by phase-shifting image digital holography". Opt. Eng. **42**(5): 1267–1271 (2003).

[Yam04] I. Yamaguchi, K. Kobayashi and L. Yaroslavsky. "Measurement of surface roughness by speckle correlation". Opt. Eng. **43**(11): 2753–2761 (2004).

[Yam05] M. Yamagiwa, A. Komatsu, Y. Awatsuji and T. Kubota. "Observation of propagating femtosecond light pulse train generated by an integrated array illuminator as a spatially and temporally continuous motion picture". Opt. Express **13**(9): 3296–3302 (2005).

[Yan03] L. Yang, C. M. Taylor, Y. Rakovich and E. M. McCabe. "Three-dimensional imaging of microspheres with confocal and conventional polarization microscopes". Appl. Opt. **42**(28): 5693–5700 (2003).

[Yan04] X. G. Yang, S. H. Chen, C. Wang and L. Li. "In-line digital holography for the study of dynamic processes of electrochemical reaction". Electrochem. Commun. **6**(7): 643–647 (2004).

[Yon05] L. Yongqian, Z. Zhenyu and L. Xiaoying. "Elimination of reference phase errors in phase-shifting interferometry". Measurement Science and Technology **16**(6): 1335–1340 (2005).

[Yu03] L. F. Yu and L. L. Cai. "Multidimensional data encryption with digital holography". Opt. Commun. **215**(4-6): 271–284 (2003).

[Yu05] L. Yu and M. K. Kim. "Wavelength scanning digital interference holography for variable tomographic scanning". Opt. Express **13**(15): 5621 – 5627 (2005).

[Zem01] "ZEMAX: Optical Design Program, User's Guide, Version 10.0" (Focus Software, Tucson, 2001), pp. 126–127.

[Zha98] T. Zhang and I. Yamaguchi. "Three-dimensional microscopy with phase-shifting digital holography". Opt. Lett. **23**(15): 1221–1223 (1998).

[Zha04a] F. Zhang, J. D. R. Valera, I. Yamaguchi, M. Yokota and G. Mills. "Vibration Analysis by Phase Shifting Digital Holography". Opt. Rev. **11**(5): 297–299 (2004).

[Zha04b] F. C. Zhang, I. Yamaguchi and L. P. Yaroslavsky. "Algorithm for reconstruction of digital holograms with adjustable magnification". Opt. Lett. **29**(14): 1668–1670 (2004).

# Appendix A

# Zernike coefficients

The Zernike polynomials are a set of functions that are orthogonal over the unit circle. They are useful for describing the shape of an aberrated wavefront. Several different normalization and numbering schemes for these polynomials are in common use. Below we present the common ordering and the ordering we use, similar to the one used in Zemax program.

The Zernike polynomials are usually defined in polar coordinates ($\rho$,$\theta$), where $\rho$ is the radial coordinate ranging from 0 to 1 and $\theta$ is the azimuthal component ranging from 0 to $2\pi$. Each of the Zernike polynomials consists in three components: a normalization factor, a radial-dependent component and an azimuthal-dependent component. The radial component is a polynomial, whereas the azimuthal component is sinusoidal. A double indexing scheme is useful for unambiguously describing these functions, with the index $n$ describing the highest power (order) of the radial polynomial and the index $m$ describing the azimuthal frequency of the sinusoidal component. By this scheme the Zernike polynomials are defined as

$$Z_n^m(\rho,\theta) = \begin{cases} N_n^m R_n^{|m|}(\rho)\cos(m\theta) & \text{for } m \geq 0 \\ -N_n^m R_n^{|m|}(\rho)\sin(m\theta) & \text{for } m < 0 \end{cases} \tag{A.1}$$

where $N_n^m$ is the normalization factor described in more detail below and $R_n^{|m|}(\rho)$ is given by

$$R_n^{|m|}(\rho) = \sum_{s=0}^{(n-|m|)/2} \frac{(-1)^s (n-s)!}{s!\,[0.5(n+|m|-s)]!\,[0.5(n-|m|-s)]!}\rho^{n-2s}. \tag{A.2}$$

This definition uniquely describes the Zernike polynomials except for the

| **n/m** | **-5** | **-4** | **-3** | **-2** | **-1** | **0** | **1** | **2** | **3** | **4** | **5** |
|---|---|---|---|---|---|---|---|---|---|---|---|
| **0** | | | | | | $j=0$ | | | | | |
| **1** | | | | | 1 | | 2 | | | | |
| **2** | | | | 3 | | 4 | | 5 | | | |
| **3** | | | 6 | | 7 | | 8 | | 9 | | |
| **4** | | 10 | | 11 | | 12 | | 13 | | 14 | |
| **5** | 15 | | 16 | | 17 | | 18 | | 19 | | 20 |

*Table A.1: Zernike pyramid*

normalization constant. The normalization is given by

$$N_n^m = \sqrt{\frac{2(n+1)}{1+\delta_{m0}}}, \tag{A.3}$$

where $\delta_{m0}$ is the Kronecker delta function (i.e. $\delta_{m0} = 1$ for $m = 0$, and $\delta_{m0} = 0$ for $m \neq 0$). Note that the value of $n$ is a positive integer or zero. For a given $n$, $m$ can only take on values -$n$, -$n$ + 2, -$n$ +4, ...$n$.

Sometimes, a single indexing scheme is used for describing Zernike expansion coefficients. Since the polynomials actually depend on two parameters, $n$ and $m$, ordering of a single indexing scheme is arbitrary. To obtain the single index, $j$, it is convenient to lay out the polynomials in a pyramid with row number $n$ and column number $m$ as shown in Table A.1. The single index $j$, starts at the top of the pyramid and steps down from left to right. To convert between $j$ and the values of $n$ and $m$, the following relationships can be used ($\lceil$ is the ceil function):

$$j = \frac{n(n+2)+m}{2}, \tag{A.4}$$

$$n = \lceil \left( \frac{-3+\sqrt{9+8j}}{2} \right), \tag{A.5}$$

$$m = 2j - n(n+2). \tag{A.6}$$

As presented above, the Zernike polynomials are described in polar coordinates, but a cartesian form can be calculated as presented in Table A.2. The classification ♯1 is on the pyramid form. In this thesis we prefer another classification equivalent to the Zemax program one [Zem01] allowing regroupment of similar descriptions (♯2). The resulting polynomials are presented in Table A.3.

| ♯1 | ♯2 | **Cartesian form** | **Description** |
|---|---|---|---|
| $Z_0$ | $Z_0$ | $1$ | Piston |
| $Z_1$ | $Z_2$ | $\sqrt{4}y$ | Tilt y |
| $Z_2$ | $Z_1$ | $\sqrt{4}x$ | Tilt x |
| $Z_3$ | $Z_4$ | $\sqrt{6}(2xy)$ | Astigmatism y |
| $Z_4$ | $Z_3$ | $\sqrt{3}(2x^2+2y^2-1)$ | Power |
| $Z_5$ | $Z_5$ | $\sqrt{6}(x^2-y^2)$ | Astigmatism x |
| $Z_6$ | $Z_8$ | $\sqrt{8}(3x^2y-y^3)$ | Trefoil y |
| $Z_7$ | $Z_6$ | $\sqrt{8}(3x^2y+3y^3-2y)$ | Coma y |
| $Z_8$ | $Z_7$ | $\sqrt{8}(3x^3+3xy^2-2x)$ | Coma x |
| $Z_9$ | $Z_9$ | $\sqrt{8}(x^3-3xy^2)$ | Trefoil x |
| $Z_{10}$ | $Z_{14}$ | $\sqrt{10}(4x^3y-4xy^3)$ | Tetrafoil y |
| $Z_{11}$ | $Z_{12}$ | $\sqrt{10}(8x^3y+8xy^3-6xy)$ | $2^{\text{ary}}$ Astig y |
| $Z_{12}$ | $Z_{10}$ | $\sqrt{5}(6x^4+12x^2y^2+6y^4-6x^2-6y^2+1)$ | $1^{\text{ary}}$ Spherical |
| $Z_{13}$ | $Z_{11}$ | $\sqrt{10}(4x^4-3x^2+3y^2-4y^4)$ | $2^{\text{ary}}$ Astig x |
| $Z_{14}$ | $Z_{13}$ | $\sqrt{10}(x^4-6x^2y^2+y^4)$ | Tetrafoil x |
| $Z_{15}$ | $Z_{20}$ | $\sqrt{12}(5x^4y-10x^2y^3+y^5)$ | Pentafoil y |
| $Z_{16}$ | $Z_{18}$ | $\sqrt{12}(15x^4y+10x^2y^3-5y^5-12x^2y+4y^3)$ | $2^{\text{ary}}$ Trefoil y |
| $Z_{17}$ | $Z_{16}$ | $\sqrt{12}(10x^4y+20x^2y^3+10y^5-12x^2y$ $-12y^3+3y)$ | $2^{\text{ary}}$ Coma y |
| $Z_{18}$ | $Z_{15}$ | $\sqrt{12}(10x^5+20x^3y^2+10xy^4-12x^3$ $+-12xy^23x)$ | $2^{\text{ary}}$ Coma x |
| $Z_{19}$ | $Z_{17}$ | $\sqrt{12}(5x^5-10x^3y^2-15xy^4-4x^3+12xy^2)$ | $2^{\text{ary}}$ Trefoil x |
| $Z_{20}$ | $Z_{19}$ | $\sqrt{12}(x^5-10x^3y^2+5xy^4)$ | Pentafoil x |
| $Z_{21}$ | $Z_{26}$ | $\sqrt{14}(6x^5y-20x^3y^3+6xy^5)$ | |
| $Z_{22}$ | $Z_{24}$ | $\sqrt{14}(24x^5y-20x^3y-24xy^5+20xy^3)$ | $2^{\text{ary}}$ Tetrafoil y |
| $Z_{23}$ | $Z_{22}$ | $\sqrt{14}(30x^5y+60x^3y^3+30xy^5-40x^3y$ $-40xy^3+12xy)$ | $3^{\text{ary}}$ Astig y |
| $Z_{24}$ | $Z_{21}$ | $\sqrt{7}(20x^6+60x^4y^2+60x^2y^4+20y^6-30x^4$ $-60x^2y^2-30y^4+12x^2+12y^2-1)$ | $2^{\text{ary}}$ Spherical |
| $Z_{25}$ | $Z_{23}$ | $\sqrt{14}(15x^6+15x^4y^2-20x^4+6x^2-15x^2y^4$ $-15y^6+20y^4-6y^2)$ | $3^{\text{ary}}$ Astig x |
| $Z_{26}$ | $Z_{25}$ | $\sqrt{14}(6x^6-5x^4-30x^4y^2-30x^2y^4$ $+30x^2y^2+6y^6-5y^4)$ | $2^{\text{ary}}$ Tetrafoil x |
| $Z_{27}$ | $Z_{27}$ | $\sqrt{14}(x^6-15x^4y^2+15x^2y^4-y^6)$ | |

*Table A.2: Cartesian form and description of Zernike coefficients in standard (♯1) and Zemax classifications (♯2)*

| ♯2 | **Cartesian form** | **Description** |
|---|---|---|
| $Z_0$ | $1$ | Piston |
| $Z_1$ | $\sqrt{4}x$ | Tilt x |
| $Z_2$ | $\sqrt{4}y$ | Tilt y |
| $Z_3$ | $\sqrt{3}(2x^2+2y^2-1)$ | Power |
| $Z_4$ | $\sqrt{6}(2xy)$ | Astigmatism y |
| $Z_5$ | $\sqrt{6}(x^2-y^2)$ | Astigmatism x |
| $Z_6$ | $\sqrt{8}(3x^2y+3y^3-2y)$ | Coma y |
| $Z_7$ | $\sqrt{8}(3x^3+3xy^2-2x)$ | Coma x |
| $Z_8$ | $\sqrt{8}(3x^2y-y^3)$ | Trefoil y |
| $Z_9$ | $\sqrt{8}(x^3-3xy^2)$ | Trefoil x |
| $Z_{10}$ | $\sqrt{5}(6x^4+12x^2y^2+6y^4-6x^2-6y^2+1)$ | Primary Spherical |
| $Z_{11}$ | $\sqrt{10}(4x^4-3x^2+3y^2-4y^4)$ | $2^{\text{ary}}$ Astig x |
| $Z_{12}$ | $\sqrt{10}(8x^3y+8xy^3-6xy)$ | $2^{ary}$ Astig y |
| $Z_{13}$ | $\sqrt{10}(x^4-6x^2y^2+y^4)$ | Tetrafoil x |
| $Z_{14}$ | $\sqrt{10}(4x^3y-4xy^3)$ | Tetrafoil y |
| $Z_{15}$ | $\sqrt{12}(10x^5+20x^3y^2+10xy^4-12x^3-12xy^2)$ $+3x)$ | $2^{\text{ary}}$ Coma x |
| $Z_{16}$ | $\sqrt{12}(10x^4y+20x^2y^3+10y^5-12x^2y-12y^3)$ $+3y)$ | $2^{\text{ary}}$ Coma y |
| $Z_{17}$ | $\sqrt{12}(5x^5-10x^3y^2-15xy^4-4x^3+12xy^2)$ | $2^{\text{ary}}$ Trefoil x |
| $Z_{18}$ | $\sqrt{12}(15x^4y+10x^2y^3-5y^5-12x^2y+4y^3)$ | $2^{\text{ary}}$ Trefoil y |
| $Z_{19}$ | $\sqrt{12}(x^5-10x^3y^2+5xy^4)$ | Pentafoil x |
| $Z_{20}$ | $\sqrt{12}(5x^4y-10x^2y^3+y^5)$ | Pentafoil y |
| $Z_{21}$ | $\sqrt{7}(20x^6+60x^4y^2+60x^2y^4+20y^6-30x^4$ $-60x^2y^2-30y^4+12x^2+12y^2-1)$ | $2^{\text{ary}}$ Spherical |
| $Z_{22}$ | $\sqrt{14}(30x^5y+60x^3y^3+30xy^5-40x^3y-40xy^3$ $+12xy)$ | $3^{\text{ary}}$ Astig y |
| $Z_{23}$ | $\sqrt{14}(15x^6+15x^4y^2-20x^4+6x^2-15x^2y^4$ $-15y^6+20y^4-6y^2)$ | $3^{\text{ary}}$ Astig x |
| $Z_{24}$ | $\sqrt{14}(24x^5y-20x^3y-24xy^5+20xy^3)$ | $2^{\text{ary}}$ Tetrafoil y |
| $Z_{25}$ | $\sqrt{14}(6x^6-5x^4-30x^4y^2-30x^2y^4+30x^2y^2$ | |
| $Z_{26}$ | $\sqrt{14}(6x^5y-20x^3y^3+6xy^5)$ | |
| $Z_{27}$ | $\sqrt{14}(x^6-15x^4y^2+15x^2y^4-y^6)$ | |

*Table A.3: Cartesian form and description of Zernike standard coefficients in Zemax classification*

# Appendix B

# 1D Procedure: Parameters Computation

## B.1 $P_{11}$ computation

Let us consider first the second order crossed term parameter $P_{11}$, which can be evaluated by defining two profiles of slopes $\pm 1$, along the diagonals of the image: $n = m + \tau$ ($y = x + cst$) and $n = -m + \nu$ ($y = x - cst$). The second order phase component of the NPL along the first profile is

$$\begin{aligned}\varphi_{+1} =& P_{10}m + P_{01}(m+\tau) + P_{20}m^2 + P_{02}(m+\tau)^2 + P_{11}m(m+\tau) \\ =& \left(P_{20} + P_{02} + P_{11}\right) m^2 + \left(P_{10} + P_{01} + 2P_{02}\tau + P_{11}P_{02}\right) m + \\ & \left(P_{01}\tau + P_{02}\tau^2\right) \\ =& a_2^{(+1)}m^2 + a_1^{(+1)}m + a_0^{(+1)}. \end{aligned} \tag{B.1}$$

Similarly, along the other profile, we have

$$\varphi_{-1} = \left(P_{20} + P_{02} - P_{11}\right) m^2 + ... = a_2^{(-1)}m^2 + a_1^{(-1)}m + a_0^{(-1)}, \tag{B.2}$$

which yields

$$P_{11} = \frac{a_2^{(+1)} - a_2^{(-1)}}{2}, \tag{B.3}$$

where $a_2^{(+1)}$ and $a_2^{(-1)}$ are the second order coefficient of the polynomial fit along the diagonal profiles, respectively $y = x + cst$ and $y = -x + cst$. Henceforth we will note $a_i^{(+j)}$ the $i^{th}$ order coefficient of the polynomial fit along a profile of slope $j$: $y = jx + cst$.

## B.2 $P_{12}$ and $P_{21}$ computation

In order to compute the third order crossed terms $P_{12}$ and $P_{21}$, we need to consider two additional profiles at $n = 2m + \tau$ ($y = 2x + cst$) and

$n = -2m + \nu$ ($y = -2x + cst$). Along the two profiles of slope $\pm 1$, the relations to the third order hold

$$\begin{aligned}\varphi_{+1} &= (P_{30} + P_{03} + P_{12} + P_{21})\, m^3 + ... = a_3^{(+1)} m^3 + ... \\ \varphi_{-1} &= (P_{30} - P_{03} + P_{12} - P_{21})\, m^3 + ... = a_3^{(-1)} m^3 + ....\end{aligned} \tag{B.4}$$

For the profiles of slope $\pm 2$, we have

$$\begin{aligned}\varphi_{+2} &= (P_{30} + 8P_{03} + 4P_{12} + 2P_{21})\, m^3 + ... = a_3^{(+2)} m^3 + ..., \\ \varphi_{-2} &= (P_{30} - 8P_{03} + 4P_{12} - 2P_{21})\, m^3 + ... = a_3^{(-2)} m^3 + ....\end{aligned} \tag{B.5}$$

Eliminating the terms $P_{30}$ and $P_{03}$ in these equations yield

$$P_{12} = \frac{a_3^{(+2)} + a_3^{(-2)} - a_3^{(+1)} - a_3^{(-1)}}{6}, \tag{B.6}$$

$$P_{21} = \frac{2}{3}\left(a_3^{(+1)} - a_3^{(-1)} - \frac{a_3^{(+2)} - a_3^{(-2)}}{8}\right). \tag{B.7}$$

## B.3 $P_{13}$ and $P_{31}$ computation

Using the same profiles as before, we have the following relations

$$\begin{aligned}\varphi_{+1} &= (P_{40} + P_{04} + P_{22} + P_{13} + P_{31})\, m^4 + ... &&= a_4^{(+1)} m^4 + ..., \\ \varphi_{-1} &= (P_{40} + P_{04} + P_{22} - P_{13} - P_{31})\, m^4 + ... &&= a_4^{(-1)} m^4 + ..., \\ \varphi_{+2} &= (P_{40} + 16P_{04} + 4P_{22} + 8P_{13} + 2P_{31})\, m^4 + ... &&= a_4^{(+2)} m^4 + ..., \\ \varphi_{-2} &= (P_{40} + 16P_{04} + 4P_{22} - 8P_{13} - 2P_{31})\, m^4 + ... &&= a_4^{(-2)} m^4 + ....\end{aligned} \tag{B.8}$$

which leads to

$$\begin{aligned}P_{13} &= \frac{a_4^{(+2)} - a_4^{(-2)}}{12} - \frac{a_4^{(+1)} - a_4^{(-1)}}{6} \\ P_{31} &= \frac{2(a_4^{(+1)} - a_4^{(-1)})}{3} - \frac{a_4^{(+2)} - a_4^{(-2)}}{12},\end{aligned} \tag{B.9}$$

where $a_4^{(\pm i)}$ ($i = 1, 2$) are the fourth order coefficients of the polynomial fit along the respective profiles.

## B.4 $P_{22}$ computation

In order to compute $P_{22}$ without using the values $P_{40}$ and $P_{04}$, we need two additional profiles $n = m/2 + \tau$ ($y = x/2 + cst$) and $n = -m/2 + \tau$ ($y = -x/2 + cst$). As before, checking the fourth order terms in the NPL along these profiles yield

$$\begin{aligned}\varphi_{+\frac{1}{2}} &= \frac{1}{16}(16P_{40} + P_{04} + 4P_{22} + 2P_{13} + 8P_{31})\, m^4 + \cdots &&= a_4^{(+\frac{1}{2})} m^4 +, \\ \varphi_{-\frac{1}{2}} &= \frac{1}{16}(16P_{40} + P_{04} + 4P_{22} - 2P_{13} - 8P_{31})\, m^4 + \cdots &&= a_4^{(-\frac{1}{2})} m^4 + .\end{aligned} \tag{B.10}$$

Eliminating the terms $P_{13}$ and $P_{31}$ yields the following equation system

$$\begin{aligned} P_{40} + P_{04} + P_{22} =& \frac{a_4^{(+1)} + a_4^{(-1)}}{2} \\ P_{40} + 16P_{04} + 4P_{22} =& \frac{a_4^{(+2)} + a_4^{(-2)}}{2} \\ P_{40} + \frac{P_{04}}{16} + \frac{P_{22}}{4} =& \frac{a_4^{(+\frac{1}{2})} + a_4^{(-\frac{1}{2})}}{2}. \end{aligned} \tag{B.11}$$

The system is defined by the matrix $\boldsymbol{A}$,

$$\boldsymbol{A} = \begin{pmatrix} 1 & 1 & 1 \\ 1 & 16 & 4 \\ 1 & 1/16 & 1/4 \end{pmatrix} \tag{B.12}$$

which can be inverted easily to solve the system

$$\boldsymbol{A}^{-1} = \frac{1}{9} \begin{pmatrix} -4 & 1/5 & 64/5 \\ -4 & 4/5 & 16/5 \\ 17 & -1 & -16 \end{pmatrix} \tag{B.13}$$

Finally we have

$$P_{22} = \frac{17}{18}\left(a_4^{(+1)} + a_4^{(-1)}\right) - \frac{1}{18}\left(a_4^{(+2)} + a_4^{(-2)}\right) - \frac{8}{9}\left(a_4^{(+\frac{1}{2})} + a_4^{(-\frac{1}{2})}\right) \tag{B.14}$$

## B.5 $P_{14}$, $P_{41}$, $P_{32}$ and $P_{23}$ computation

Let us consider the fifth order terms along the profiles extracted before. We have

$$\begin{aligned} \varphi_{+1} =& \left(P_{50} + P_{05} + P_{41} + P_{14} + P_{32} + P_{23}\right) m^5 + \cdots && = a_5^{(+1)} m^5 + \\ \varphi_{-1} =& \left(P_{50} - P_{05} - P_{41} + P_{14} + P_{32} - P_{23}\right) m^5 + \cdots && = a_5^{(-1)} m^5 + \\ \varphi_{+2} =& \left(P_{50} + 32P_{05} + 2P_{41} + 16P_{14} + 4P_{32} + 8P_{23}\right) m^5 + && = a_5^{(+2)} m^5 + \\ \varphi_{-2} =& \left(P_{50} - 32P_{05} - 2P_{41} + 16P_{14} + 4P_{32} - 8P_{23}\right) m^5 + && = a_5^{(-2)} m^5 + \\ \varphi_{+\frac{1}{2}} =& \left(P_{50} + \frac{P_{05}}{32} + \frac{P_{41}}{2} + \frac{P_{14}}{16} + \frac{P_{32}}{4} + \frac{P_{23}}{8}\right) m^5 + \cdots && = a_5^{(+\frac{1}{2})} m^5 + \\ \varphi_{-\frac{1}{2}} =& \left(P_{50} - \frac{P_{05}}{32} - \frac{P_{41}}{2} + \frac{P_{14}}{16} + \frac{P_{32}}{4} - \frac{P_{23}}{8}\right) m^5 + \cdots && = a_5^{(-\frac{1}{2})} m^5 + . \end{aligned} \tag{B.15}$$

Combining these equations yields the following system

$$\begin{aligned} P_{50} + P_{14} + P_{32} =& \frac{a_5^{(+1)} + a_5^{(-1)}}{2} \\ P_{50} + 16P_{14} + 4P_{32} =& \frac{a_5^{(+2)} + a_5^{(-2)}}{2} \\ P_{50} + \frac{P_{14}}{16} + \frac{P_{32}}{4} =& \frac{a_5^{(+\frac{1}{2})} + a_5^{(-\frac{1}{2})}}{2}. \end{aligned} \tag{B.16}$$

The matrix of this system is identical to the one obtained when computing $P_{22}$ (see Eq. B.12), leading to

$$\begin{aligned} P_{32} &= \frac{17}{18}\left(a_5^{(+1)} + a_5^{(-1)}\right) - \frac{1}{18}\left(a_5^{(+2)} + a_5^{(-2)}\right) - \frac{8}{9}\left(a_5^{(+\frac{1}{2})} + a_5^{(-\frac{1}{2})}\right), \\ P_{14} &= \frac{2}{9}\left(a_5^{(+1)} + a_5^{(-1)}\right) + \frac{2}{45}\left(a_5^{(+2)} + a_5^{(-2)}\right) + \frac{8}{45}\left(a_5^{(+\frac{1}{2})} + a_5^{(-\frac{1}{2})}\right). \end{aligned} \tag{B.17}$$

Another system can be derived from Eq. B.15

$$\begin{aligned} P_{05} + P_{41} + P_{23} &= \frac{a_5^{(+1)} - a_5^{(-1)}}{2} \\ 32P_{05} + 2P_{41} + 8P_{23} &= \frac{a_5^{(+2)} - a_5^{(-2)}}{2} \\ \frac{P_{05}}{32} + \frac{P_{41}}{2} + \frac{P_{23}}{8} &= \frac{a_5^{(+\frac{1}{2})} - a_5^{(-\frac{1}{2})}}{2}. \end{aligned} \tag{B.18}$$

Solving this equation system leads to

$$\begin{aligned} P_{23} &= \frac{17}{18}\left(a_5^{(+1)} - a_5^{(-1)}\right) - \frac{1}{36}\left(a_5^{(+2)} - a_5^{(-2)}\right) - \frac{32}{9}\left(a_5^{(+\frac{1}{2})} - a_5^{(-\frac{1}{2})}\right), \\ P_{41} &= \frac{-4}{18}\left(a_5^{(+1)} - a_5^{(-1)}\right) + \frac{1}{180}\left(a_5^{(+2)} - a_5^{(-2)}\right) + \frac{128}{90}\left(a_5^{(+\frac{1}{2})} - a_5^{(-\frac{1}{2})}\right) \end{aligned} \tag{B.19}$$

By analogy, the definition of others profiles and the solving of resulting equations systems allows to compute higher order crossed-terms.

# Tristan COLOMB

Villette
CH-1934 Le Châble
tristan.colomb@a3.epfl.ch

**Age: 30**
**Single**
**Swiss**

## *Education*

2002–2005 PhD in Digital Holography Microscopy
Institute of Applied Optics, Ecole polytechnique fédérale de Lausanne (EPFL)
PhD dissertation: "Numerical aberrations compensation and polarization imaging in digital holographic microscopy"
Thesis director: Prof. R.-P. Salathé
Thesis advisor: Prof. Ch. Depeursinge

2000–2002 Engineer in Institute of Applied Optics
Institute of Applied Optics, Ecole polytechnique fédérale de Lausanne (EPFL)
Subject: "Heartbeat measurement by a fringe projection method"

1995–2000 MSc in Physics
Ecole polytechnique fédérale Lausanne (EPFL)
Diploma thesis at the Institute of Applied Optics: "Polarization state imaging by use of digital holography"

1990–1995 Maturité scientifique, Collège de l'abbaye de St-maurice

## *Experience*

Research assistant at the Institute of Applied Optics, EPFL
Supervision of several student semester and diploma projects in holography
Teaching assistant for practical work

## *Languages*

Mother tongue French; fluent in English; Basic skills in Spanish; Elementary skills in German.

## *Computer skills*

Programming: Matlab, Labview
Publishing: TEX, Photoshop, Illustrator, Acrobat, HTML, Office

# *Publications*

### Articles


1 T. Colomb, P. Dahlgren, D. Beghuin, E. Cuche, P. Marquet and C. Depeursinge. "Polarization imaging by use of digital holography". Appl. Opt. **41**(1): 27–37 (2002).

2 T. Colomb, E. Cuche, F. Montfort, P. Marquet and C. Depeursinge. "Jones vector imaging by use of digital holography: simulation and experimentation". Opt. Commun. **231**(1-6): 137–147 (2004).

3 T. Colomb, F. Dürr, E. Cuche, P. Marquet, H. Limberger, R.-P. Salathé and C. Depeursinge. "Polarization microscopy by use of digital holography: application to optical fiber birefringence measurements". Appl. Opt. **44**(21): 4461–4469 (2005).

4 T. Colomb, E. Cuche, F. Charrière, J. Kühn, N. Aspert, F. Montfort, P. Marquet and C. Depeursinge. "Automatic procedure for aberration compensation in digital holographic microscopy and applications to specimen shape compensation". Appl. Opt. **45**(5): 851–863 (2006).

5 T. Colomb, F. Montfort, J. Kühn, N. Aspert, E. Cuche, A. Marian, F. Charrière, S. Bourquin, P. Marquet and C. Depeursinge. "A numerical parametric lens for shifting, magnification and complete aberration compensation in digital holographic microscopy" J. Opt. Soc. Am. A (submitted).

6 T. Colomb, J. Kühn, A. Marian, F. Charrière, P. Marquet, E. Cuche, F. Montfort, N. Aspert, S. Bourquin and C. Depeursinge. "Total aberrations compensation in digital holographic microscopy with a conjugated reference hologram" Opt. Express **14**(10): 4300–4306 (2006).

7 V. Apostolopoulos, L. Laversenne, T. Colomb, C. Depeursinge, R. P. Salathé and M. Pollnau. "Femtosecond-irradiation-induced refractive-index changes and channel waveguiding in bulk Ti3+:Sapphire". Appl. Phys. Lett. **85**(7): 1122–1124 (2004).

8 P. Marquet, B. Rappaz, P. J. Magistretti, E. Cuche, Y. Emery, T. Colomb and C. Depeursinge. "Digital holographic microscopy: a noninvasive contrast imaging technique allowing quantitative visualization of living cells with subwavelength axial accuracy". Opt. Lett. **30**(5): 468–470 (2005).

9 F. Charrière, A. Marian, F. Montfort, J. Kuehn, T. Colomb, E. Cuche, P. Marquet and C. Depeursinge. "Cell refractive index tomography by digital holographic microscopy". Opt. Lett. **31**(2): 178–180 (2006).

10 F. Charrière, J. Kühn, T. Colomb, F. Monfort, E. Cuche, Y. Emery, K. Weible, P. Marquet and C. Depeursinge. "Characterization of microlenses by digital holographic microscopy". Appl. Opt. **45**(5): 829–835 (2006).

11 F. Montfort, T. Colomb, F. Charrière, E. Cuche, P. Marquet and C. Depeursinge. "Purely numerical compensation for microscope objective phase curvature in digital holographic microscopy: influence of digital phase masks application position" J. Opt. Soc. Am. A (accepted).

12 F. Montfort, T. Colomb, F. Charrière, E. Cuche and C. Depeursinge. "Use of weights in sub-micron optical tomography by multiple wavelength digital holographic microscopy: improvement of signal to noise ratio" (in preparation).

13 F. Montfort, T. Colomb, F. Charrière, E. Cuche, S. Herminjard and C. Depeursinge. "Sub-micron optical tomography by multiple wavelength digital holographic microscopy" (in preparation).

14 A. Marian, F. Charrière, T. Colomb, F. Montfort and C. Depeursinge. "On the complex 3D amplitude point spread function of lenses and microscope objectives. I Theoretical aspects and simulations" J. Microsc. (submitted).

15 A. Marian, F. Charrière, T. Colomb, F. Montfort and C. Depeursinge. "On the complex 3D amplitude point spread function of lenses and microscope objectives. II Measurements by digital holography" J. Microsc. (submitted).

16 F. Charrière, A. Marian, T. Colomb and C. Depeursinge. "Amplitude point spread function measurement of high NA microscope objectives" (in preparation).

17 F. Charrière, T. Colomb, E. Cuche,P. Marquet and C. Depeursinge. "Shot noise influence in reconstructed phase images SNR in digital holographic microscopy" Appl. Opt (submitted).

**Proceedings**

1 T. Colomb, P. Dahlgren, E. Cuche, D. Beghuin and C. Depeursinge. "A method for polarisation imaging using digital holography". In "Interferometry in Speckle Light - Theory and Applications", (2000), pp. 227–234.

2 T. Colomb, E. Cuche, P. Dahlgren, A. M. Marian, F. Montfort, C. D. Depeursinge, P. Marquet and P. J. Magistretti. "3D imaging of surfaces and cells by numerical reconstruction of wavefronts in Digital Holography applied to transmission and reflection microscopy". In "2002 Ieee International Symposium on Biomedical Imaging, Proceedings", (2002), pp. 773–776.

3 T. Colomb, E. Cuche and C. Depeursinge. "Jones vector imaging by use or digital holography: Simulation results". In "Novel Optical Instrumentation for Biomedical Applications", (2003), vol. 5143, pp. 315–321.

4 T. Colomb, E. Cuche and C. Depeursinge. "Birefringence measurement by use of digital holographic microscopy: examples with fiber optics and concrete samples". In "Proc. SPIE", (Munich, 2005), vol. 5856, pp. 1022–1027.

5 T. Colomb, E. Cuche and C. Depeursinge. "Polarization digital holographic microscope: a single acquisition for a complete determination of polarization state". In H. Bjelkhagen, ed., "Application of holographic and optical coherence methods", (Proc. SPIE, Holo 05, Bulgaria, vol. 6252, 2005).

6 T. Colomb, J. Kühn, F. Charrière, P. Marquet,N. Aspert and C. Depeursinge. "Real-Time Phase Recovery of Biological Cell in Digital Holographic Microscopy by Use of a Self-Calibration Hologram". In "Proc. OSA", (BIOMED, Fort Lauderdale, 2006), in press.

7 T. Colomb, J. Kühn, E. Cuche, F. Charrière, F. Montfort, A. Marian, N. Aspert, P. Marquet and C. Depeursinge. "Automatic procedure for aberrations compensation in digital holographic microscopy". In "Proc. SPIE", (Photonics Europe, Strasbourg, 2006), in press.

8 T. Colomb, F. Charrière, P. Marquet and C. Depeursinge. "Full aberration compensation in digital holographic microscopy". In "Focus On Microscopy Conference (April 9-12, Perth, Western Australia)", (2006).

9 C. D. Depeursinge, E. Cuche, P. Marquet, T. Colomb, P. Dahlgren, A. M. Marian, F. Montfort and P. J. Magistretti. "Digital holography applied to microscopy". In "Practical Holography Xvi and Holographic Materials Viii", (2002), vol. 4659, pp. 30–34.

10 C. D. Depeursinge, E. Cuche, T. Colomb, P. Dahlgren, A. M. Marian, F. Monfort, P. Marquet and P. J. Magistretti. "Cells and tissue imaging with digital holographic microscopy". In "Novel Optical Instrumentation for Biomedical Applications", (2003), vol. 5143, pp. 134–138.

11 C. D. Depeursinge, F. Charrière, A. M. Marian, F. Montfort, T. B. Colomb, J. Kühn, E. Cuche, Y. Emery, P. Marquet and P. J. Magistretti. "Digital Holographic Microscopy applied to Metrology". In "Optical Metrology in Production Engineering", (2004), vol. 5457, pp. 504–512.

12 C. Depeursinge, F. Charrière, A. M. Marian, T. Colomb, F. Montfort, J. Kühn, N. Aspert, M. Botkine, F. Marquet, S. Bourquin, E. Cuche, Y. Emery, P. Marquet and P. J. Magistretti. "Digital Holographic Microscopy, a new imaging technology applied to nanotechnology and life". In H. Bjelkhagen, ed., "Application of holographic and optical coherence methods", (Proc. SPIE, Holo 05, Bulgaria, vol. 6252, 2005).

13 Y. Emery, E. Cuche, F. Marquet, N. Aspert, P. Marquet, J. Kühn, M. Botkine, T. Colomb, F. Montfort, F. Charrière and C. Depeursinge. "Digital Holography Microscopy (DHM): Fast and robust systems for industrial inspection with interferometer resolution". In "Optical Measurement Systems for Industrial Inspection Iv, Pts 1 and 2", (2005), vol. 5856, pp. 930–937.

14 F. Charrière, J. Kühn, T. Colomb, F. Montfort, E. Cuche, Y. Emery, K. Weible and C. D. Depeursinge. "Microlenses metrology with digital holographic microscopy". In "Optical Measurement Systems for Industrial Inspection Iv, Pts 1 and 2", (2005), vol. 5856, pp. 447–453.

15 P. Marquet, P. Magistretti, B. Rappaz, T. Colomb, J. Kühn and C. Depeursinge. "Quantitative Measurements of Dynamic Cell Morphometry and Intracellular Integral Refractive Index with Digital Holographic Microscopy". In "Proc. OSA", (BIOMED, Fort Lauderdale, 2006), in press.

16 F. Charrière, T. Colomb, E. Cuche, P. Marquet and C. Depeursinge. "Digital Holographic Microscopy Applied to Diffraction Tomography of a Cell Refractive Index". In "Proc. OSA", (BIOMED, Fort Lauderdale, 2006), in press.

17 F. Montfort, T. Colomb, F. Charrière, J. Kühn, E. Cuche and C. Depeursinge. "Submicron optical tomography by multiple-wavelength digital holographic microscopy". In "Proc. SPIE", (Photonics Europe, Strasbourg, 2006), in press.

18 J. Kühn, E. Cuche, Y. Emery, T. Colomb, F. Charrière, F. Montfort, A. Marian, M. Botkine, N. Aspert and C. Depeursinge. "Measurements of corner cubes microstructures by high-magnification digital holographic microscopy". In "Proc. SPIE", (Photonics Europe, Strasbourg, 2006), in press.

19 F. Charrière, F. Montfort, J. Kühn, T. Colomb, A. Marian, E. Cuche, P. Marquet and C. Depeursinge. "Use of digital holography microscopy in tomography". In "Proc. SPIE", (Photonics Europe, Strasbourg, 2006), in press.

20 Y. Emery, E. Cuche, F. Marquet, N. Aspert, P. Marquet, J. Kûhn, M. Botkine, T. Colomb, F. Montfort, F. Charrière, C. Depeursinge, P. Debergh and R. Conde. "Digital holography Microscopy (DHM) for metrology and dynamic characterization of MEMS and MOEMS". In "Proc. SPIE", (Photonics Europe, Strasbourg, 2006), in press.

21 Y. Bellouard, T. Colomb, C. Depeursinge, A. A. Said, M. Dugan and P. Bado. "Investigation of Femtosecond Laser Irradiation on Fused Silica". In "Commercial and Biomedical Applications of Ultrafast Lasers VI, Proc. SPIE", (2006), vol.6108.

22 F. Charrière, T. Colomb, P. Marquet and C. Depeursinge. "Digital holographic microscopy for complex pupil function evaluation of high NA microscope objectives". In "Focus On Microscopy Conference (April 9-12, Perth, Western Australia)", (2006).

23 C. Depeursinge, F. Charrière, T. Colomb, J. Kühn, Y. Emery, E. Cuche P. Marquet and B. Rappaz "Digital holographic microscopy". In "Focus On Microscopy Conference (April 9-12, Perth, Western Australia)", (2006).